

Selective epitaxial growth of single crystal diamond and its application for high- performance diamond MOSFET fabrication

高品質単結晶ダイヤモンドの選択エピタキシャル成長およびその高性能ダイヤモンド MOSFET への適用

July 2020

Wenxi	FEI
費	文茜

**Selective epitaxial growth of single crystal
diamond and its application for high-
performance diamond MOSFET
fabrication**

高品質単結晶ダイヤモンドの選択エピタ
キシャル成長およびその高性能ダイヤモ
ンド MOSFET への適用

July 2020

Waseda University

Graduate School of Advanced Science and Engineering

Department of Nanoscience and Nanoengineering,

Research on Nanodevice

Wenxi	FEI
費	文茜

Abstract

Chapter I is a review of synthetic methods and conductivity of diamond semiconductors. In comparison with other wide-bandgap semiconductor materials, diamond (5.5 eV) exhibits excellent properties. High thermal conductivity ($22 \text{ kW m}^{-1} \text{ K}^{-1}$) reduces the heat dissipation area of electronic devices. Moreover, breakdown voltage of up to 10 MV/cm makes it suitable for high-voltage-resistant devices. Furthermore, carrier mobility ($4500 \text{ cm}^2 \text{ V}^{-1} \text{ s}^{-1}$ for electrons, $3800 \text{ cm}^2 \text{ V}^{-1} \text{ s}^{-1}$ for holes) and saturation carrier drift velocity make it a potential candidate for high-frequency devices. Because of high costs and uneven crystalline qualities of natural diamonds, researchers prefer synthetic diamonds. HPHT diamonds are synthesized using high-pressure–high-temperature methods that simulate natural forming conditions, and they are mostly used in industrial cutting and milling tools. Chemical vapor deposition (CVD) has emerged as a method for semiconductor device and jewelry requiring single crystal diamonds or those with fewer grain boundaries. In CVD, a carbon-containing gas (usually methane or carbon dioxide) and hydrogen are excited into carbon-containing active species and atomic hydrogen, after being activated in a reaction chamber, then the reactive species are deposited on a substrate. CVD can be classified as hot filament CVD (HFCVD) and microwave plasma CVD (MPCVD), according to different activation sources. Both types of CVD can synthesize single crystal diamonds with good crystallinity. Since diamonds are insulating by nature, it is necessary to make them conductive to be used in electronic devices. There are usually two types of p-type conduction: boron doping and two-dimensional hole gas (2DHG). However, doping involves a series of problems. Firstly, all the dopants of diamond are at

deep energy levels (compared to silicon doping); thus, the activation rate at room temperature is very low, resulting in limited carrier concentration. For example, lightly boron-doped diamond is almost non-conductive at room temperature. Heavy doping of diamond can only be achieved by a high concentration of dopant gas in the CVD method or ion implantation. However, heavily doped diamond cannot be used for the channel and drift layers owing to its metallic conductivity. Therefore, the doped diamond is mostly used for the source and drain to increase the ohmic contact between diamond and metals. Surface conductivity induced by the hydrogen-terminated (C-H) diamond surface, which was synthesized by CVD, was first noticed in 1989; however, this phenomenon is not regarded as useful for electron devices. After the C-H diamond metal semiconductor field effect transistor (MESFET) was implemented in 1994, most diamond FETs with excellent performance were achieved on the C-H diamond. However, for industrial applications, the C-H surface or interface is still believed to be unreliable by semiconductor engineers. Alternative surface termination shows similar qualities and robustness is highly desired.

In Chapter II, we proposed a selective growth method of point-arc remote MPCVD and SiO₂ mask, to achieve high quality synthesis of single crystal diamonds. The ohmic contact between diamond and metal can be improved by selective grown doped diamond, and the metal mask is usually used during growth. Until now, low-resistivity n-type heavily doped contacts of (111) diamond and p-type heavily doped contacts of (111) and (100) diamonds have been achieved through selective growth. However, the concerns of deformation of the metal mask during the growth process and the contamination of diamond by the filament metal material when using HFCVD remain to be solved. The proposed remote CVD is a method in which contactless plasma fixed at an antenna edge.

The synthesis of carbon nanotubes and heteroepitaxial growth of diamond by this apparatus have been previously reported. However, the selective homoepitaxial growth of diamond has not been previously reported. After analyzing the results of the surface morphology (by scanning electron microscopy and energy-dispersive X-ray spectroscopy), crystalline quality (Raman spectroscopy), and contamination concentration of the selectively grown diamond, selective growth was successfully achieved by the proposed technique and SiO₂ mask. The selectively grown diamond is of high crystallinity and is not contaminated by the antenna material.

In Chapter III, the high-performance silicon-terminated diamond metal oxide semiconductor field-effect transistor (MOSFET) based on selective homoepitaxial growth technique in Chapter II was fabricated and electrically characterized. SiO₂ which is generally considered as a reliable insulator in MOS power device, its stability under high temperature and reductive environment as mask was revealed by selective growth of diamond in Chapter II. The conductivity of silicon-terminated diamond in MOSFET devices was derived from the surface hole accumulation at the silicon-terminated (C-Si) diamond and SiO₂ interface. The heavily boron-doped diamond/metal layer with low resistivity was achieved by selective growth. The C1s X-ray photoelectron spectroscopy spectrum confirmed that a C-Si diamond channel was formed under the high-temperature and reductive environment of the SiO₂ mask at the contact surface with the diamond. Moreover, the hydrogen depth profile acquired at the SiO₂/diamond interface suggested C-Si is mainly responsible for the channel conductivity. The MOSFET showed high current modulation from the field effect without a C-H of diamond channel. The drain current (I_{DS}) was controlled by varying the gate voltage (V_{GS}), reaching a maximum of -165 mA/mm at

$V_{GS} = -60$ V. By calculating the surface state density and channel carrier mobility of the silicon-terminated MOS structure, it was found that the characteristics of C-Si diamond in device applications are comparable with those based on the C-H diamond channel. The operation of C-Si diamond for MOSFET has not been reported yet. The C-Si diamond which directly connects diamond with SiO_2 , is expected to change diamond electronics more industrial acceptable compared with H-terminated diamond FETs recognized as best diamond FET from the point of RF and high-power applications.

In Chapter IV, successful diamond (111) heteroepitaxial growth on a Ru (0001) // Al_2O_3 (0001) substrate is discussed. The Ru (0001) film was successfully sputtered on Al_2O_3 (0001) by magnetron sputtering. The synthesis of Ru is divided into RF bias nucleation at 450 °C and DC sputtering at 600 °C. X-ray diffraction showed that the Ru film is a high-symmetry film with fine crystal quality (rocking curve FWHM= 1.1°) and a highly orientated (0001) surface. After processing the Ru (0001) // Al_2O_3 (0001) substrate by bias-enhanced nucleation and (111) preferred growth conditions in point-arc remote MPCVD, according to the electron back-scattering diffraction measurement results, there are a large number of diamond nuclei with a diameter of approximately 500 nm oriented (111) on the Ru (0001) surface. The result is applicable for (111) heteroepitaxial diamond for a vertical device.

Chapter V is a summary of the previous chapters. Using point-arc remote MPCVD and SiO_2 masks to achieve the selective growth of high-quality single-crystal diamonds and improve the quality of the selectively grown diamond film. MOSFET fabrication of C-Si diamond provides a simpler and high-performance device manufacturing method and more stable 2DHG operation of FETs. The heteroepitaxial growth of diamond on the Ru

substrate can reduce the synthesis cost of large-area diamond (111) substrates for vertical FETs. The above processes, from substrate production to surface modification to actual device applications, is of great significance to promote the development of diamond crystal growth and high-performance device fabrication.

Table of contents

Selective epitaxial growth of single crystal diamond and its application for high-performance diamond MOSFET fabrication.....	1
Abstract.....	3
Acknowledgement	11
Chapter I General introduction of diamond.....	14
1.1. Wide-bandgap semiconductors.....	14
1.2 Synthetic diamond	16
1.2.1 High pressure high temperature grown diamond.....	17
1.2.2 Chemical vapor deposition grown diamond	18
1.3 Doped diamond.....	26
1.4 Hydrogen terminated diamond	30
1.4.1. Advantages of hydrogen terminated diamonds.....	30
1.4.2 Mechanism.....	31
1.4.3 Carrier distribution.....	34
1.5 Performance of diamond electronic device.....	39
References.....	41
Chapter II selective growth of high-quality single crystal diamond by point-arc remote MPCVD utilizing SiO ₂ mask.....	47
2.1 Selective growth of diamond	47
2.2 point-arc remote plasma MPCVD	49

2.3 Experimental methods	53
2.3.1 Growth condition of diamond growth on Si	53
2.3.2 Diamond substrate preparation	58
2.3.3 Deposition and patterning SiO ₂ mask	59
2.3.4 Selective growth of diamond	60
2.4 Results and discussions	66
2.4.1 Morphology of the selectively grown diamond.	66
2.4.2 Raman spectroscopy	70
2.4.3 Secondary ion mass spectroscopy	71
2.4.4 Cross-sectional transmission electron microscopy	75
2.5 Conclusion	78
References	79
Chapter III Novel diamond MOSFET fabrication process by selectively grown	
source/drain and Si-terminated channel.....	82
3.1 Background	83
3.2 Device fabrication.....	85
3.3 Electrical Characterization of C-Si MOSFET with undoped S/D layer	
.....	94
3.4 Improved characteristic of C-Si diamond MOSFET with p ⁺ S/D layer	
.....	97
3.5 The presence of C-Si diamond.....	103
3.5.1 TEM and EDS measurement of the diamond/SiO ₂ interface	
.....	103

3.5.2 XPS analyses of the diamond/SiO ₂ interface.....	107
3.6 Field effect mobility and interface states density	110
3.7 Conclusion	111
References.....	113
Chapter IV Initial local epitaxial growth of diamond (111) on Ru (0001)//c-	
sapphire by antenna-edge-type microwave plasma chemical vapor deposition ..	116
4.1 Heteroepitaxial growth of diamond	117
4.2 Experimental process	119
4.3 Crystallographic characterization of ruthenium on c-sapphire.....	123
4.4 Morphologies of diamond (111) on Ru (0001)//c-sapphire.....	125
4.5 Crystallographic characterization of diamond on Ru (0001)/c-sapphire	
.....	126
4.6 Conclusion	129
References.....	130
Chapter V Summary	133
Appendix A MOSFET fabrication process detail.....	136
Appendix B	140
List of research achievements for application of doctorate (Dr. of	
Engineering), Waseda University	141
Referee's signatures	142

Acknowledgement

Firstly, I would like to express my sincere gratitude to my advisor Prof. Dr. Hiroshi Kawarada, the leader of Kawarada Laboratory, for the continuous support of my Master and Ph.D studies, for his patience, motivation and immense knowledge. He helps me so much from the master course application to my Ph.D graduation. His supervision and guidance helped my research head the correct direction and go deeper. Besides the research contents, the most important thing I learned from him is how to think logically. He always intentionally trains my independent thinking and corrects my mistakes in time. I could not have imagined having a better advisor and mentor for my Ph.D study. The thesis would not have been possible without the help, support and patience from him.

I also would like to thank Dr. Masafumi Inaba and Dr. Taisuke Kageura for bringing me into the field of carbon materials, teaching me the experimental details and helping me do the analysis when I am a newbie in this field.

Mr.Te Bi, Ms. Haruka Hoshino, Mr. Masayuki Iwataki, Mr. Shoichiro Imanishi, Ms. Aoi Morishita, Mr. Yu Fu and Mr. Benjian Liu, thank you all for being the same research team with me. Without your efforts and opinions, we could not smoothly process all the research topics. The happy and hard time we spent together in doing researches together is unforgettable to me.

Many thanks to Prof. Dr. Hongxing Wang, Mr. Kongting Wei and Ms Fei Li for providing me to use the magnetron sputtering system and XRD equipment in Xi'an Jiao'tong University. The deposition of high-quality ruthenium film and the XRD analysis played an important role in this thesis and your kind help are greatly appreciated.

I am thankful of my fellow laboratory members through my five years in Kawarada Laboratory who have taught me how to use the laboratory instruments and for the interesting and useful talking on my work. I am grateful to have had the opportunity to work with you all.

I would like to thank the Kagami Memorial Research Institute for Materials Science and Technology, Mr. Shinpei Enomoto for analyzing and providing me to use TEM and EDX. Without your kind help, I could not finish my research smoothly.

The help from our secretary Hisako Nishiki also be great appreciated. She helped me a lot to finish complicated documents. Her fully support made it possible for me to spend more time in doing my research.

I would also like to thank my committee members, Professor Shuichi Shoji, Professor Takashi Tanii and Professor Takanobu Watanabe for serving as my committee members even at busy period. Thanks to their insightful comments and encouragement, but also for the hard questions which incented me to widen my research from various perspectives.

Finally, I would like to thank my parents for their unconditional love and support throughout my life, I would not have been able to complete my study in Japan without their continuous love and encouragements. I would like to thank my husband Ti for his love

and constant support. He is the right partner who makes all the difference in my life. This thesis would not have been possible without him.

Chapter I General introduction of diamond

1.1. Wide-bandgap semiconductors

At present, electric energy supplies nearly 40% of the global energy consumption. From the generation of energy to its distribution to users, power electronics plays a key role in power generation, storage, and transmission.¹ In recent times, mature silicon power devices have dominated the power electronics equipment market. However, large energy losses occur due to Si-based power devices in semiconductor devices. Commercial silicon devices have undergone decades of development. As the technology mature, the physical limitations of silicon devices in terms of breakdown voltage, operating temperature, and switching frequency become increasingly obvious. These limitations will degrade the performance of the high-power, high-temperature, and high-frequency silicon devices, rendering them incapable of meeting the needs of low energy consumption for the next-generation of power devices.²

Wide-bandgap (WBG) semiconductor materials are expected to achieve improved power conversion efficiency while reducing the size of the power devices. WBG materials usually have high thermal conductivity, which allows them to operate at high temperatures without requiring considerable cooling systems. The WBG enables the material to achieve

a large breakdown voltage and lower conduction resistance under thin epitaxial layers. High saturation speed of the material is expected to result in high-frequency switching of power devices.³

Various applications of WBG power devices are shown in **Figure 1.1**.¹ In case of low-voltage applications below 600 V, power devices are mainly used in various household appliances. In medium and high voltages of 600-1200 V, WBG power electronics are mainly used for AC/DC conversion of inverter/converter in electric vehicles and hybrid vehicles. In high-voltage fields above 1200 V, they are used in industrial applications, renewable energy, and transportation.

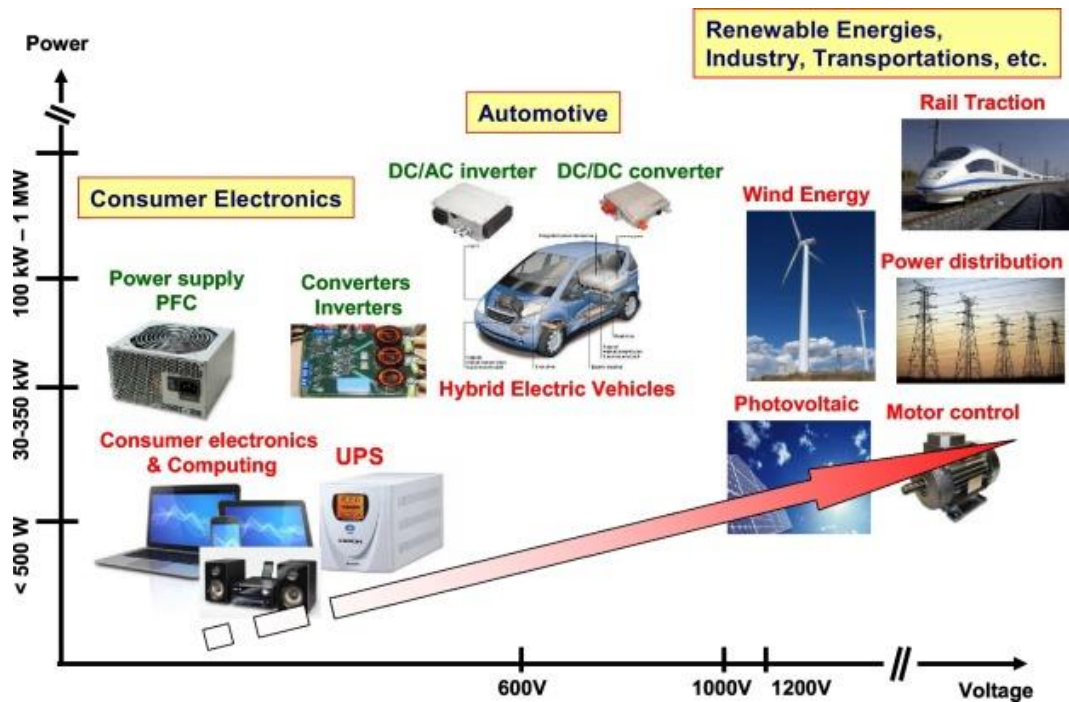


Figure 1.1 Major applications of WBG power devices in a plot of power vs operation voltage range.¹ (reuse permitted)

With respect to other WBG materials, diamond not only has a maximum band gap of 5.5 eV, but also has many excellent properties. Its highest thermal conductivity and high melting point at RT can reduce the heat dissipation area of power electronics, the breakdown voltage of up to 10 MV/cm makes it suitable for high-voltage-resistant devices. the carrier mobility ($4500 \text{ cm}^2 \text{ V}^{-1} \text{ s}^{-1}$ for electrons, $3800 \text{ cm}^2 \text{ V}^{-1} \text{ s}^{-1}$ for holes) and saturation carrier drift velocity make it suitable for high frequency devices. Diamond and other current WBG semiconductor materials are shown in Table 1.1, where pink indicates less maturity of the power device applications.⁴

Parameter	Diamond	c-BN	β - Ga ₂ O ₃	AlN	GaN	SiC	GaAs	Si
σ_{thermal} (W/m•K)	2290 - 3450	940 - 2145	11 -27	317	253	370	55	145
e ⁻ mobility (cm ² /V•s)	4500	825	180	426	2260	900	8500	1450
Hole mobility (cm ² /V•s)	3800	500	--	--	24	120	400	480
E _{br} (MV/cm)	~13.0	~ 17.5	~ 10.3	~ 15.4	~ 4.9	~ 3.0	~ 0.4	~ 0.3
V _{sat} (10 ⁷ cm/s)	2.3(e ⁻) 1.4(h ⁺)	--	1.1	1.3	1.4	2.0	1.0	1.0
Rel. permittivity	5.7	7.1	10.0	9.8	10.4	9.7	12.9	11.8
maturity								

Table 1.1 electric properties of current WBG semiconductor materials where pink implies less maturity. ⁴(reuse permitted)

1.2 Synthetic diamond

Natural diamonds are mostly aged between 130 and 300 million years. Under the conditions of high temperature and high pressure in the mantle layer, carbon-containing fluids dissolve and transform into stable crystals, which are transported with the magma to

the surface by geological movement. Since the semiconductor properties of diamonds are affected by the crystal quality, natural diamonds cannot fulfill the repeatability quality or the availability in large sizes. In addition, the limited size and high price also make it unsuitable for the industry. Owing to the need for stable bulk synthesis of diamonds with tight budgets, the technology of graphite synthetic diamond has emerged. At room temperature and pressure, diamonds are dynamically stable and not thermodynamically stable. In the same environment, however, graphite is the most stable carbon allotrope, which is common in nature and therefore, inexpensive. Owing to its activation barrier, it is difficult for graphite to spontaneously convert into a diamond. Therefore, researchers have attempted to synthesize diamonds in a more stable environment, with high temperature and high pressure.

1.2.1 High pressure high temperature grown diamond

The HPHT method is a synthetic method that simulates the conditions required for the formation of natural diamonds at high pressure (5.5-8.0 GPa) and high temperature (1000-1400 °C) that are prevalent close to the earth's core (140-240 km).⁵ Graphite is put into a hydraulic press and compressed under high pressure and high temperature conditions to form a diamond catalyzed by metals. Although HPHT is the earliest method for synthesizing diamonds, it is still widely used in the industry because of its low cost. The first laboratory synthesized diamond was reported by Bundy et al..⁶ After several years of effort, they finally developed a device that can maintain the temperature and pressure of the diamond in a stable state for several hours. The synthesized diamond has the same hardness and crystal structure as a natural diamond. Relatively pure single-crystal diamond desirable for jewelry and heat sink of power device can be produced by HPHT method.

1.2.2 Chemical vapor deposition grown diamond

The chemical vapor deposition (CVD) method is favored by researchers as it can synthesize high-quality single-crystal diamond films with precisely controllable thickness. CVD is a method that decomposes the hydrocarbon gas mixture into active groups and deposits the diamond on the substrate under specific conditions. In contrast to HPHT, the CVD method has the advantage of being able to synthesize large-scale and high-quality diamonds on various substrates and can accurately control the impurities and properties of the synthesized diamond. The first CVD-synthesized diamond was reported by Spitsyn et al. in 1981.⁷ They demonstrated that the CVD method, under reduced pressure, used atomic hydrogen to inhibit the crystallization of graphite, and successfully ensured the selective growth of diamond. In a typical CVD process, the hydrocarbon (usually CH₄ gas) provides a carbon source for diamond growth, while H₂ play critical role in initiating reaction between gas phase radicals and surface sites. There are many ways to excite the reaction gas into active groups, such as the thermal method, electric discharge method (e.g., DC, RF, or microwave), or a combination flame (such as an oxygen type torch). **Figure 1.2** shows four major CVD apparatuses. Although they differ in structure, some of the basic growth conditions are the same. For example, to ensure the growth of the diamond, the hydrocarbon gas will be diluted to less than 1% by hydrogen and in order to prevent the formation of amorphous carbon, the substrate temperature is usually above 700 °C.⁸

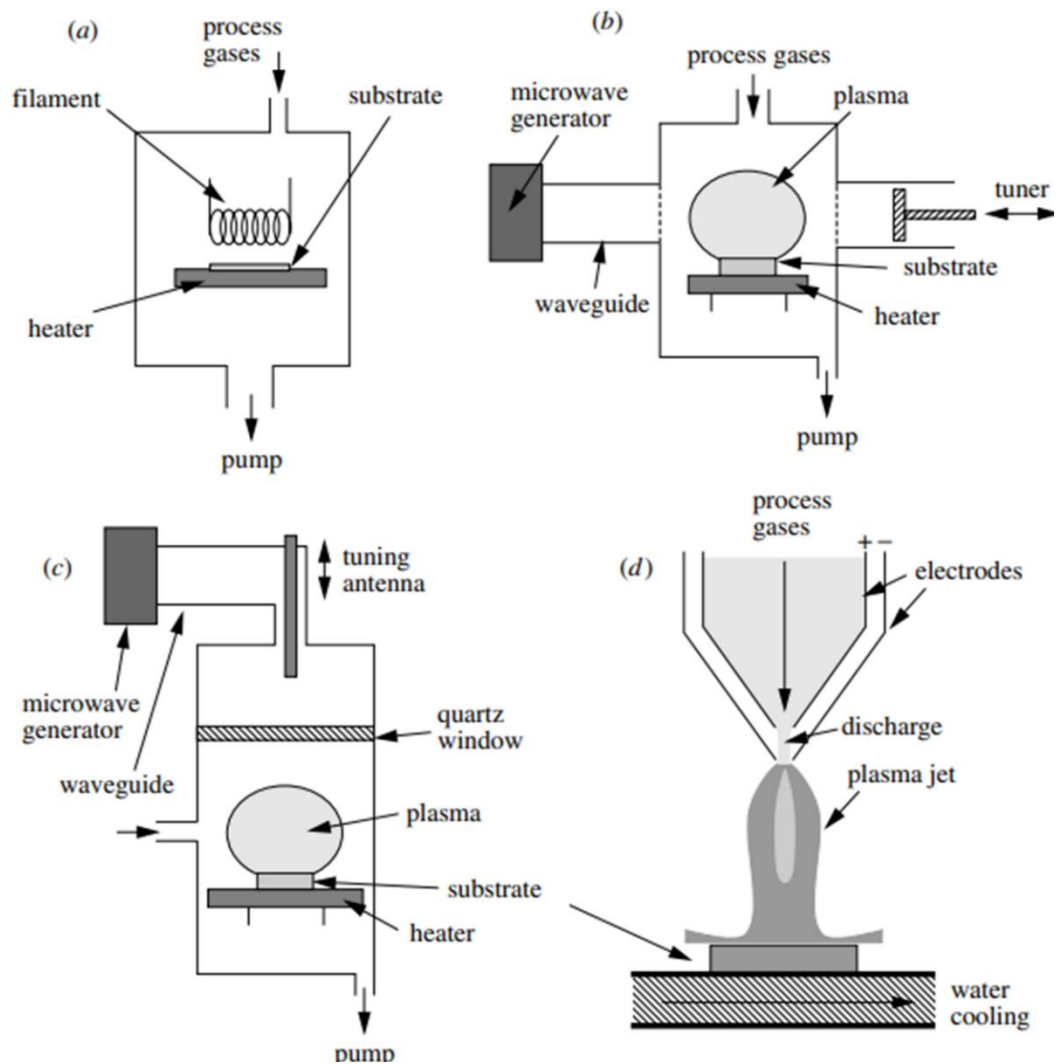


Figure 1.2 Structure diagram of four common types of CVD reactors (a) Hot filament (b) Quartz type microwave plasma reactor (c) Cylinder cavity type microwave plasma reactor (d) DC arc jet (plasma torch)⁸ (reuse permitted)

Hot filament chemical vapor deposition (HFCVD) is suitable for low-cost large-size film formation and is mostly used in the synthesis of large-size polycrystalline diamonds. W, Ta, and Re as metal filaments are usually heated to more than 2000 °C, the substrate is heated to 700-900 °C on the heater a few millimeters below the filament (shown in **Figure 1.2** (a)), and the pressure in the reaction chamber is 20-30 Torr. The deposition

rate can reach several microns per hour. The disadvantage is that the filaments can undergo carburization resulting in uncontrolled contamination of the diamond. During the deposition, the filament and carbon-containing reactive species are carburized, and the carbon atoms diffuse in the metal lattice, forming metal carbide that will change the electrical conductivity of the filament and render the metal filament inactive, thus interrupting the reaction. Carburization affects the life of the filament and shortens the time of single diamond deposition.^{9,10}

Microwaves are coupled to the reaction chamber through the dielectric window to cause a discharge, and then, the energy is coupled to the gas phase electron by the microwave. Finally, the energy is transferred to the gas molecules through the collision. The gas molecules dissociate to form active groups and then deposit on the substrate. The quartz type (shown in Fig. 1.2(b)) and cylinder cavity type (shown in Fig. 1.2(c)) are the two most common microwave plasma reactors. quartz type was designed by the National Institute for Research in Inorganic Materials (NIRIM) in the 1980s. It uses a discharge quartz tube with a diameter of approximately 5 cm, vertically placed at the antinode of the maximum amplitude of the electromagnetic wave propagating in the microwave waveguide of 2.45 GHz, which forms a stable plasma. The sample holder is usually made of Mo or quartz, placed at the center of the cross of the waveguide and quartz tube. As a mean to achieve high-density plasma, which is fierce and suitable for doping, the holder is designed to be conducive to the shape of the plasma concentration. The area where the plasma occurs is placed in the center of the intersection of the quartz tube and the waveguide, as the shape of the holder changes. The location of the plasma formation can be tuned by plunger.

The cylinder cavity type reactor is effective for large area diamond deposition with high quality. In this reactor, the microwave is coupled to the metal cavity with a water-cooling system through the dielectric window, and the TE₁₀ mode microwave is converted into TM₁₀ by the antenna. A certain cavity diameter maintains the radial mode of the microwave at 2.45 GHz. The substrate placed on the heater with a diameter of more than 10 cm is immersed in the plasma ball. Under a maximum power of 5 kW, the growth rate of diamond can exceed 10 $\mu\text{m h}^{-1}$.

As shown in Fig. 1.3, hydrocarbon gas (CH_4 or C_2H_2 is widely used) introduced into the reaction chamber is diluted to approximately 1% with hydrogen. The mixture gas is activated by plasma dissociation, splitting into atomic hydrogen and hydrocarbon radicals (C_xH_y). Although several kinds of stable hydrocarbon radicals have been monitored by optical diagnosis¹¹⁻¹⁵, methyl radical (CH_3) has been intensively investigated due to its significant abundance in the gas phase. Hereafter, the CH_3 will be discussed as the representative radical C_xH_y during the CVD process. Atomic hydrogen, being the most abundant radical, plays a critical role in reactions between gaseous radicals and surface sites.¹⁶⁻¹⁸ Hydrogen abstractions initiates the addition of CH_3 to diamond surface, creating surface radical sites for CH_3 deposition, stabilizing diamond phase. The abstraction can be driven by gas phase hydrogen to for molecular hydrogen, it is also feasible to be abstracted by growth species with similar energy.

Diamond (100) surface is relatively economically and technically approachable, most of the work on studying the reactions on diamond surface is based on the reactions occurring upon the hydrogen terminated diamond (100) surface which is featured with 2×1 reconstruction.

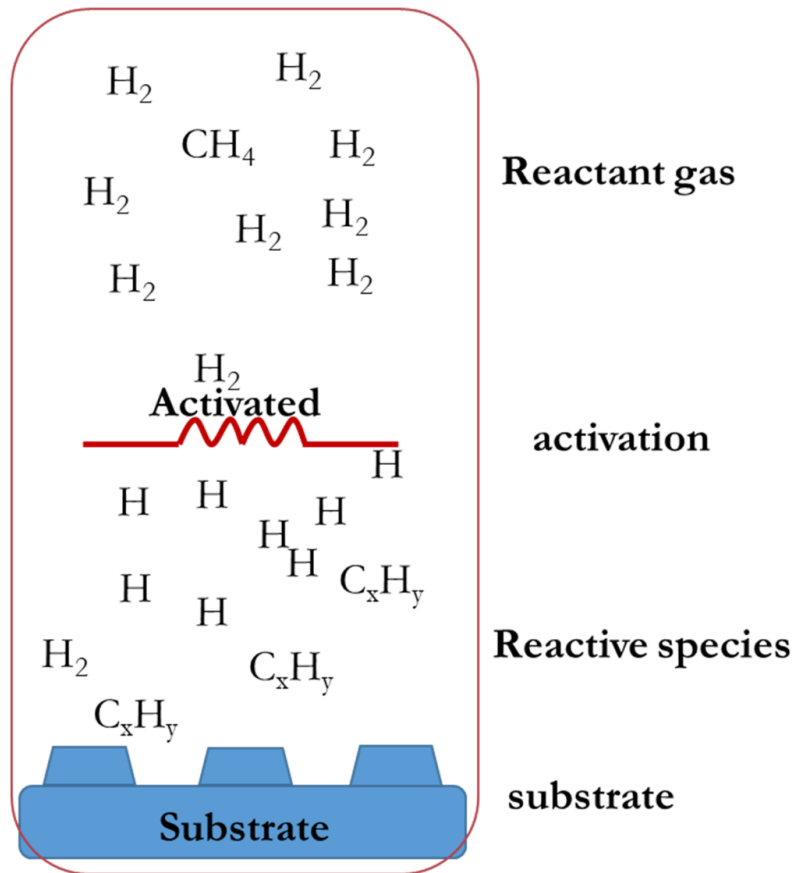


Figure 1.3 Schematic of chemical and physical processes during CVD synthesis of diamonds.

In an ideal infinite crystal, the equilibrium position of each individual atom depends on the force exerted by all other atoms in the crystal, thus forming a periodic structure. If the crystal is terminated along a given plane, the force alters, thus changing the equilibrium position of the remaining atoms. The atoms on the surface and near the surface are most affected and will form different structures from bulk atoms. As for the (100) surface of diamond, there is the original 1×1 square lattice with two dangling bonds for each carbon (shown in Fig. 1.4(a)). However, 2×1 reconstruction was observed on the homoepitaxial diamond (Fig. 1.4(b)), the surface carbon atoms form monolayer dimers, resulting one of the two dangling bonds removed and another one terminated by hydrogen atom.^{19,20}

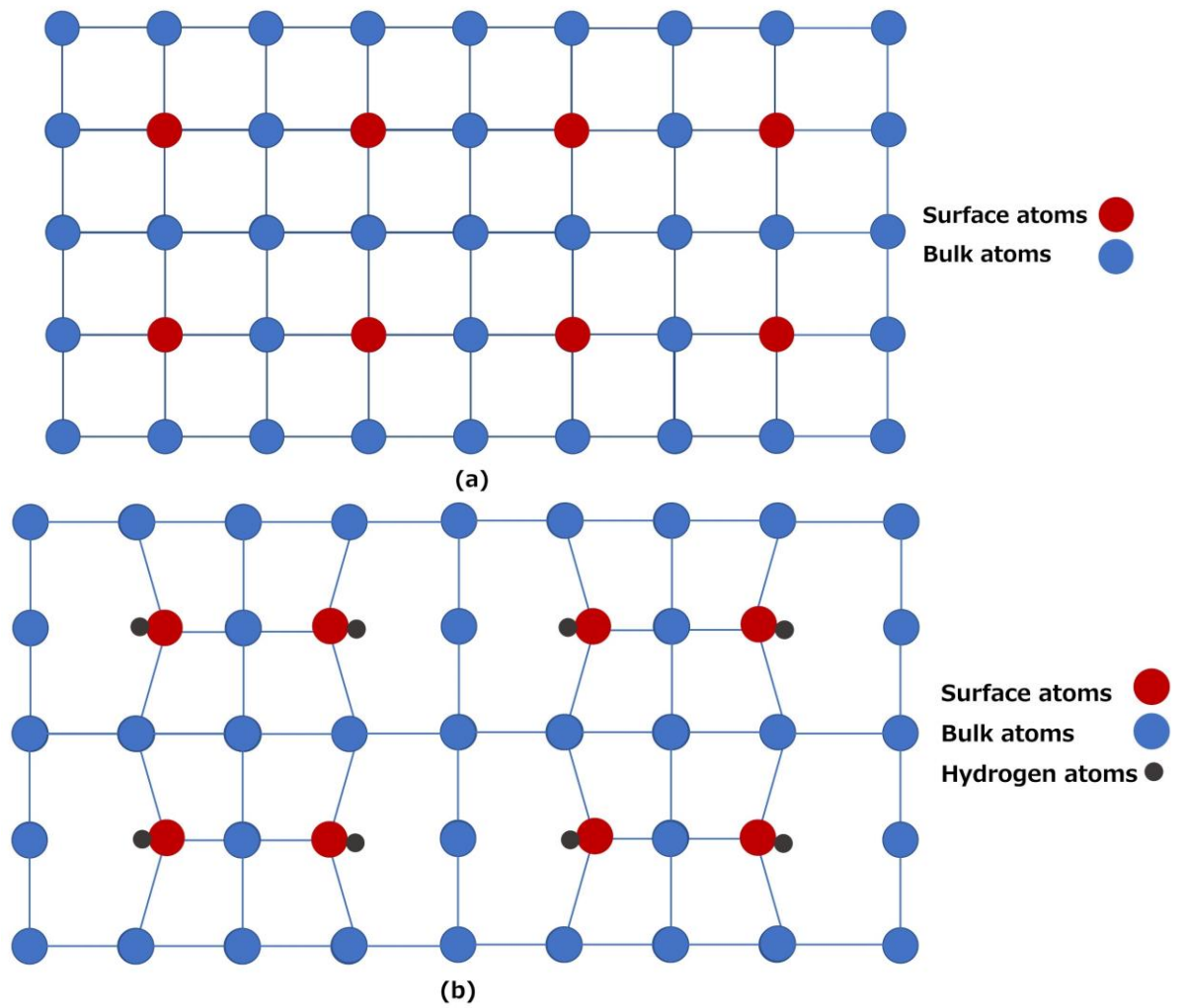


Figure 1.4 Top view of (a) an ideal diamond (100) surface and (b) 2×1 reconstruction overserved of the homoepitaxial diamond (100).

According to the well-investigated review of Butler's group,^{17,21} reactions between gaseous radicals and surface sites can be interpreted briefly as followings: after crossing the activation area, CH₃ radicals diffuse from the gas phase towards to the diamond surface. The homoepitaxial diamond (100) 2×1:H reconstructed surface is shown in Fig. 1.5(a). The surface-active site (dangling bond) formed by hydrogen desorption is essential for CH₃ addition to the diamond surface. The pendant hydrogen atom can be abstracted by the gas phase, but it can also be abstracted by the hydrocarbon radicals with similar energy.²¹ the CH₃ added to diamond surface will form C-C bond at the reconstructed dimer. The hydrogen atom bounded to surface carbon is desorbed back to gas phase, leaving a dangling bond for subsequent CH₃ addition (Fig. 1.5(b)). CH₃ forms a C-C bonding by adding to the dangling bond (b→c). Next, one of the hydrogen atoms desorbed from the pendant CH₃ (c→d). Because of the larger energy barrier (~200 kJ/mol) of direct insertion into the C-C bond, the newly formed pendant CH₂ involving into the diamond formation though a ring opening reaction is much energetically favorable (e→f).^{22,23}

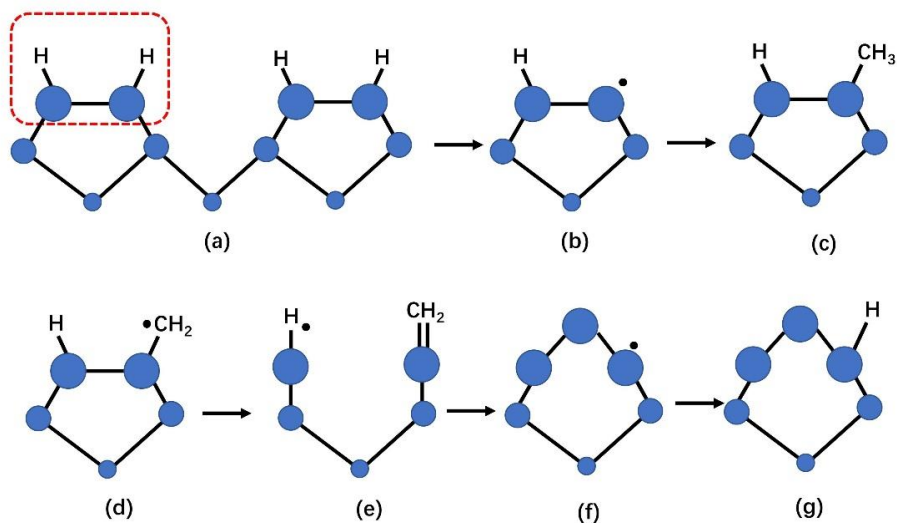


Figure 1.5 The mechanism for the process for CH_3 insertion into the dimer bond on $(100) 2 \times 1\text{-}2\text{H}$ surface. (Side view)

1.3 Doped diamond

Since intrinsic diamond is an insulator, the key issue for the use of diamond in electronics is the generation and control of its conductivity. The following contents mainly introduce two methods of making diamonds conductive: doping and hydrogen termination.

For p-type doping, boron is the only atom known to replace carbon atoms in diamond crystals to form acceptors. The mobility of a natural diamond with high crystal quality, containing boron impurities, can reach $2000 \text{ cm}^2 \text{ v s}^{-1}$ at RT. When applied to semiconductor devices, precise control of conductivity is essential. By suppressing the impurities mixed with diamonds that are caused by the residual gas in the reaction chamber, high-quality single-crystal diamonds can be obtained by low-pressure CVD growth. At the same time, by adjusting the proportion of boron-containing gas to carbon-containing gas,

boron doping at different concentrations can be achieved, and diamond conductivity can be accurately controlled.

Microwave plasma CVD provides high reproducibility and homogeneous quality of homoepitaxial boron-doped growth of diamonds. Typical doping growth conditions are as follows: methane concentration below 1%, reaction pressure of 20-50 Torr, and boron concentration (B/C) of 1000 ppm or less. Trimethylborane ($\text{B}(\text{CH}_3)_3$) is usually used as a dopant gas. Common crystal surfaces (100) and (111) can achieve almost 100% boron coverage. For the (100) surface, boron concentration (C_B) decreases with increasing methane concentration. However, under the same doping conditions, the doping of the (111) surface is approximately one order of magnitude larger than that of the (100) surface. Homoepitaxially grown boron-doped diamond (100) synthesized by microwave plasma CVD can easily reach a carrier mobility of $1000 \text{ cm}^2 \text{ v s}^{-1}$ at RT.²⁴⁻²⁶ However, HPHT grown boron-doped diamond (111) suffers from low carrier mobility, which has not been reported to go over $1500 \text{ cm}^2 \text{ v s}^{-1}$ yet.

The activation energy exceeding 370 meV is a major disadvantage of the boron-doped diamond when it is applied in electronics. An activation rate of less than 0.1% at RT results in relatively high resistivity (specific resistivity over $10 \text{ } \Omega\text{-cm}$) of boron-doped diamond. Although higher conductivity requires a higher boron concentration, an excessive doping concentration will reduce mobility. For example, a homoepitaxial film with an acceptor concentration of over 10^{18} cm^{-3} has a mobility of approximately $100 \text{ cm}^2 \text{ v s}^{-1}$. However, if the acceptor concentration continues to increase, the conductance rises due to impurity conductance domination. The lightly boron-doped ($C_B \approx 10^{17} \sim 10^{19} \text{ cm}^{-3}$) diamond synthesized by CVD exhibits conductivity with an activation energy of 0.35 eV. When C_B

increases over 10^{20} cm^{-3} , the diamond shows metallic conductivity at RT.²⁷ Until now, the use of boron-doped diamond as channel FET has not yet achieved satisfactory results. Heavily boron-doped diamond is temporarily used mostly to improve the ohmic contact between the diamond and the metal.^{28,29} Heavily boron-doped (p^+) diamonds may even exhibit superconducting properties. At present, superconductors with a superconducting temperature above 25K have been realized on p^+ ($C_B > 3 \times 10^{20} \text{ cm}^{-3}$) diamond.³⁰

The n-type doping of diamonds remains a huge challenge. For silicon, n-type doping can usually be achieved by thermal diffusion, ion implantation, vapor phase growth, etc. However, for diamonds, the thermal energy diffusion method is not easy to realize because the binding energy between carbon atoms is too large while the lattice constant is relatively small. Defects generated during ion implantation are difficult to recover through annealing, and it is difficult to replace the carbon atom with the dopant atom. Although there have been a few reports of n-type doping, there is a lack of conclusive evidence of activated carriers, so the applicable n-type doping has not yet been achieved. Currently, diamond n-type doping is achieved by introducing dopant gas during vapor-phase growth.

Due to the deep energy donor (P 0.36 eV, N 1.7 eV), the conductivity of N-doped diamond is almost negligible at RT. From the perspective of the covalent bond radius, the nitrogen element (0.74 Å) is closer to that of carbon (0.77 Å), but the local lattice distortion of the nitrogen at the substitution position causes the substitution position to shift, leading to an extremely deep activation energy. Therefore, the nitrogen donor negligibly contributes to any conductivity at RT. Phosphorus is considered a potential candidate for n-type doping because its energy level is lower than that of nitrogen. The n-type doping is independent of orientation and has been achieved on both the (100) and (111) surfaces.

The conductivity of phosphorus-doped diamond was confirmed by van der Pauw measurement. The n-type conductivity was confirmed when the phosphorus concentration (C_P) was above 10^{16} cm^{-3} in the temperature range of 300-873 K. When $C_P < 10^{16} \text{ cm}^{-3}$, there is no conductivity detected at RT.³¹ In the case of (111) diamond, when C_P is $7 \times 10^{16} \text{ cm}^{-3}$, the carrier concentration and the specific resistance at RT are $5 \times 10^{10} \text{ cm}^{-3}$ and $2 \times 10^5 \text{ } \Omega\text{-cm}$, respectively. At 873 K with the same C_P , the carrier concentration and the specific resistance are $6 \times 10^{16} \text{ cm}^{-3}$ and $2 \text{ } \Omega\text{-cm}$, respectively. The increase of carrier concentration and decrease of specific resistance as temperature increases suggest that the conductivity is derived from band transfer and is activated thermally.

1.4 Hydrogen terminated diamond

1.4.1. Advantages of hydrogen terminated diamonds

Since diamonds exhibit favorable properties for electric devices, developments have been undertaken on diamond-based bipolar transistors, metal semiconductor field effect transistors (MESFETs) metal insulator semiconductor FETs (MISFETs) since the late 1980s.³²⁻³⁴

However, the performance of these diamond devices does not meet the expectations of the physical properties of the diamond block due to various reasons. The first reason is low carrier concentration under RT caused by deep acceptor boron doping, resulting in poor performance of the MOSFET. The second reason is the difficulty in controlling the carrier due to strong surface states existing on the pristine or oxidized diamond surface. The third is the high Schottky barrier height (SBH) due to poor ohmic contact.

In 1989, the hydrogen-terminated diamond was found on a CVD as-grown film displaying low resistivity ($10^6 \Omega\text{cm}$).³⁵ In 1994, Kawarada et al. reported the enhancement mode MESFET based on the control of surface p-type conduction of a hydrogen-terminated homoepitaxial layer without a doping channel.³⁶ The distinguishing properties of hydrogen-terminated diamond, such as high hole density (up to 10^{13} cm^{-2}),³⁷ low activation energy (less than 50 meV),³⁷ shallow carrier distribution ($<10 \text{ nm}$),^{37,38} are desirable for carrier control; low SBH to form ohmic contact,^{36,39} low density of surface state ($<10^{11} \text{ cm}^{-2}$),⁴⁰ and high hole mobility (above $100 \text{ cm}^2 \text{ v}^{-1} \text{ s}^{-1}$)^{41,42} are advantageous for the field effect. Thus, excellent performance has been achieved for hydrogen-

terminated diamonds, resulting in high current output,^{41,43-45} high-frequency operation,⁴⁶ wide temperature range operation,⁴⁷ and high breakdown voltage.^{48,49}

1.4.2 Mechanism

The two representative terminations: hydrogen termination and oxygen termination possess significantly different properties. Hydrogen termination shows thermal stability up to a temperature of 600 °C in vacuum and starts to desorb above this temperature.⁵⁰ In the typical diamond plasma-assisted CVD growth environment, hydrogen contributes to etch non-diamond and stabilized sp³. Hydrogen termination can be reproducibly generated by exposure to hydrogen plasma after growth. It can also remain after the deposition of metals or insulators.

On the other hand, a depletion layer for holes is generated in oxygen-terminated diamonds, due to donor-type surface states existing at 1.7 eV above the valence band,⁵¹ exhibiting insulating properties. The transformation from hydrogen termination to oxygen termination occurs at 350 °C under atmospheric pressure or at 350 °C under strong acid. Atomic layer deposition (ALD) oxidation makes the manufacture of electronic materials with diamonds easier and more efficient compared to doping.^{52,53} Unlike the oxidization of Si, the oxidization of diamond stops at the monolayer on the surface, resulting in carbon atoms terminated by oxygen.

In 1989, unlike the boron-doped diamond which was bulk conductive, the subsurface of as-grown diamond film was found to display low-resistivity conductivity by Landstrass et al.³⁵ The Seebeck effect measurement was conducted by Maki et al. on the as-grown diamond to reveal the p-type conductivity existing near the surface.⁵⁴ RF FET with considerable transconductance were fabricated by Kawarada's group,⁵⁵ characterized

by Hall effect measurement. Hayashi et al. suggested that the carrier density induced by H-termination is 10^{13} cm^{-2} .³⁷ The band bending caused by acceptor-like surface states below the bulk Fermi level has been suggested by Kelvin probe measurement, which contributes to the hole accumulation near the surface.⁵¹

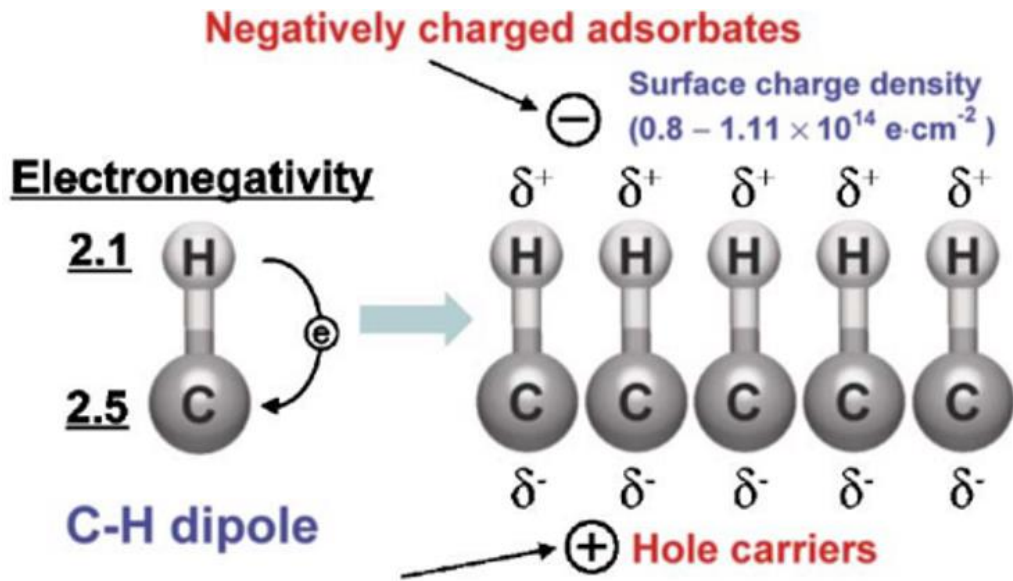


Figure 1.6 Spontaneous polarization of C-H dipole occurring on the H-terminated diamond surface caused by different electronegativities - the electronegativity of C is 0.4 Pauling unit higher than H. The negatively charged adsorbate induces the formation of hole carriers with p-type conductivity.⁵⁷(reuse permitted)

In terms of electronic properties, H-termination displays shallow p-type conductivity, while O-termination exhibits insulating behavior as a clean diamond surface. The electronegativities of C, H and O are 2.6, 2.1 and 3.5, respectively. The surface potential gap over 1.0 eV, caused by the difference in electronegativities, leads to distinct polarizations of C-H dipole and C-O dipole. The C-H dipole (Fig.1.6) is electrically positive with negative electron affinity while the C-O is negative with positive electron affinity.^{56,57}

Several models have been proposed to interpret the mechanism of p-type conductivity induced by H-termination, which is still controversial. Based on the analysis of the H profile by secondary ion mass spectroscopy (SIMS), Hayashi et al. declared that the acceptors are caused by the hydrogen atom incorporated into the region that is 20 nm beneath the surface.³⁷ Kawarada et al. observed the existence of empty surface states near the valence band maximum and proposed a band bending model caused by the existence of acceptor-like surface states.¹⁹

Since the subsurface conductivity induced by hydrogen termination shows strong dependence of the atmosphere it exposed to, it has been widely accepted that the presence of H-termination is a necessary but not sufficient condition for hydrogen-terminated diamond, and additional adsorbates also contribute to the conductivity.⁵⁸ In 1995, Gi et al. found that the oxonium ion (H_3O^+) reacted with hydrogen-terminated diamond, causing hole accumulation.⁵⁹ The difference in chemical potential causes the electrons to transfer from the hydrogen-terminated diamond with negative electron affinity to the lowest unoccupied molecular orbital (LUMO) of the acceptor material, which is accepted as the transfer doping theory.⁶⁰ It has been reported that the stability of the subsurface conductivity can be considerably increased by using materials with high electron affinity such as transition metal oxides.⁶¹⁻⁶³ Combining the surface acceptor and transfer doping, Nebel and coworkers claimed that localized states caused by surface disorder and adsorbates with negative charge are the sink for electrons from the valence band.⁶⁴

1.4.3 Carrier distribution

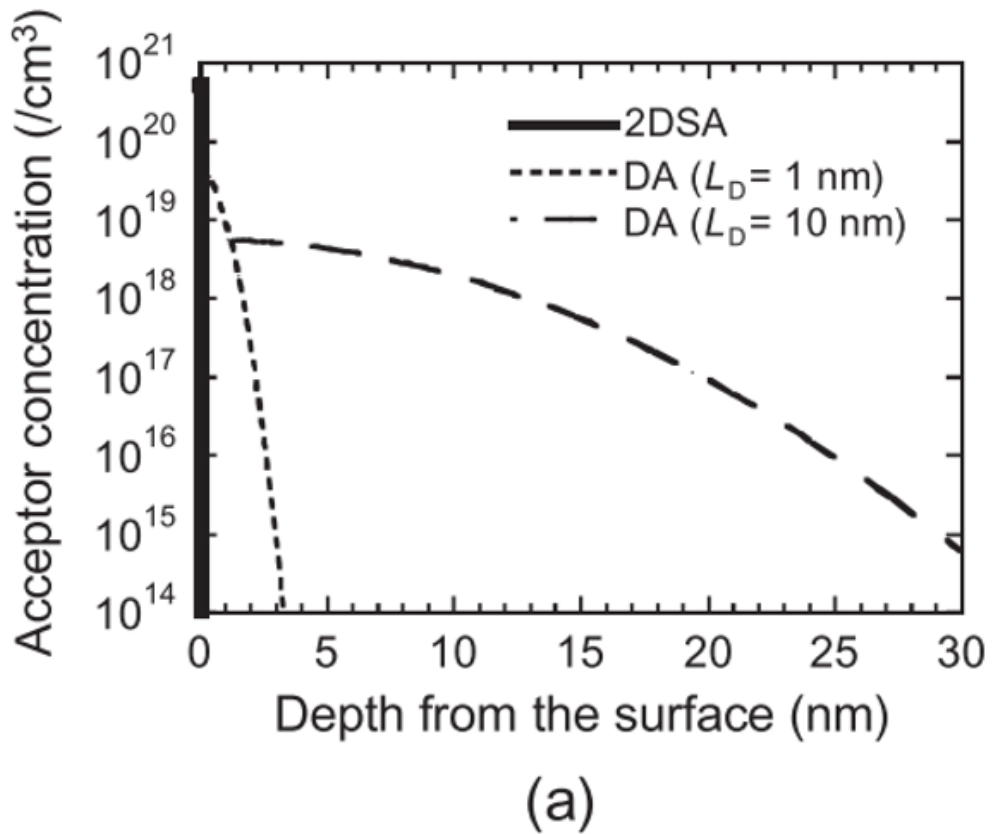
Tsugawa et al.^{38,65} adopted two models to present the p-type surface channel in hydrogen-terminated diamond MESFET/MOSFET: two-dimensional surface acceptor model (2DSA), in which the acceptors are assumed to be distributed two-dimensionally on the diamond surface and the diffused acceptor model (DA), where acceptors are distributed three-dimensionally in the subsurface region, following the Gaussian function profile with a diffusion length of 1~ 10 nm.

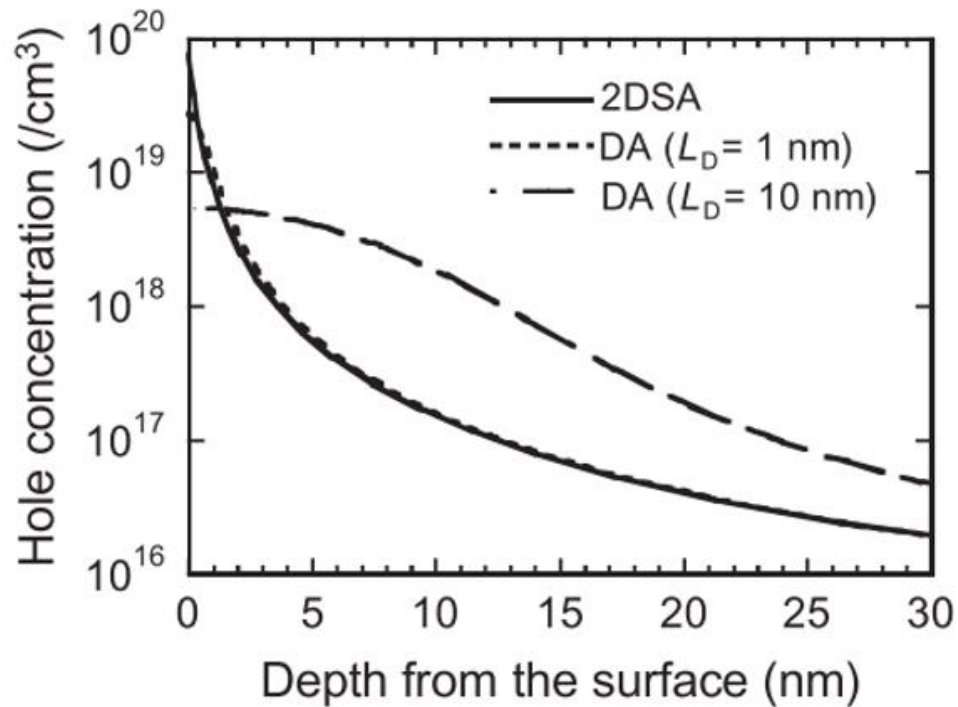
In the former model, it was assumed that the H atom on the surface contributes to the p-type conductivity, and the influence of those incorporated into the subsurface region is negligible. An ultra-thin layer (0.2 nm) with fully activated acceptors was placed on the intrinsic diamond surface. The acceptor density was $5 \times 10^{20} \text{ cm}^{-2}$, corresponding to a hole concentration of $1 \times 10^{13} \text{ cm}^{-3}$ obtained by Hall measurement.³⁸

$$C(x, L_D) = \frac{2Q}{\sqrt{\pi}L_D} \exp\left(-\frac{x^2}{L_D^2}\right)$$

Here, $C(x, L_D)$ is the acceptor concentration at depth x , and L_D (1 ~ 10 nm) is the diffusion length. Q represents the total dose integration of the acceptor concentration along the depth direction. This model indicates that the H atoms incorporated into the subsurface region diffuse to the bulk and provide holes as acceptors.³⁸

Figure 1.7⁶⁵ shows the acceptor and hole distribution profiles of 2DSA and DA with L_D of 1 nm and 10nm, respectively. In **Figure 1.7(a)**, the acceptor of 2DSA only exists on the surface for the DA mode, where the hole distributions at depths of 1 nm and 10 nm are plotted as dotted and long dash signs. The hole concentration calculated under thermal equilibrium conditions at 300 K at a depth of 10 nm drops three orders of magnitude from that at the surface. The hole concentration of 2DSA coincided with the DA with $L_D = 1$ nm except for the depth within 1 nm beneath the surface, in which the hole concentration of the former is double that of the latter.





(b)

Figure 1.7 Acceptor (a) and hole (b) profiles of 2DSA and DA with $L_D = 1$ nm and 10nm along depth direction. The hole distributions are calculated under the thermal equilibrium at 300 K.⁶⁵ Copyright (2001) The Japan Society of Applied Physics

Compared to the metal insulator semiconductor FET (MISFET), which has a more complicated architecture including a gate insulator, the simulation of the MESFET with p-type surface conductive channel⁶⁵, which reproduces the device characteristics, provides a reliable approach for investigating surface conductivity. The DC characteristics of this MESFET with Pb-gate were simulated by varying the acceptor distribution using distinct distribution models. In this method, the dependence of the DC characteristics, i.e., threshold voltage (V_T), was investigated. **Figure 1.8** shows the architecture of the simulated MESFET. The Pb-gate contact characterization⁶⁶ and fabrication of this MESFET⁶⁷ have been provided in the previous work. The DC characteristics suggested that the V_T range

from -0.1 to -0.6 V, no normally-on operation ($V_T > 0$) have been found. In **Figure 1.9**, the sheet hole density versus the V_T of the simulated MESFET was plotted for various acceptor distributions. Since the sheet resistance of the hydrogen-terminated diamond varies from $\sim 10 \text{ k}\Omega/\square$ to $\sim 10 \text{ k}\Omega/\square$, the hole density is thought to vary by an order of magnitude of 10^{12} cm^{-2} to 10^{13} cm^{-2} . As shown in **Fig. 1.9**, when the hole density varies from 10^{12} to 10^{13} cm^{-2} , only the simulation of 2DSA and DA with $L_D = 1 \text{ nm}$ reproduced the actual V_T variation of -0.1 to -0.6 V, while the DA with L_D of 5 nm and 10 nm showed high sensitivity to the hole density, exhibiting normal characteristics when the hole density is just over $1 \times 10^{13} \text{ cm}^{-3}$.

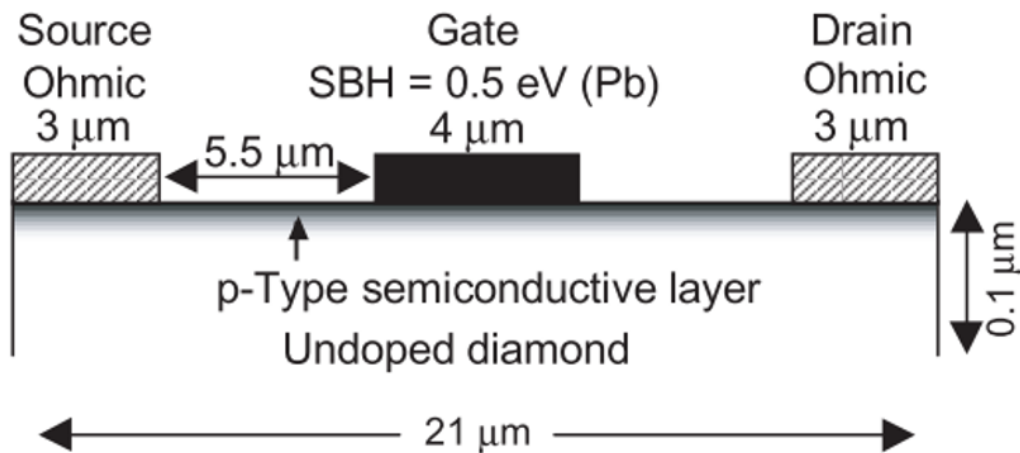


Figure 1.8 cross-sectional schematic diagram of the simulated diamond MESFET. The device composed of Pb gate, which has a SBH of 0.5 eV at the interface of Pb/diamond.⁶⁵ Copyright (2001) The Japan Society of Applied Physics

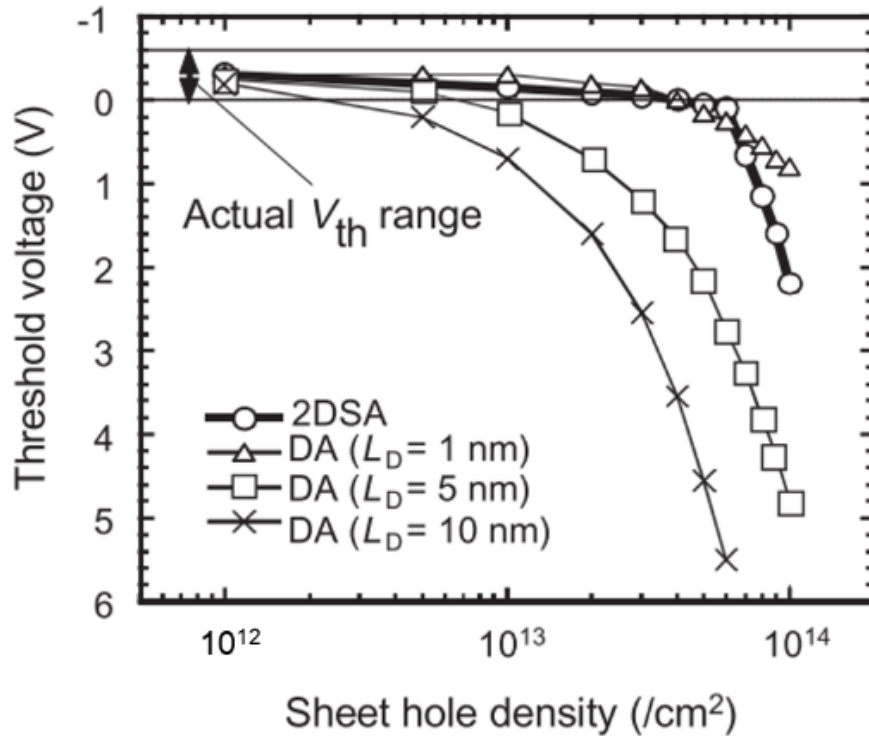


Figure 1.9 Comparison of simulated and actual dependence of V_T on sheet hole density in Pb-gate diamond MOSFET with surface p-type channel shown in Figure 1.8. The actual variation of V_T is indicated by the arrow sign.⁶⁵ Copyright (2001) The Japan Society of Applied Physics

Device simulation based on 2DSA and shallow depth acceptor (DA when $L_D = 1$ nm) distribution reproduced the actual DC characteristics of the hydrogen-terminated surface channel MESFET. The results suggested that the p-type surface conductivity is induced by the acceptors that are localized two-dimensionally or are near the surface. The mechanism of the surface conductivity of hydrogen-terminated diamond is still controversial. However, the quasi two-dimensional distribution is the only mode that can reproduce the operation of a MESFET with a hydrogen-terminated channel.

1.5 Performance of diamond electronic device

High-output operation diamond FETs are desirable because they are essential for the application of power devices. A diamond FET with a drain current over 1.3 A/mm has been achieved by the NO₂ adsorption treatment and Al₂O₃ passivation performed on the hydrogen-terminated diamond surface.⁴⁴ This characteristic indicates that Al₂O₃ is capable of stabilizing NO₂ adsorbates, which can increase the hole concentration.

Recently, transition metal oxides have garnered attention due to their capability to increase the performance of diamond devices. It has been reported that the hole carrier concentration of hydrogen-terminated diamond surfaces increased upon using MoO₃⁶⁸ or V₂O₅⁶⁹ as a surface electron acceptor material. Ren and coworkers have studied the operation of hydrogen-terminated diamond FETs with MoO₃ gate dielectric, showing a relatively high hole mobility, while transconductance of the FETs indicate good interface characteristics.⁷⁰ Drain current I_d over 12000 A/cm² has been realized in a hydrogen-terminated diamond MOSFET with a vertical-type channel.⁷¹

(110) diamond possesses the highest density of C-H dipoles, which induce more holes on the diamond surface. Diamond FETs fabricated on a (110) preferential oriented film have a higher I_{DS} and cut-off frequency (f_T) than those on the (100) surface.⁵⁷ In case of diamond MOSFETs with $f_T = 24$ GHz at $V_{DS} = -60$ V, fabricated on type II a (110) preferential surface, a maximum output power density of 3.8 W/mm was achieved.⁴⁶ Yu and coworkers demonstrated the high-frequency operation ($f_T = 66$ GHz; maximum oscillation frequency (f_{max}) = 55 GHz) of a (100) diamond MISFET with an output power density of 182 mW/mm by shortening the source-drain distance to 350 nm.⁷² Besides the RF operation, normally-off operation is also highly desirable as it offers the electronics

advantage of avoiding switching malfunctions in abnormal environments such as strong magnetic fields. The hydrogen-terminated diamond MOSFET shows a normally-off operation by partial C-O, which can suppress the formation of the 2DHG channel.^{49,73} Inversion channel diamond MOSFETs with normally-off characteristics have been successfully fabricated on n-type diamond body MOSFETs with p⁺ source/drain.²⁸ The normally-off operation can also be achieved by preventing hole accumulation by implanting a nitrogen-doped layer below the C-H channel.⁷⁴ The hole accumulation of the hydrogen-terminated diamond surface is compensated by the positive charges in high-K oxides such as HfO₂⁷⁵ or Y₂O₃⁷⁶, resulting in a normally-off operation.

The C-H bonded diamond is passivated by deposition of Al₂O₃ gate oxide, and stable operation was realized over a wide temperature range of 10 K to 673 K.⁴⁷

The breakdown voltage of 1.8 kV was achieved on a black polycrystalline C-H bonded diamond FET, suggesting that diamond is a worthy candidate with comparable high-voltage operation to lateral SiC and GaN FETs.⁴⁸ The average breakdown voltage of over 500 V realized on heteroepitaxial diamond FET⁷⁷ breaks the size limitation of homoepitaxially grown diamond substrates, leading to fully exploring its potential for application in high-performance electronics.

References

- ¹ F. Roccaforte, P. Fiorenza, G. Greco, R. L. Nigro, F. Giannazzo, F. Iucolano, and M. Saggio, *Microelectronic Engineering* **187**, 66 (2018).
- ² J. Millan, P. Godignon, X. Perpiñà, A. Pérez-Tomás, and J. Rebollo, *IEEE transactions on Power Electronics* **29**, 2155 (2013).
- ³ F. Roccaforte, P. Fiorenza, G. Greco, R. L. Nigro, F. Giannazzo, A. Patti, and M. Saggio, *Phys. Status Solidi A* **211**, 2063 (2014).
- ⁴ M. W. Geis, T. C. Wade, C. H. Wuorio, T. H. Fedynyshyn, B. Duncan, M. E. Plaut, J. O. Varghese, S. M. Warnock, S. A. Vitale, and M. A. Hollis, *Phys. Status Solidi A* **215**, 1800681 (2018).
- ⁵ S. B. Shirey and J. E. Shigley, *Gems & Gemology* **49** (2013).
- ⁶ F. Bundy, H. T. Hall, H. Strong, and R. Wentorf, *nature* **176**, 51 (1955).
- ⁷ B. Spitsyn, L. Bouilov, and B. Derjaguin, *Journal of Crystal Growth* **52**, 219 (1981).
- ⁸ P. W. May, *Philosophical Transactions of the Royal Society of London. Series A: Mathematical, Physical and Engineering Sciences* **358**, 473 (2000).
- ⁹ R. Haubner and B. Lux, *Diam. Relat. Mater.* **2**, 1277 (1993).
- ¹⁰ S. Okoli, R. Haubner, and B. Lux, *Surface and Coatings technology* **47**, 585 (1991).
- ¹¹ F. Celi, P. Pehrsson, H. T. Wang, and J. Butler, *Appl. Phys. Lett.* **52**, 2043 (1988).
- ¹² F. Celi and J. Butler, *Annual Review of Physical Chemistry* **42**, 643 (1991).
- ¹³ S. Redman, K. Rosser, and M. R. Ashfold, *Physical Chemistry Chemical Physics* **1**, 1415 (1999).
- ¹⁴ J. Smith, E. Cameron, M. Ashfold, Y. A. Mankelevich, and N. Suetin, *Diam. Relat. Mater.* **10**, 358 (2001).

- ¹⁵ P. John, J. Rabeau, and J. Wilson, *Diam. Relat. Mater.* **11**, 608 (2002).
- ¹⁶ J. C. Angus, A. Argoitia, R. Gat, Z. Li, M. Sunkara, L. Wang, and Y. Wang, *Philosophical Transactions of the Royal Society of London. Series A: Physical and Engineering Sciences* **342**, 195 (1993).
- ¹⁷ J. E. Butler and R. L. Woodin, *Philosophical Transactions of the Royal Society of London. Series A: Physical and Engineering Sciences* **342**, 209 (1993).
- ¹⁸ D. Goodwin and J. Butler, *Handbook of industrial diamonds and diamond films*, 527 (1997).
- ¹⁹ H. Kawarada, H. Sasaki, and A. Sato, *Physical Review B* **52**, 11351 (1995).
- ²⁰ J. Furthmüller, J. Hafner, and G. Kresse, *Physical Review B* **53**, 7334 (1996).
- ²¹ R. S. Sussmann, *CVD diamond for electronic devices and sensors*. (John Wiley & Sons, 2009).
- ²² B. J. Garrison, E. J. Dawnkaski, D. Srivastava, and D. W. Brenner, *Science* **255**, 835 (1992).
- ²³ J. K. Kang and C. B. Musgrave, *J. Chem. Phys.* **113**, 7582 (2000).
- ²⁴ B. Fox, M. Hartsell, D. Malta, H. Wynands, C.-T. Kao, L. Plano, G. Tessmer, R. Henard, J. Holmes, and A. Tessmer, *Diam. Relat. Mater.* **4**, 622 (1995).
- ²⁵ S. Sonoda, J. Won, H. Yagi, A. Hatta, T. Ito, and A. Hiraki, *Appl. Phys. Lett.* **70**, 2574 (1997).
- ²⁶ H. Kiyota, E. Matsushima, K. Sato, H. Okushi, T. Ando, J. Tanaka, M. Kamo, and Y. Sato, *Diam. Relat. Mater.* **6**, 1753 (1997).
- ²⁷ E. Ekimov, V. Sidorov, E. Bauer, N. Mel'Nik, N. Curro, J. Thompson, and S. Stishov, *nature* **428**, 542 (2004).

- ²⁸ T. Matsumoto, H. Kato, K. Oyama, T. Makino, M. Ogura, D. Takeuchi, T. Inokuma, N. Tokuda, and S. Yamasaki, *Sci. Rep.* **6**, 31585 (2016).
- ²⁹ H. Kawashima, S. Ohmagari, H. Umezawa, and D. Takeuchi, *Jpn. J. Appl. Phys.* **58** (2019).
- ³⁰ H. Okazaki, T. Wakita, T. Muro, T. Nakamura, Y. Muraoka, T. Yokoya, S.-i. Kurihara, H. Kawarada, T. Oguchi, and Y. Takano, *Appl. Phys. Lett.* **106**, 052601 (2015).
- ³¹ T. Teraji, S. Koizumi, and H. Kanda, *Phys. Status Solidi A* **181**, 129 (2000).
- ³² M. Geis, D. Rathman, D. Ehrlich, R. Murphy, and W. Lindley, *IEEE Electron Device Lett.* **8**, 341 (1987).
- ³³ C. R. Zeisse, C. A. Hewett, R. Nguyen, J. R. Zeidler, and R. G. Wilson, *IEEE Electron Device Lett.* **12**, 602 (1991).
- ³⁴ G. S. Gildenblat, S. Grot, C. Hatfield, and A. Badzian, *IEEE Electron Device Lett.* **12**, 37 (1991).
- ³⁵ M. Landstrass and K. V. Ravi, *Appl. Phys. Lett.* **55**, 975 (1989).
- ³⁶ H. Kawarada, M. Aoki, and M. Ito, *Appl. Phys. Lett.* **65**, 1563 (1994).
- ³⁷ K. Hayashi, S. Yamanaka, H. Okushi, and K. Kajimura, *Appl. Phys. Lett.* **68**, 376 (1996).
- ³⁸ K. Tsugawa, K. Kitatani, H. Noda, A. Hokazono, K. Hirose, M. Tajima, and H. Kawarada, *Diam. Relat. Mater.* **8**, 927 (1999).
- ³⁹ H. Kawarada, M. Aoki, H. Sasaki, and K. Tsugawa, *Diam. Relat. Mater.* **3**, 961 (1994).
- ⁴⁰ Y. Yun, T. Maki, and T. Kobayashi, *J. Appl. Phys.* **82**, 3422 (1997).
- ⁴¹ H. Kawarada, *Jpn. J. Appl. Phys.* **51**, 090111 (2012).
- ⁴² H. Kawarada, T. Yamada, D. Xu, H. Tsuboi, Y. Kitabayashi, D. Matsumura, M. Shibata, T. Kudo, M. Inaba, and A. Hiraiwa, *Sci. Rep.* **7**, 42368 (2017).

- ⁴³ Y. Fu, R. Xu, Y. Xu, J. Zhou, Q. Wu, Y. Kong, Y. Zhang, T. Chen, and B. Yan, *IEEE Electron Device Lett.* **39**, 1704 (2018).
- ⁴⁴ K. Hirama, H. Sato, Y. Harada, H. Yamamoto, and M. Kasu, *Jpn. J. Appl. Phys.* **51**, 090112 (2012).
- ⁴⁵ X. Yu, J. Zhou, C. Qi, Z. Cao, Y. Kong, and T. Chen, *IEEE Electron Device Lett.* **39**, 1373 (2018).
- ⁴⁶ S. Imanishi, K. Horikawa, N. Oi, S. Okubo, T. Kageura, A. Hiraiwa, and H. Kawarada, *IEEE Electron Device Lett.* **40**, 279 (2019).
- ⁴⁷ H. Kawarada, T. Yamada, D. Xu, H. Tsuboi, T. Saito, and A. Hiraiwa, presented at the 2014 IEEE International Electron Devices Meeting, (2014).
- ⁴⁸ M. Syamsul, Y. Kitabayashi, D. Matsumura, T. Saito, Y. Shintani, and H. Kawarada, *Appl. Phys. Lett.* **109** (2016).
- ⁴⁹ Y. Kitabayashi, T. Kudo, H. Tsuboi, T. Yamada, D. Xu, M. Shibata, D. Matsumura, Y. Hayashi, M. Syamsul, M. Inaba, A. Hiraiwa, and H. Kawarada, *IEEE Electron Device Lett.* **38**, 363 (2017).
- ⁵⁰ J. Shirafuji and T. Sugino, *Diam. Relat. Mater.* **5**, 706 (1996).
- ⁵¹ M. Tachiki, H. Seo, T. Banno, Y. Sumikawa, H. Umezawa, and H. Kawarada, *Appl. Phys. Lett.* **81**, 2854 (2002).
- ⁵² A. Hiraiwa, A. Daicho, S. Kurihara, Y. Yokoyama, and H. Kawarada, *J. Appl. Phys.* **112**, 124504 (2012).
- ⁵³ H. Kawarada, H. Tsuboi, T. Naruo, T. Yamada, D. Xu, A. Daicho, T. Saito, and A. Hiraiwa, *Appl. Phys. Lett.* **105**, 013510 (2014).

- ⁵⁴ T. Maki, S. Shikama, M. Komori, Y. Sakaguchi, K. Sakuta, and T. Kobayashi, *Jpn. J. Appl. Phys.* **31**, L1446 (1992).
- ⁵⁵ M. Itoh and H. Kawarada, *Jpn. J. Appl. Phys.* **34**, 4677 (1995).
- ⁵⁶ D. Takeuchi, M. Riedel, J. Ristein, and L. Ley, *Physical Review B* **68**, 041304 (2003).
- ⁵⁷ K. Hirama, H. Takayanagi, S. Yamauchi, J. Yang, H. Kawarada, and H. Umezawa, *Appl. Phys. Lett.* **92**, 112107 (2008).
- ⁵⁸ F. Maier, M. Riedel, B. Mantel, J. Ristein, and L. Ley, *Phys. Rev. Lett.* **85**, 3472 (2000).
- ⁵⁹ R. S. Gi, T. Mizumasa, Y. Akiba, Y. Hirose, T. Kurosu, and M. Iida, *Jpn. J. Appl. Phys.* **34**, 5550 (1995).
- ⁶⁰ P. Strobel, M. Riedel, J. Ristein, and L. Ley, *Nature* **430**, 439 (2004).
- ⁶¹ M. T. Edmonds, M. Wanke, A. Tadich, H. M. Vulling, K. J. Rietwyk, P. L. Sharp, C. B. Stark, Y. Smets, A. Schenk, Q. H. Wu, L. Ley, and C. I. Pakes, *J. Chem. Phys.* **136**, 124701 (2012).
- ⁶² M. J. Sear, A. K. Schenk, A. Tadich, A. Stacey, and C. I. Pakes, *Appl. Phys. Lett.* **110**, 011605 (2017).
- ⁶³ K. G. Crawford, D. Qi, J. McGlynn, T. G. Ivanov, P. B. Shah, J. Weil, A. Tallaire, A. Y. Ganin, and D. A. J. Moran, *Sci. Rep.* **8**, 3342 (2018).
- ⁶⁴ C. E. Nebel, F. Ertl, C. Sauerer, M. Stutzmann, C. Graeff, P. Bergonzo, O. A. Williams, and R. Jackman, *Diam. Relat. Mater.* **11**, 351 (2002).
- ⁶⁵ K. Tsugawa, H. Umezawa, and H. Kawarada, *Jpn. J. Appl. Phys.* **40**, 3101 (2001).
- ⁶⁶ M. Aoki and H. Kawarada, *Jpn. J. Appl. Phys.* **33**, L708 (1994).
- ⁶⁷ H. Kawarada, M. Itoh, and A. Hokazono, *Jpn. J. Appl. Phys.* **35**, L1165 (1996).

- ⁶⁸ S. A. Russell, L. Cao, D. Qi, A. Tallaire, K. G. Crawford, A. T. Wee, and D. A. Moran, *Appl. Phys. Lett.* **103**, 202112 (2013).
- ⁶⁹ K. G. Crawford, L. Cao, D. Qi, A. Tallaire, E. Limiti, C. Verona, A. T. Wee, and D. A. Moran, *Appl. Phys. Lett.* **108**, 042103 (2016).
- ⁷⁰ Z. Ren, J. Zhang, J. Zhang, C. Zhang, S. Xu, Y. Li, and Y. Hao, *IEEE Electron Device Lett.* **38**, 786 (2017).
- ⁷¹ M. Iwataki, N. Oi, K. Horikawa, S. Amano, J. Nishimura, T. Kageura, M. Inaba, A. Hiraiwa, and H. Kwarada, *IEEE Electron Device Lett.* **41**, 111 (2019).
- ⁷² X. Yu, J. Zhou, S. Zhang, Z. Cao, Y. Kong, and T. Chen, *Appl. Phys. Lett.* **115**, 192102 (2019).
- ⁷³ J.-F. Zhang, W.-J. Chen, Z.-Y. Ren, K. Su, P.-Z. Yang, Z.-Z. Hu, J.-C. Zhang, and Y. Hao, *Phys. Status Solidi A* **217**, 1900462 (2020).
- ⁷⁴ N. Oi, T. Kudo, M. Inaba, S. Okubo, S. Onoda, A. Hiraiwa, and H. Kwarada, *IEEE Electron Device Lett.* **40**, 933 (2019).
- ⁷⁵ J. Liu, M. Liao, M. Imura, and Y. Koide, *Appl. Phys. Lett.* **103**, 092905 (2013).
- ⁷⁶ J. Liu, H. Oosato, M. Liao, and Y. Koide, *Appl. Phys. Lett.* **110**, 203502 (2017).
- ⁷⁷ M. Syamsul, N. Oi, S. Okubo, T. Kageura, and H. Kwarada, *IEEE Electron Device Lett.* **39**, 51 (2017).

Chapter II selective growth of high-quality single crystal diamond by point-arc remote MPCVD utilizing SiO₂ mask

2.1 Selective growth of diamond

Diamond substrates as a potential alternative of power device material has been applied to various electronics with different architectures such as MOSFET¹, MESFET², junction FET³ and Schottky barrier diode⁴.

Diamond selective growth techniques are believed to be the most effective approaches to fabricate the functional architecture in the electronics above. Because impurity dope by ion implantation will introduce unrecoverable damage that transfer sp³ to energetically favorable sp².⁵ Successful selective growth of heavily phosphorus-doped (n⁺) (111) diamond on (001), the selectively grown (111) diamond film showed four orders of magnitude lower than that of (001) diamond.⁶ heavily phosphorus-doped (phosphorus concentration $\sim 1 \times 10^{19} \text{ cm}^{-3}$) diamond were selectively grown by MPCVD with Ti/Au mask covered. Ohmic contact formation using the heavily phosphorus-doped diamond is a promising method to obtain n-type diamond suitable for electronic devices,⁷ the fabrication process is illustrated in **Figure 2.1**. Moreover, As shown in **Figure 2.2**, diamond metal-semiconductor FET (MESFET) was realized on selectively grown p⁺ contact layer,

resulting drain current improved from 0.06 to 0.2 mA/mm.⁸ It is important to note that simultaneously achieving C-Si diamond surface and low on-resistance, selective growth is considered to be a simple and effective method for C-Si diamond FET fabrication. The detail of C-Si diamond FET will be discussed in Chapter III. In this chapter will focus on the feasibility of selective growth utilizing the arc-point remote MPCVD with SiO₂ mask assisting.

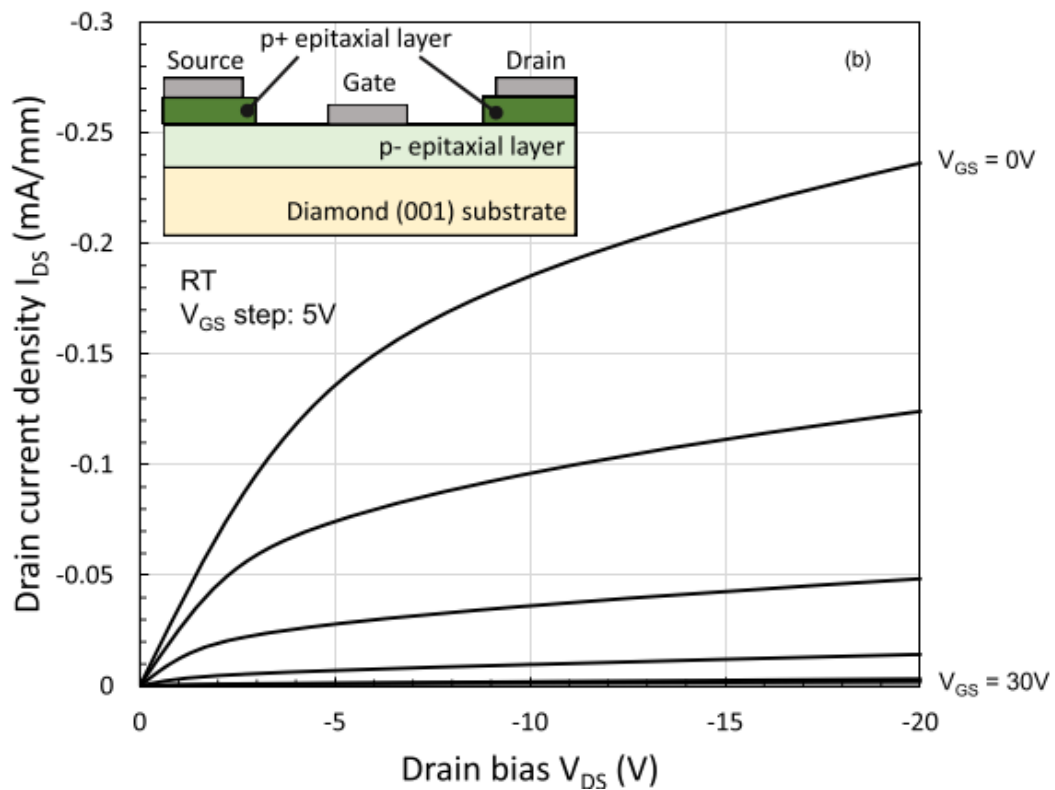


Figure 2.2 Drain current (I_{DS}) – drain bias (V_{DS}) characteristics of the diamond MESFET with p^+ contact layer. The inset is cross-sectional structure of the MESFET. The p^+ epitaxial layer is selectively grown by HFCVD and considerably decrease the resistivity of between diamond and metal contact.⁸ Copyright (2019) The Japan Society of Applied Physics

2.2 point-arc remote plasma MPCVD

Polycrystalline diamond consists of several crystal grains and shows poor performance in electronic devices comparing to those based on single crystal diamond.⁹ Therefore, selective homoepitaxial growth of single diamond is commonly performed to structure the architecture of each functional component in electronic devices.¹⁰⁻¹³ MPCVD and hot filament CVD (HFCVD) have been intensively investigated as deposition methods for homoepitaxial diamond growth. Although research on HFCVD were initiated earlier and were widely accepted, the contaminant is still a severe problem.

The typical process for diamond growth is a competition between the etching effect caused by atomic hydrogen and the deposition of carbon precursors. Because it is still controversial whether the carbon precursor methyl or/and acetylene, hereafter C_xH_y will be referred to as the precursors. Carbon-containing gas and hydrogen gas mixed at an appropriate ratio are usually used as reactant gases, and they are stimulated to atomic or ionic radicals thermally, chemically, electrically, or electromagnetically. C_xH_y diffuse to the surface and are absorbed by the substrate, and then hydrogen abstracted from the radical forms a dangling bond for the subsequent C_xH_y radicals, this reaction occurs mainly during the deposition process. However, growing diamond crystals are continuously etched by atomic hydrogen, and if the deposition rate is higher than the etching rate, the diamond deposition dominates the CVD process.¹⁴⁻¹⁶

In HFCVD diamond growth processes, filament temperatures of 2000°C or higher are favored, and the carburization or evaporation of metallic filaments and the dissociation of reactant gases occur simultaneously.^{17,18} Subsequently, evaporated filament materials are involved in the deposition of carbon precursors, leading to diamond contamination. In

numerous studies, Ta, W, and Re have been utilized as filaments in diamond deposition by HFCVD, and the contaminant concentrations were reported to be significant in all three materials.¹⁹⁻²³ Despite the high toleration of contaminants in some fields, this disadvantage limits the applicability of HFCVD because the electronic properties of diamond are very sensitive to contaminants. The presence of contaminants can deteriorate the carrier concentration, and mobility values may consequently degrade diamond quality, and thus deteriorate device performance.

At present, conventional MPCVD is the dominant method for producing high-quality homoepitaxial growth.^{11,24} In conventional MPCVD, the operating temperature is usually below 1000 °C, far below the evaporation temperature of the metal antenna, resulting in far fewer impurities in diamond deposited by MPCVD than that deposited by HFCVD. However, diamond deposition by MPCVD has also shown new problems with increasing studies on this method. In order to maintain an appropriate substrate temperature for diamond growth, an additional heating system is usually utilized, and when the microwave plasma changes, the substrate temperature is also modified because the plasma flame causes an undesirable heat load. Furthermore, the masks are usually found to peel off or burst after MPCVD growth, and this phenomenon indicates an abnormal temperature increase that causes an ion bombardment effect in the plasma.^{12,25} In addition, because the plasma is ignited near the substrate, the concentration of radicals on the substrate is extremely high. The competition of deposition and etching is so fierce that even slight variations in the experimental parameters lead to low reproducibility.²⁶

Point-arc remote MPCVD has to date only been reported to be effective for the successful synthesis of carbon nanotubes.²⁶⁻³⁰ Diamond deposition by remote plasma on a silicon wafer has been also reported, and the results confirmed the presence of a diamond precursor outside the plasma's luminous sphere; however, the quality and contamination of crystalline diamond were not comprehensively understood.³¹ The activation energy supply of point-arc remote MPCVD is the same as conventional MPCVD, generally 2.45-GHz microwave supplied by a magnetron generator carried by a waveguide to the reaction chamber through the convertor. As shown in **Figure 2.3**, without discharging electrode pair inside the chamber, the plasma ball ignites only at the edge of the antenna will not be drifted to the cathode by electric field, and the plasma maintains a ball shape that will not change as input power changes. Moreover, the maximum radius of the plasma ball will not exceed a quarter of the wavelength of the generator.³² The vacuum flanges are sealed by the copper gaskets and fluororubber O-rings; therefore, the water-cooling system is induced into the antenna to avoid the O-ring failure caused by antenna over-heating. The reaction chamber is made of stainless steel with an inner diameter far larger than the diameter of the plasma ball to avoid plasma contact. Unlike conventional MPCVD, which normally proceeds with the substrate close to the plasma, the point-arc remote plasma is immobilized and will not move to the substrate side because the position of the antenna edge corresponds to the antinode ($1/4 \lambda$) of the standing microwave from the wave window, The wave is at maximum amplitude at the antinode, constantly. The distance between the substrate and antenna can be adjusted, and the substrate temperature can be monitored with non-contact measurements by a pyrometer. The maximum output power of the generator is 300 W, when the output power increases to more than 200 W,

the risk of plasma distortion moving towards the generator side increases significantly. To ensure the stable operation of the plasma in 4 hours growth duration, the output power of all growth experiments was under 200 W.

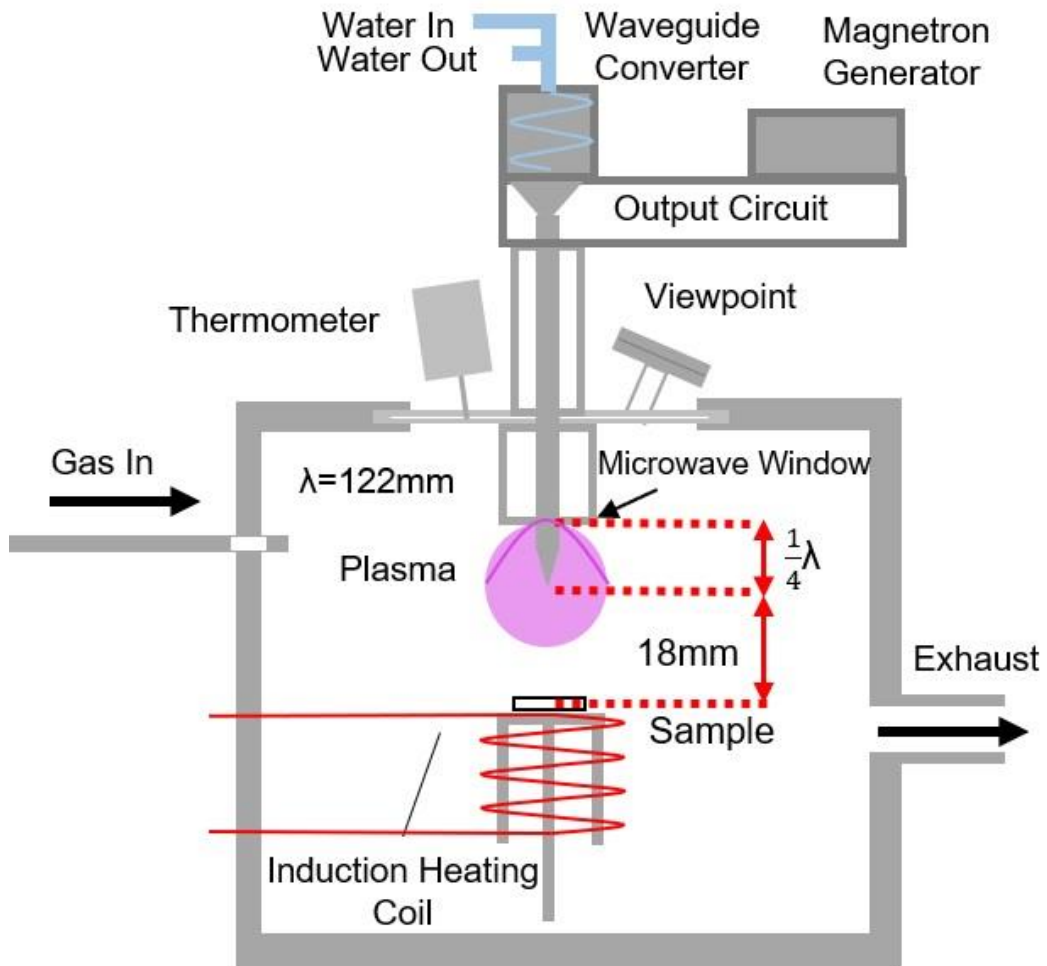


Figure 2.3 Schematic of point-arc remote MPCVD. 2.45-GHz microwave and reactant gas were guided to the top of the reaction chamber to ignite the plasma. The plasma ball is fixed at the antenna tip and does not move the substrate, and the distance between the plasma and substrate is adjustable. Substrate temperatures were measured by thermometer. The sample stage is surrounded by the separate induction heating coil.

In this work, the selective growth of the high-quality single crystalline diamond was successfully conducted by the point-arc remote MPCVD as shown in **Figure 2.3**. The crystalline quality of the selectively grown diamond was comprehensively evaluated. The SIMS profile suggested that the selectively grown diamond was high-quality single diamond without contaminants from the metal antenna. The distribution of some contaminants at the substrate and interface surfaces was independent of the substrate temperatures, which were within the MPCVD operating range. Although the mechanism of impurity incorporation remained indistinct, the limited distribution of contaminants and moderate growth rate of 50 nm h^{-1} enable high reproducibility, which is of great importance for precise control thickness of selective growth layer.

2.3 Experimental methods

2.3.1 Growth condition of diamond growth on Si

Diamond growth by remote type MPCVD have not reported before this work, it is necessary to optimize the growth conditions for diamond growth. Two parameters were considered for experimental condition optimization: growth rate and orientation of crystal surface. Excessively high growth rates will reduce the reproducibility, whereas very slow growth rates require long experimental periods, and grains with the same facets are more favorable than those with random facets. The experimental condition optimization was conducted on silicon substrates at various substrate temperatures, chamber pressures, and methane concentration. Diamond nanopowders (AR BROWN Co., Ltd, Japan) with average diameters of 4~6 nm were dispersed on silicon wafers by ultrasonic treatment in

deionized water. Typical deposition conditions were: substrate temperatures of 650~850°C, chamber pressures of 20~30 Torr, and methane concentrations of 0.5~2.0%; microwave power applied to the antenna was 100 W, based on previous reports^{9,11,24,33}.

The dependence of the growth rate on substrate temperature is shown in **Figure 2.4**, in which the SEM images suggest that diamond nuclei had been grown on the silicon substrate, indicating that there were carbon precursors for diamond growth even outside the plasma's luminous region. As can be seen from the figure, the growth rate was proportional to the substrate temperature. Under same scale bar, the grain obtained under 650°C is without clear diamond facet and barely able to be observed. On the contrast, even the largest grains were obtained under 850°C, they were polycrystalline zed composed of various facets.

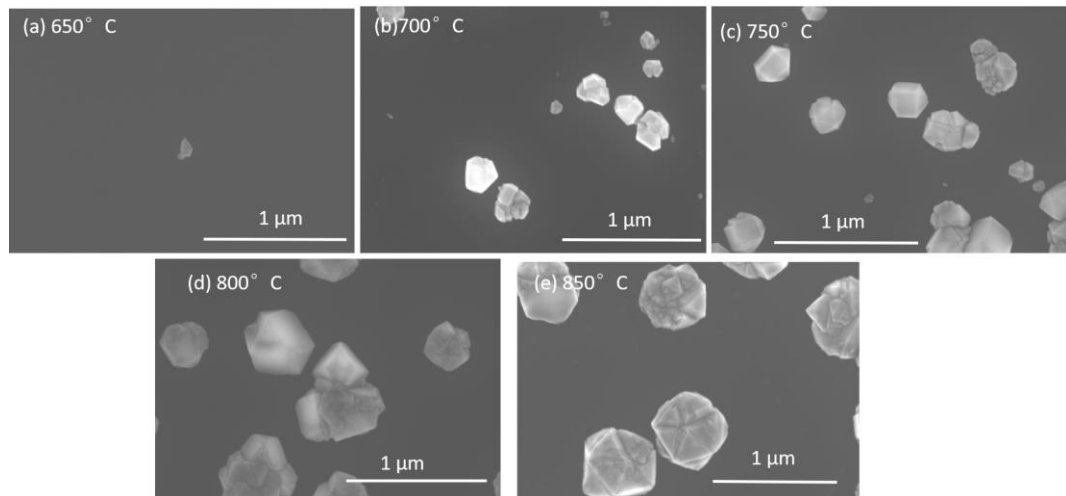


Figure 2.4 SEM images of grains obtained with methane concentrations of (a) 650°C, (b) 700°C, (c) 750°C, (d) 800°C and (e) 850°C.

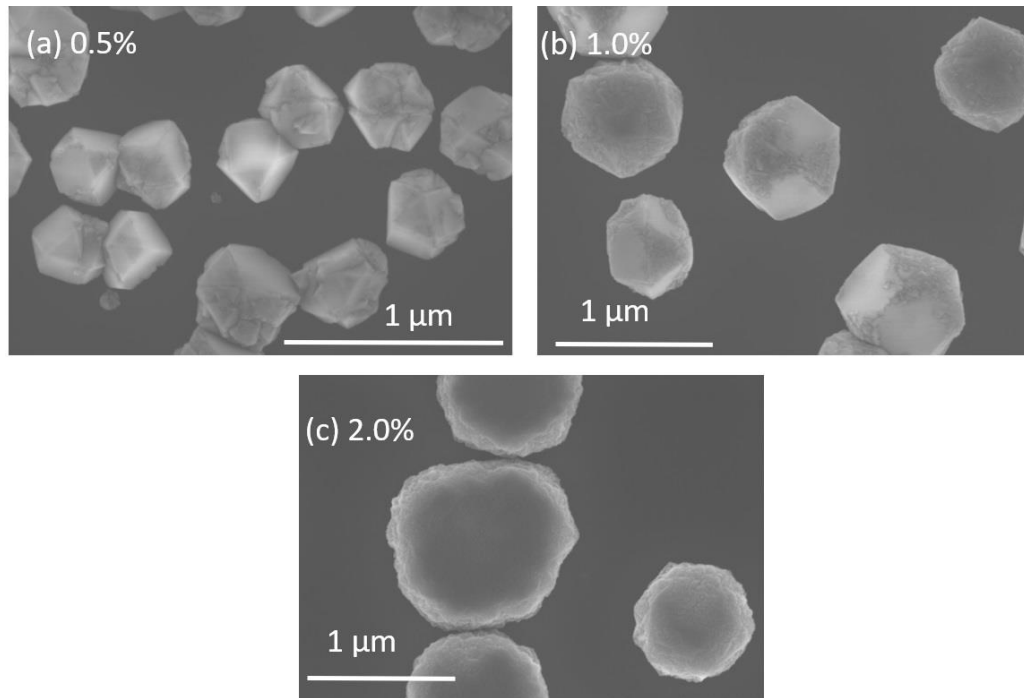


Figure 2.5 SEM images of grains obtained with methane concentrations of (a) 0.5%, (b) 1%, and (c) 2%.

Figure 2.5 show the SEM images of diamond obtained in different methane concentration varies from 0.5%~ 2.0% Torr indicated the growth is highly sensitive of methane concentration. The disorientation of grains increases with increasing methane concentration, and when the methane concentration was higher than 0.5%, the polycrystalline diamond dominated. The morphology of grains obtained at 2.0% differs sharply with that obtained at 0.5%, even the size of grain increase as the methane increase, indicating the growth rate is proportional to the methane concentration.

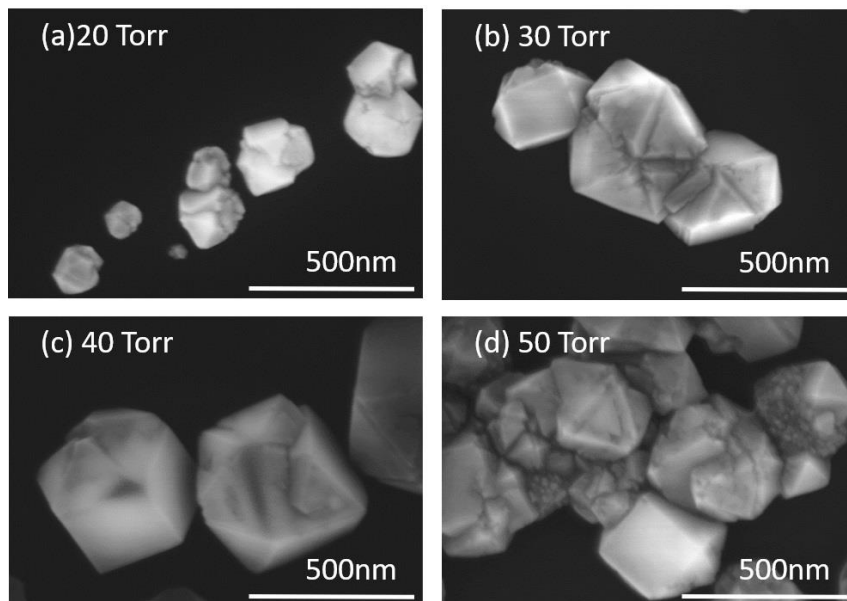


Figure 2.6 SEM images of grains obtained under (a) 20 Torr, (b) 30 Torr, (c) 40 Torr, and (d) 50 Torr.

Figure 2.6 show the SEM images of diamond obtained in different chamber pressure varies from 20~50 Torr. Grains obtained all chamber pressures show polycrystalline, the largest size grains were grown under 40 Torr.

Taking growth rate and crystal orientation to accounting, the key parameters of selective growth by point-arc remote MPCVD were determined based on the results above, substrate temperature of 800°C , chamber pressure 40 Torr and methane concentration of 0.5%.

2.3.2 Diamond substrate preparation

In order to get an uncontaminated surface without non-diamond carbon for subsequent process, strong acid boiling using mixture solution of H₂SO₄ and HNO₃ at 240 °C for 30 minutes was conducted to the type Ib HPHT grown (001) substrate with sizes of 3 × 3 × 0.5 mm³ to remove the graphitic contaminants. The ultrasonically treatment involved 10-minute soak in deionized water, ethanol, acetone, ethanol deionized water for was performed to remove the organic contaminants, then the substrate was blow dry by pure nitrogen gas (N₂).

Table 2.1 the experimental parameter for the undoped homoepitaxy diamond layer

Parameters	Values
Stage material	Mo
Stage temperature	450 °C
Substrate temperature	600°C
Stage height	45.0
Chamber pressure	35.0 Torr
Microwave power	750 W
H ₂ flow rate	394 sccm
CH ₄ flow rate	3.0 sccm
CO ₂ flow rate	3.0 sccm (Set value: 4.0 sccm)
Growth rate	170 nm/h
Diamond film thickness	500 nm

A 2- μm diamond undoped homoepitaxy layer was deposited on the surface by conventional MPCVD process (ASTeX- AX2115) which is favorable for following etching process. There are two set of experimental parameters with different growth rate in the diamond homoepitaxy by ASTeX- AX2115 apparatus. Because the epitaxial layer is thick, the process parameters of high growth rate were adopted. The parameters are provided in **Table 2.1**. The flow rate of CO_2 is controlled by a mass flow controller designed for N_2 , so it is necessary to use the gas correction factor to convert the flow rate. To clean the non-diamond component generated during MPCVD process, the strong acid boiling process was conducted once again. Prior to the subsequent SiO_2 deposition, the diamond substrate was oxygen-terminated by UV ozone treatment.

2.3.3 Deposition and patterning SiO_2 mask

A 260-nm SiO_2 layer (measured by optical interference thickness meter) was then deposited by plasma CVD using tetraethyl orthosilicate (TEOS) as the deposition source, and this mask was utilized in subsequent selective growth. The experimental parameters of plasma CVD (TEOS) can be seen in **Table 2.2**. The mask was patterned with electrodes shaped at the micrometer order by laser lithography. SiO_2 patterning was completed by dry etching using C_3F_8 in an inductive coupled plasma-ion reactive etching (ICP-RIE) and lift-off process.

Table 2.2 Experimental parameters for SiO₂ deposition by plasma CVD (TEOS) (SAMCO PD-220)

O ₂	500 sccm
TEOS	4 sccm
Substrate temperature	300°C
RF power	80 W
Process time	8 min

2.3.4 Selective growth of diamond

Next, as shown in **Figure 2.7** (a) diamond was selectively grown by point-arc remote MPCVD in locations without SiO₂ masks. The reactant gas mixed with hydrogen and methane, nitrogen impurities in the reactant gases is up to 0.05ppm and 5ppm, respectively. The experimental parameters for selective growth can be seen in **Table 2.3**, the methane/hydrogen ratio, chamber pressure, and microwave power were 0.5%, 40 Torr, and 100 W, respectively. The total growth duration was 4 hours. The substrate temperature was 800°C measured by infrared thermometer. The estimated growth rate of is approximately 80 nm h⁻¹. Finally, patterned diamond film was developed after adding hydrofluoric acid (20 mL) solution to remove the SiO₂ masks at room temperature for 1 hour. (**Figure 2.7** (b)). As shown in **Figure 2.7** (c), three homoepitaxy layers were successively deposited on sample B, and the substrate temperatures of the layers from bottom to top were 750, 800, and 850 °C, respectively. The deposition time of each layer was 3 hours, and the other conditions were the same as those for sample A. SIMS analysis of sample B was conducted to investigate contaminant concentration from the discharging antenna during point-arc remote MPCVD growth at various temperatures.

All fabrication processes are summarized in **Table 2.4**, more details are provided in Appendix A.

Table 2.3 the experimental parameter for the selective growth by point-arc remote MPCVD

Parameters	Values
Stage material	Mo
Substrate temperature	800°C
Distance from antenna to substrate	18 mm
Chamber pressure	40Torr
Microwave power	100 W
H ₂ flow rate	200 sccm
CH ₄ flow rate	1 sccm
Growth rate	80 nm/h
Thickness of film	330 nm

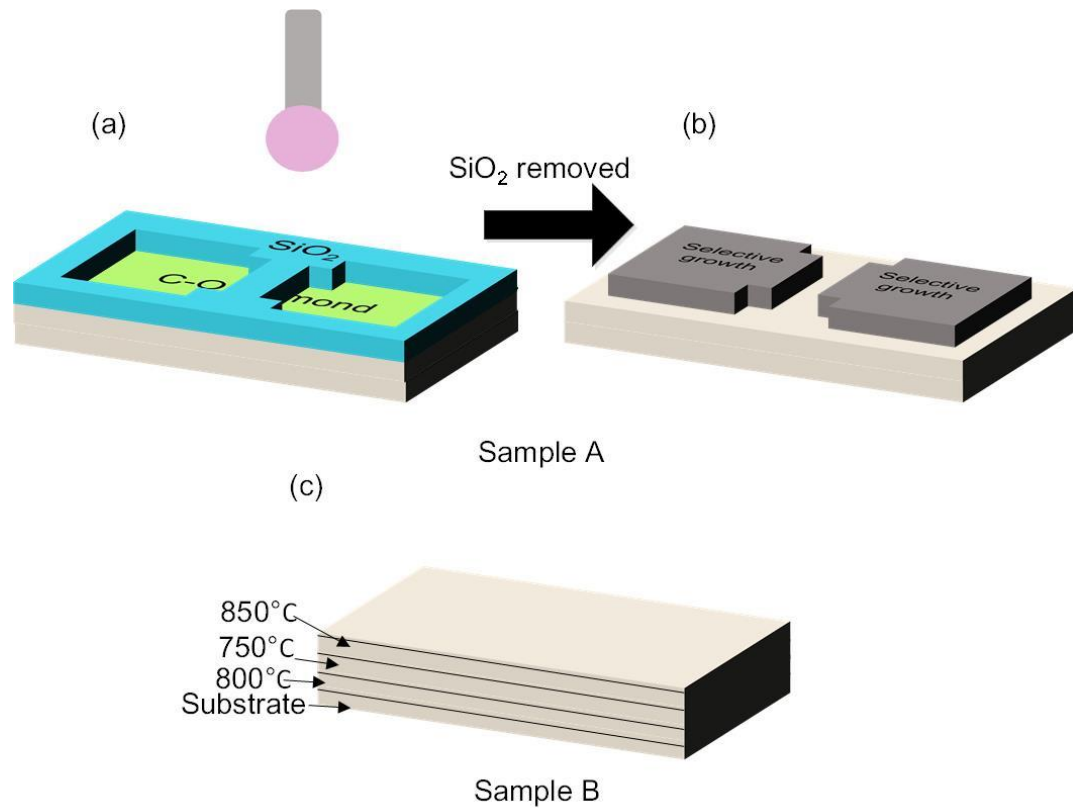
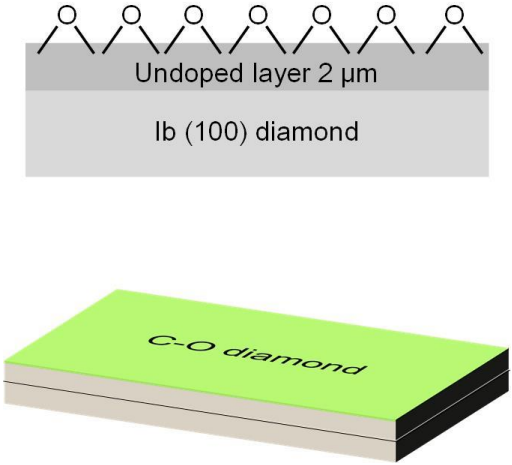
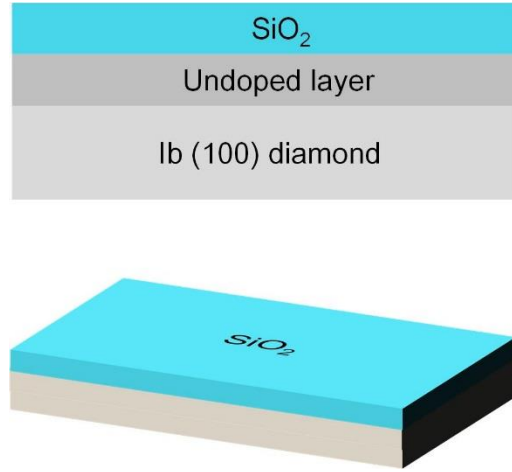
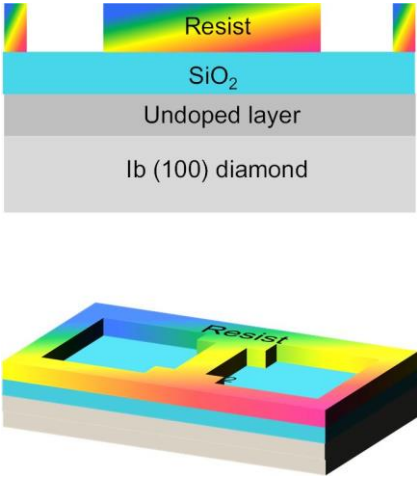
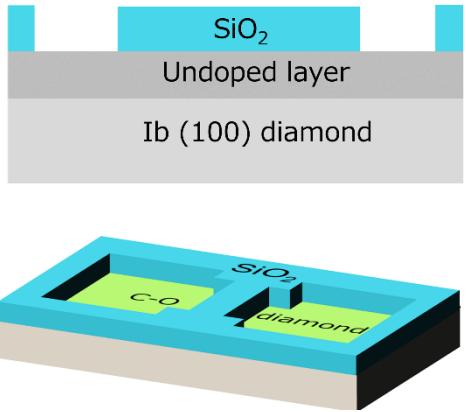
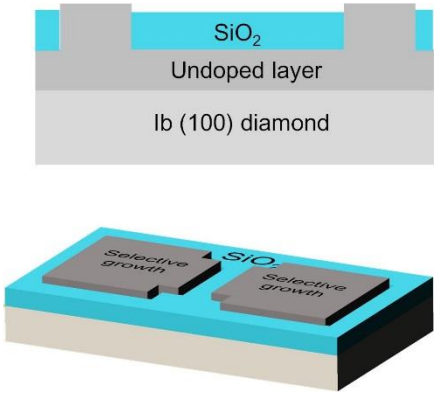
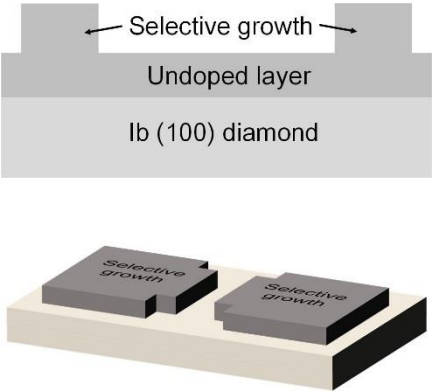


Figure 2.7 (a) Before selective growth, a 260-nm SiO₂ layer was deposited on sample A by plasma CVD, and then the mask architecture was established by laser lithography and ICP-RIE, sequentially. The distance from the plasma ball to the substrate was 18 mm, and the plasma ball was fixed, having no contact with the substrate. (b) After 4 hours of selective growth, the masks on sample A were removed chemically. A pair of symmetric electrode patterns was successfully obtained by selective growth, and the dimension of each selectively grown region was approximately $75 \times 60 \mu\text{m}^2$. (c) Three homoepitaxy layers were deposited successively on sample B by point-arc remote MPCVD at 850, 750, and 800 °C.

Table 2.4 Experimental process

 <p>Undoped layer 2 μm Ib (100) diamond</p> <p><i>C-O diamond</i></p>	<p>1. substrate preparation</p>	<p>Substrate: HPHT type Ib (001)</p> <ol style="list-style-type: none"> 1. Strong acid boiling 2. substrate cleaning 3. homoepitaxial undoped layer (2 μm, CVD 3) 4. Strong acid boiling 5. chemical cleaning 6. oxygen-termination UV ozone for 3h
 <p>SiO_2 Undoped layer Ib (100) diamond</p> <p><i>SiO₂</i></p>	<p>2. SiO_2 deposition</p>	<p>deposition: 260 nm SiO_2 by TEOS CVD: 300$^\circ\text{C}$, 8 min,</p>

 <p>The top diagram is a cross-section showing a stack of layers: a grey 'Ib (100) diamond' layer at the bottom, a grey 'Undoped layer' above it, a light blue 'SiO₂' layer, and a multi-colored 'Resist' layer on top. The 3D view below shows a rectangular substrate with a central rectangular opening. The top surface is covered with a multi-colored 'Resist' layer, and the bottom surface is the grey 'Ib (100) diamond' layer.</p>	<p>3. UV lithography</p>	<p>UV lithography</p> <ol style="list-style-type: none"> 1. Double layer resist spin: 2. Lithography 3. Development
 <p>The top diagram is a cross-section showing a stack of layers: a grey 'Ib (100) diamond' layer at the bottom, a grey 'Undoped layer' above it, and a light blue 'SiO₂' layer on top. The 3D view below shows a rectangular substrate with a central rectangular opening. The top surface is covered with a light blue 'SiO₂' layer, and the bottom surface is the grey 'Ib (100) diamond' layer. The opening is filled with a yellow 'C-O' layer.</p>	<p>4. Selective etching of SiO₂</p>	<ol style="list-style-type: none"> 1. ICP-RIE by C₃F₈: 2 min 2. double-layer resist remove

 <p>The top diagram is a cross-section showing a light blue SiO_2 layer on top of a grey undoped layer, which is on a grey Ib (100) diamond substrate. The bottom diagram is a 3D perspective view of the same structure, with two rectangular regions on the SiO_2 layer labeled "Selective growth".</p>	<p>5. Selective growth</p>	<p>UV lithography</p> <ol style="list-style-type: none"> 1. Double layer resist: 2. Lithography 3. Development
 <p>The top diagram is a cross-section showing a grey undoped layer on top of a grey Ib (100) diamond substrate. Two rectangular regions on the undoped layer are labeled "Selective growth" with arrows pointing to them. The bottom diagram is a 3D perspective view of the same structure, with two rectangular regions on the undoped layer labeled "Selective growth".</p>	<p>6. SiO_2 removed</p>	<p>Double-layer Resists remove: THF (30 min ~ overnight)</p>

2.4 Results and discussions

The surface morphology and crystalline quality of sample A were investigated by scanning electron microscopy (SEM), and energy dispersive X-ray analysis (EDX) and Raman spectroscopy (excited by a 633-nm laser). SIMS analysis of sample B was conducted to investigate contaminant concentration from the discharging antenna during point-arc remote MPCVD growth at various temperatures.

2.4.1 Morphology of the selectively grown diamond.

The SEM image in **Figure 2.8** in different magnification indicate successful epitaxial growth at where was not masked by SiO₂. **Figure 2.9 (a)** shows a SEM image obtained from sample A immediately after point-arc remote CVD growth. The bright areas in **Figure 2.8(a)** show the selectively grown region with the symmetric pattern generally utilized in MOSFET electrodes; the size of the pattern was $75 \times 60 \mu\text{m}^2$. The image confirmed the successful selective growth of the target patterns by the proposed method. It is noticed there were massive characteristic geometrical patterns of squares, partially squares and lines on the surface of selectively grown region, all of them had same orientation, and the length of a side of the square is about $2.6 \mu\text{m}$. These patterns were considered as stacking faults (SFs). In the case of silicon, the geometry of SFs on the epitaxial layer surface is dependent on the substrate orientation. For (100) silicon substrates, the SFs generally grow along inclined $4 \{111\}$ planes leads to an inverted tetrahedron, thus the etching figures of SFs will show in the form of square patterns. There are literatures proposed the SFs geometry relationship that is the grown layer thickness is approximately 70% of the length of a side of the SFs square pattern.³⁴⁻³⁶ The geometrical structures and

geometry relationship support our hypothesis on the square patterns. The geometry graph of SFs inside the grown layers were shown in **Figure 2.9 (b)**. The SFs nucleated from a dislocation site on the interface of substrate and the undoped layer (2 μm), subsequently grow along inclined $\{111\}$ planes, then propagate to the selectively grown layer (200 nm), resulting in four (111) planes adjacent to the substrate surface. The average length of a side of the square on the selective growth surface is about 2.7 μm .

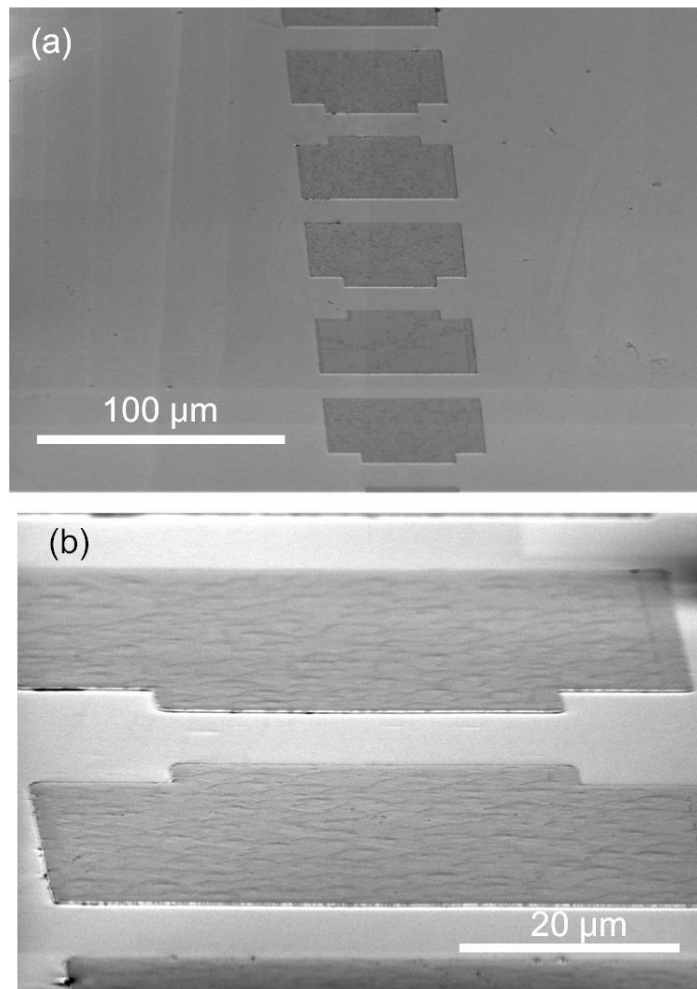


Figure 2.8 SEM images in different magnification of sample A taken after masks were removed.

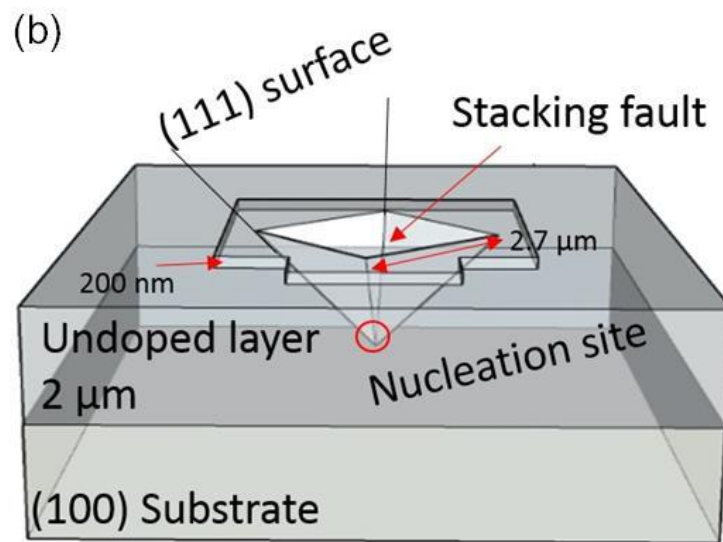
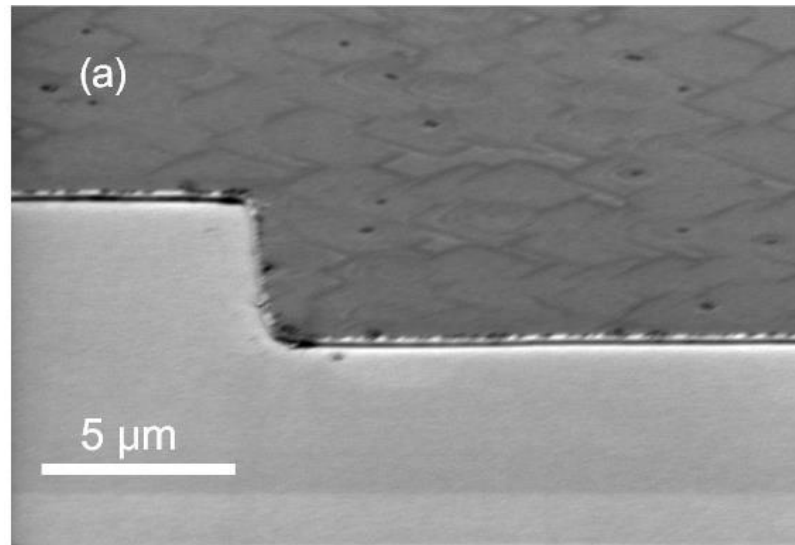


Figure 2.9 (a) SEM images of sample A taken after masks were removed. Dark areas show the selectively grown diamond, and bright areas show the substrate areas covered by masks during growth. (b) Geometry graph of SFs observed on the surface of selectively grown region. The SFs pattern on the selective growth region was magnified to display the geometrical structure completely.

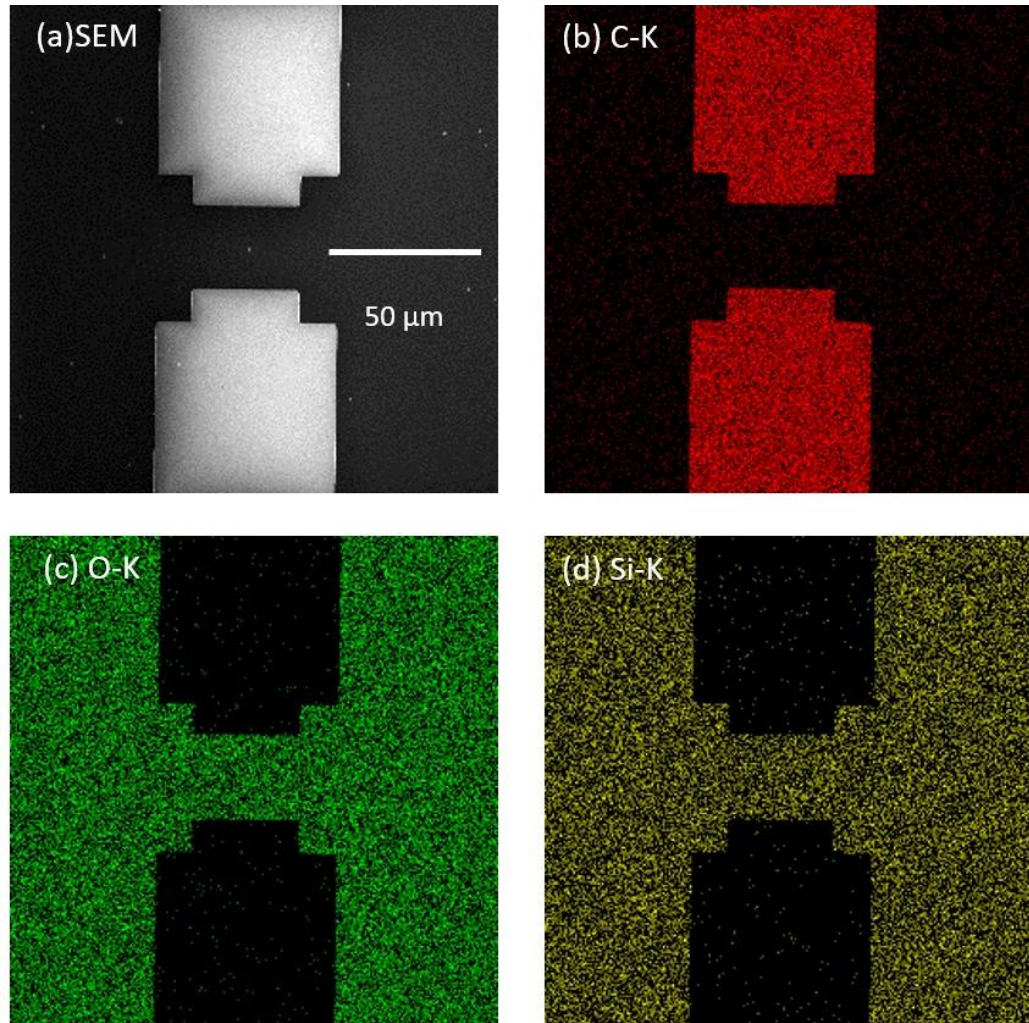


Figure 2.10 (a) SEM images of sample A where EDX mapping was performed. (b)-(d) EDX mapping of C-K, O-K, and Si-K, respectively.

Figure 2.10 (a) shows the SEM image of the area where the EDX maps in **Figure 2.10 (b), (c), and (d)** were acquired, for C-K, O-K, and Si-K, respectively. In **Figure 2.10 (b) (c) and (d)**, the outline of the SiO₂ masks can be observed clearly, indicating that the masks were quite stable, and no damage was induced. Neither diamond nucleation nor growth occurred on the mask surface, and there was no deformation or peel-off of masks, which usually happens during growth by conventional MPCVD.

2.4.2 Raman spectroscopy

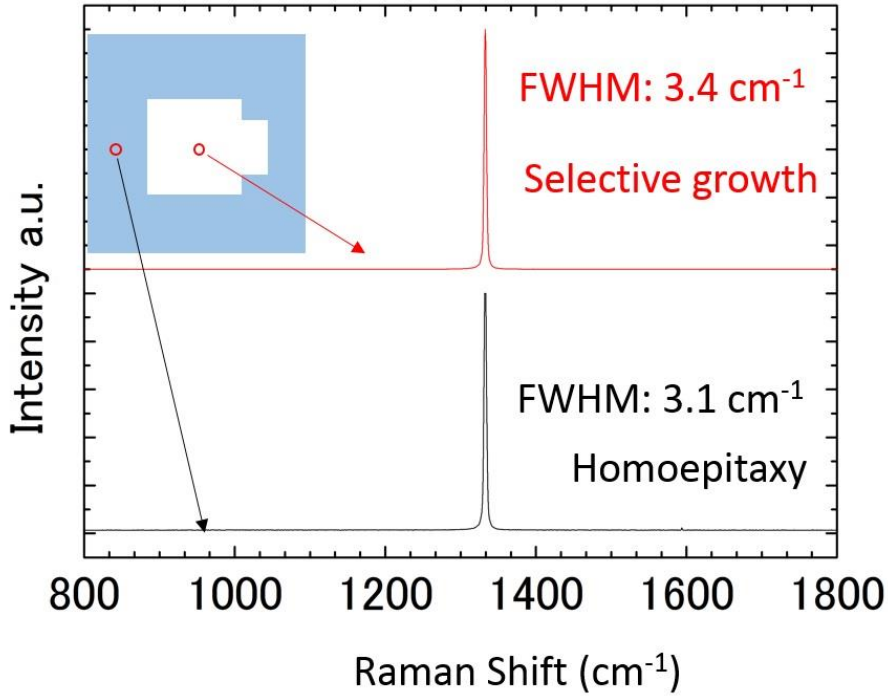


Figure 2.11 Raman spectra of selectively grown diamond and substrate, in red and black, respectively, from sample A. The measurement was conducted to evaluate crystalline quality of selectively grown diamond by point-arc remote MPCVD.

Raman spectroscopy was performed on sample A to characterize the crystalline quality of the selective growth region after masks were removed. In **Figure 2.11**, the spectrum plotted in red was taken from the selective growth region, and the one plotted in black was taken from the masked region. Both spectra were normalized to the 1332 cm⁻¹ band to allow direct comparison. In the red spectrum, the sharp peak at 1332 cm⁻¹ and the faint peak at approximately 1600 cm⁻¹ confirmed that the selective growth region was of high-quality diamond with negligible non-diamond components. Full width at half

maximum (FWHM) of selective growth layer and homoepitaxy layer was 3.4 cm^{-1} and 3.1 cm^{-1} , respectively, indicating both layers were of high degree crystallinity.

2.4.3 Secondary ion mass spectroscopy

Although there were no peaks attributed to molybdenum carbide (typically appear at 819 cm^{-1} and 995 cm^{-1}), the presence of molybdenum carbide could not be eliminated without additional analysis of the secondary ion mass spectroscopy (SIMS) profile because the impurity density could be under the Raman detection limit.^{37,38} Therefore, sample B was fabricated for impurity analysis by SIMS, as shown in **Figure 2.12**. Since sample B was not patterned, so it is believed that the quality of each layer grown by of the proposed apparatus was homogeneous. In this measurement, the sample surface was exposed to O_2^+ ions with an acceleration voltage of 8 kV. As shown in the figure, the Mo impurity concentrations were $4.4 \times 10^{16} \text{ cm}^{-3}$ and $1.5 \times 10^{17} \text{ cm}^{-3}$ at the surface and interface region, respectively.

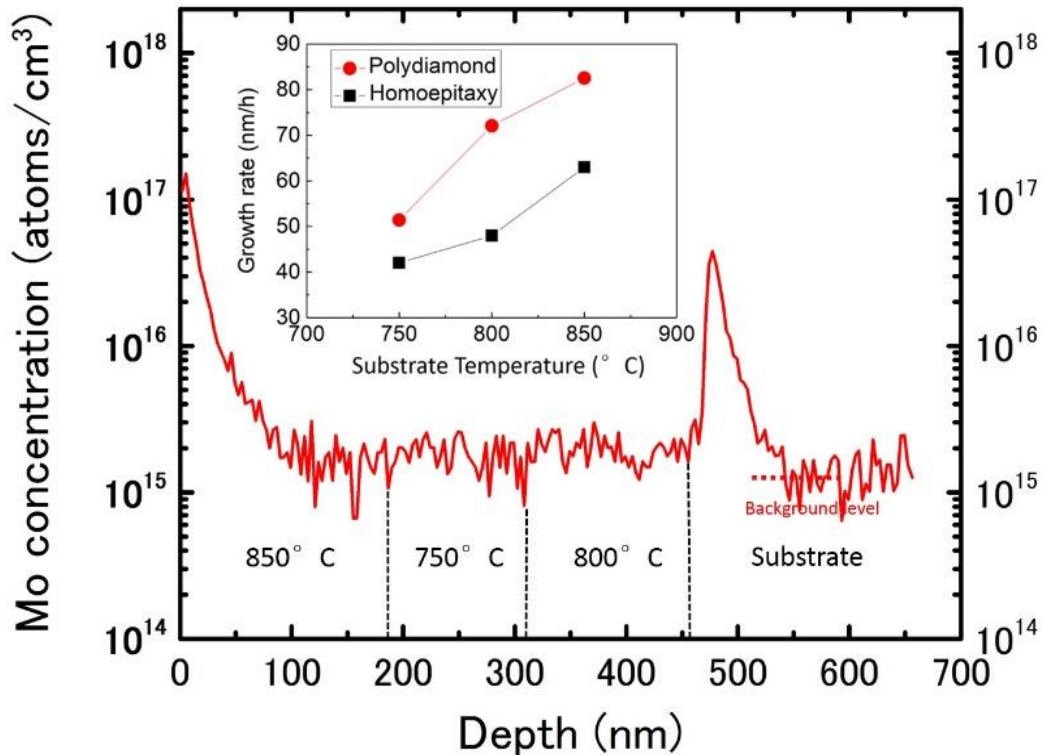


Figure 2.12 SIMS depth profile of Mo concentration in Sample B. This measurement was performed to estimate the Mo concentration due to antenna impurity in the homoepitaxy of the diamond layer by point-arc remote MPCVD. The inset presents the dependence of growth rates on substrate temperature. Red dots corresponding to the polydiamond growth on silicon wafer, and the black ones corresponding to homoepitaxy.

Despite these two peaks, which indicated some surface adsorption at the selective growth and interface regions, the average Mo concentration inside the homoepitaxy layers was detected at a background level of approximately $1.0 \times 10^{15} \text{ cm}^{-3}$, and this value is almost three orders of magnitude lower than the most recent advances in W contaminant concentration in the HFCVD process.²² This result indicates that although a small amount of Mo from the antenna and chamber wall was incorporated during growth, the diamond

deposited by point-arc remote MPCVD consisted of pure high-quality diamond with no contaminants, in agreement with the Raman spectra. The Mo concentration at the substrate and interface surface suggested that Mo from the antenna was dissociated by the microwave stimulation and adsorbed to the surface. However, the invasion appeared to stop at the surface, and was not finally incorporated into the recombined crystalline diamond. The mechanism of contamination will require further effort to elucidate.

In addition, the figure inset presents the growth rate of diamond powders on seeded silicon wafer at 750°C, 800°C, and 850°C, respectively (See details in 2.3.1). The boundary point of each homoepitaxy layer deposited under different temperature was based on the SIMS depth profile of nitrogen (**Figure 2.13**). The thickness of homoepitaxial layers are approximately 190 nm, 126 nm and 145 nm, respectively. Since the deposition time of each layer was 3 hours, the growth rate under 750°C, 800°C and 850°C is 42 nm h⁻¹, 50 nm h⁻¹ and 63 nm h⁻¹. In the insets of **Figure 2.12**, the dependence of growth rate on substrate temperature driven from homoepitaxy and polydiamond growth on silicon wafer were plotted in insets in black and red dots, respectively. Moreover, the homogeneous distributions inside the homoepitaxy layers were obtained at different substrate temperatures, suggesting the contaminant distribution was independent of substrate temperature in point-arc remote MPCVD. Comparing to various filament materials for HFCVD, there is always a strong correlation between contamination concentration and temperature. With a Ta filament, when the temperature varied from 1800 to 2000 °C, the Ta concentration in the diamond film grown by HFCVD varied from 8 ppm to 1200 ppm; with a W filament, as the temperature changed from 1800 to 2200 °C, the W concentration varied from 2 ppm to 300 ppm.¹⁸

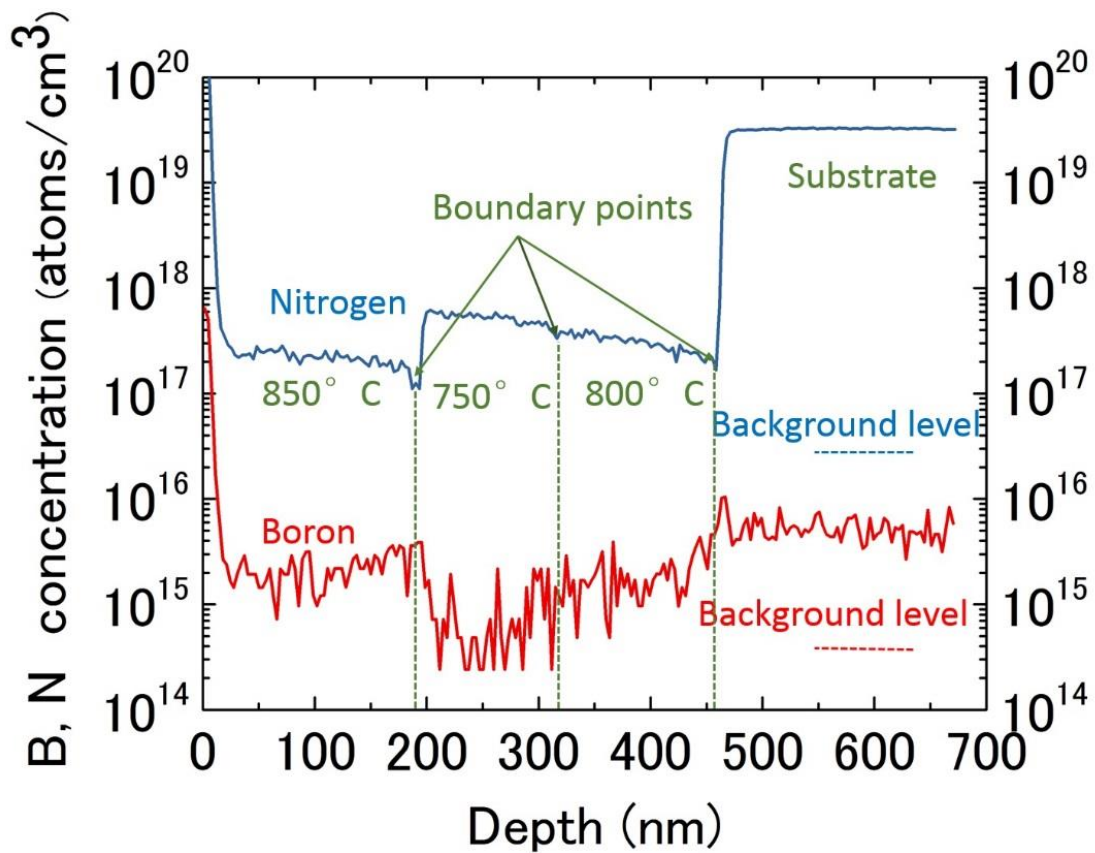


Figure 2.13 SIMS depth profile of boron and nitrogen concentration in Sample B. In this measurement, the sample surface was exposed to Cs^+ ion with an acceleration voltage of 8 kV.

There is a considerable concentration of nitrogen in the SIMS profile in **Figure 2.13**. This nitrogen is believed to be introduced due to the nitrogen impurities in reactant gases and vacuum systems leaks. In the reactant gases, hydrogen and methane contain nitrogen up to 0.05 ppm and 5 ppm, respectively, and there is no gas purifier in the apparatus currently. In addition, the O-rings are used in some vacuum flanges, which will cause a certain amount of leakage. Nitrogen impurities can be reduced to 10^{16} cm^{-3} by introducing a purifier to the gas lines.

2.4.4 Cross-sectional transmission electron microscopy

Basing on the scale bar, the thickness of the selectively grown diamond layer and SiO₂ mask are 360 nm and 220 nm, respectively. The cross-sectional transmission electron microscopy (TEM) image as **Figure 2.14 (a)** indicates the thickness of the selectively grown diamond layer at 800 °C is thicker than that calculated from SIMS profile, while the SiO₂ thickness differs from that measured by optical interference thickness meter, too. The accurate thickness of selective grown diamond and SiO₂ should be based on the TEM image, so the growth rate should be recalculated to 90 nm h⁻¹. When the diamond layer grew to the same thickness as masks, there is not only the normal growth along <001> but also lateral overgrowth starts on the SiO₂ mask surface simultaneously, forming the overgrowth edge illustrated by white broken circle in **Figure 2.14 (a)**. The lateral overgrowth region of are distorted since the growth direction changed. In the Energy Dispersive X-Ray Spectroscopy (EDS) profile of C mapping (**Figure 2.14 (b)**), the contour of selective growth including overgrowth is clearly visible, and the results are consistent with the (a). Moreover, at the interface of overgrowth diamond and SiO₂ mask is smooth and SiO₂ thickness has no tendency to become thinner. If the SiO₂ was etched by the hydrogen plasma during selective growth, the farther away from the overgrowth edge, the SiO₂ is thinner since it was under etching. Therefore, the SiO₂ mask showed stability and almost no etching under the high temperature hydrogen plasma dominated environment of selective growth.

Selective growth consists of normal growth region along the z-axis and lateral overgrowth region, both of which are analyzed by selected area electron diffraction (SAED), with the e-beam parallel to the 100 zone axis. **Figure 2.14 (c)** and **(d)** are the

SAED patterns with indexing, both the SAED patterns in (c) and (d) are identified as the typical single crystal diamond with $\langle 100 \rangle$ e-beam. According to the length of the scale bar of reciprocal space, the spot directly below the original spot is indexed as (220) surface which 1.2 Å from the origin of the direct lattice. The lower right side of the original spot is normal growth region and the lateral overgrowth region are high quality single-crystal diamonds.

In order to analyze the interface of undoped diamond and SiO₂, high-angle annular dark field (HAADF) image and EDS mapping were taken on the selective growth bottom area in larger magnification at where highlighted by broken blue circle in **Figure 2.14(b)**.

HAADF images of this region are shown in a, b and c, which are carbon and silicon mapping results using EDS. In the HAADF image (**Figure 2.15(a)**), elements with larger atomic number appear brighter. Based on **Figure 2.15 (b)**, the bright area in the left part of **Figure 2.15 (a)** is confirmed as the region of CVD and selectively grown diamond. A considerably brighter boundary was observed at the interface of the SiO₂/diamond in the masking area. The bright boundary indicates the atoms are heavier than C. In the EDS mapping of Si shown in **Figure 2.15 (c)**, the brighter boundary is confirmed as Si. After the sample was treated with HF, TEOS SiO₂ on O-terminated diamond without selective diamond growth process was completely etched off and C-Si was not dominantly formed, resulting in no Si signal. However, a clear Si signal is observed in **Figure 2.15 (c)** even after HF etching, indicating the presence of C-Si bonds; this layer is the C-Si diamond formed at high temperature during selective homoepitaxial growth of diamond and H

radical treatment. The mechanism of the C-Si bond and the application will be discussed in Chapter III.

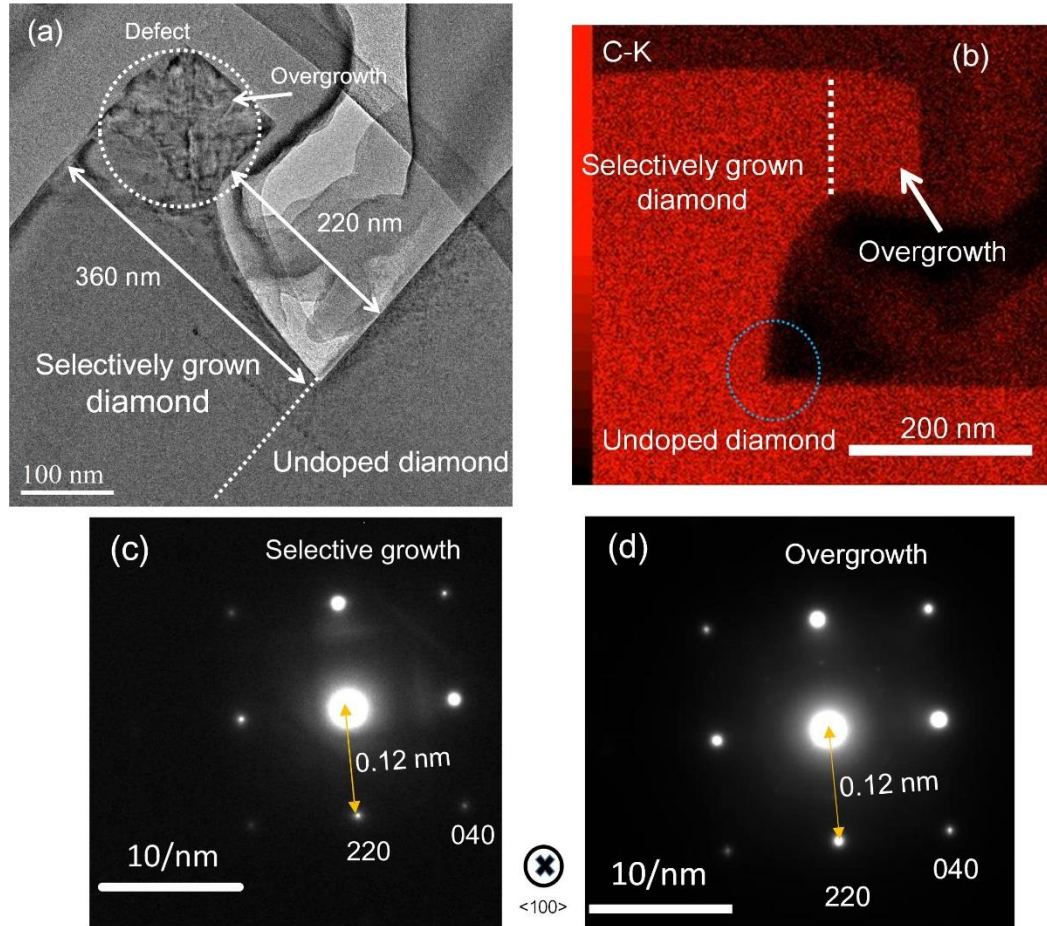


Figure 2.14 (a) cross-sectional TEM image of the selectively grown diamond. (b) EDS mapping of carbon in the same region as (a). The indexed SAED pattern from (c) normal growth region and (d) overgrowth region (white broken circle in (a)) with the beam parallel to the zone axis.

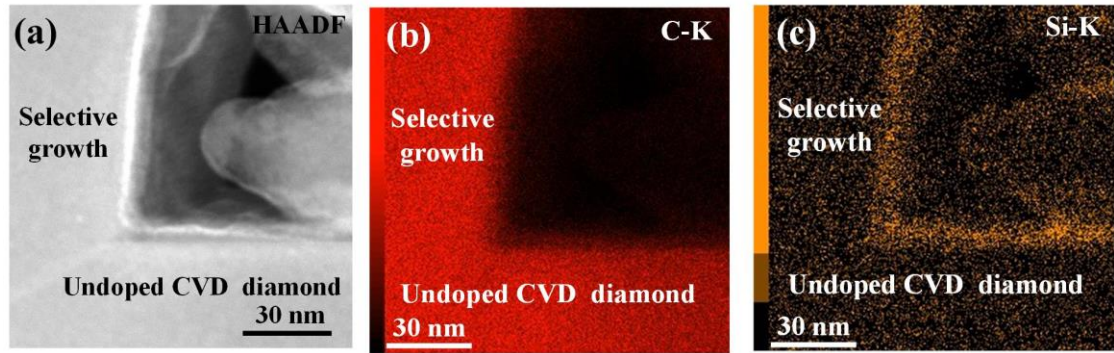


Figure 2.15 (a) HAADF image, (b) EDS mapping of C, and (c) EDS mapping of Si characterized at the masking area after SiO₂ was chemically removed.

2.5 Conclusion

Selective growth of diamond film was realized by employing point-arc remote MPCVD with SiO₂ masks. The contamination and mask distortion can be avoided because the plasma in this apparatus will not meet the substrate. These two characteristics are very important for the fabrication of fine patterns of high-performance electronic devices. Slow growth rate and high-reproducibility were found to be associated with moderate reaction conditions, and thus the proposed technique can overcome the existing disadvantages of the techniques of selective diamond growth, with considerable potential in precise control thickness of the selective growth layer in various fields, including applications such as semiconductor devices that require high-quality thin film.

References

- ¹ H. Kawarada, H. Tsuboi, T. Naruo, T. Yamada, D. Xu, A. Daicho, T. Saito, and A. Hiraiwa, *Appl. Phys. Lett.* **105**, 013510 (2014).
- ² H. Umezawa, T. Matsumoto, and S.-I. Shikata, *IEEE Electron Device Lett.* **35**, 1112 (2014).
- ³ T. Suwa, T. Iwasaki, K. Sato, H. Kato, T. Makino, M. Ogura, D. Takeuchi, S. Yamasaki, and M. Hatano, *IEEE Electron Device Lett.* **37**, 209 (2015).
- ⁴ T. Makino, H. Kato, N. Tokuda, M. Ogura, D. Takeuchi, K. Oyama, S. Tanimoto, H. Okushi, and S. Yamasaki, *Phys. Status Solidi A* **207**, 2105 (2010).
- ⁵ C. Uzan - Saguy, C. Cytermann, R. Brener, V. Richter, M. Shaanan, and R. Kalish, *Appl. Phys. Lett.* **67**, 1194 (1995).
- ⁶ H. Kato, T. Makino, M. Ogura, N. Tokuda, H. Okushi, and S. Yamasaki, *Applied physics express* **2**, 055502 (2009).
- ⁷ T. Teraji, M. Katagiri, S. Koizumi, T. Ito, and H. J. J. o. a. p. Kanda, **42**, L882 (2003).
- ⁸ H. Kawashima, S. Ohmagari, H. Umezawa, and D. Takeuchi, *Jpn. J. Appl. Phys.* **58** (2019).
- ⁹ T. Teraji, *Phys. Status Solidi A* **203**, 3324 (2006).
- ¹⁰ M. Tetsuro and K. Takeshi, *Jpn. J. Appl. Phys.* **33**, 4053 (1994).
- ¹¹ T. Teraji, S. Mitani, C. Wang, and T. Ito, *Journal of crystal growth* **235**, 287 (2002).
- ¹² S. Ohmagari, T. Matsumoto, H. Umezawa, and Y. Mokuno, *Thin Solid Films* **615**, 239 (2016).
- ¹³ T. Kageura, M. Hideko, I. Tsuyuzaki, S. Amano, A. Morishita, T. Yamaguchi, Y. Takano, and H. Kawarada, *Diam. Relat. Mater.* **90**, 181 (2018).

- ¹⁴ S.-T. Lee, Z. Lin, and X. Jiang, *Materials Science and Engineering* **25**, 123 (1999).
- ¹⁵ M. Schwander and K. Partes, *Diam. Relat. Mater.* **20**, 1287 (2011).
- ¹⁶ M. Kasu, *Progress in Crystal Growth and Characterization of Materials* **62**, 317 (2016).
- ¹⁷ M. Stammler, H. Eisenbeiß, J. Ristein, J. Neubauer, M. Göbbels, and L. Ley, *Diam. Relat. Mater.* **11**, 504 (2002).
- ¹⁸ S. Ohmagari, K. Srimongkon, H. Yamada, H. Umezawa, N. Tsubouchi, A. Chayahara, S. Shikata, and Y. Mokuno, *Diam. Relat. Mater.* **58**, 110 (2015).
- ¹⁹ H.-J. Hinneberg, M. Eck, and K. Schmidt, *Diam. Relat. Mater.* **1**, 810 (1992).
- ²⁰ J. Cifre, F. Lopez, J. Morenza, and J. Esteve, *Diam. Relat. Mater.* **1**, 500 (1992).
- ²¹ M. Griesser, G. Stingeder, M. Grasserbauer, H. Baumann, F. Link, P. Wurzinger, H. Lux, R. Haubner, and B. Lux, *Diam. Relat. Mater.* **3**, 638 (1994).
- ²² P. M. Menon, A. Edwards, C. Feigerle, R. Shaw, D. Coffey, L. Heatherly, R. Clausing, L. Robinson, and D. Glasgow, *Diam. Relat. Mater.* **8**, 101 (1999).
- ²³ S. Ohmagari, H. Yamada, H. Umezawa, A. Chayahara, T. Teraji, S.-i. J. D. Shikata, and R. Materials, **48**, 19 (2014).
- ²⁴ M. Hamada, T. Teraji, and T. Ito, *Jpn. J. Appl. Phys.* **44**, L216 (2005).
- ²⁵ M. Nagase, K. Watanabe, H. Umezawa, and S. Shikata, *Jpn. J. Appl. Phys.* **51**, 070202 (2012).
- ²⁶ G. Zhong, M. Tachiki, H. Umezawa, T. Fujisaki, H. Kawarada, and I. Ohdomari, *Chemical Vapor Deposition* **10**, 125 (2004).
- ²⁷ G. Zhong, T. Iwasaki, H. Kawarada, and I. Ohdomari, *Thin Solid Films* **464**, 315 (2004).
- ²⁸ G. Zhong, T. Iwasaki, K. Honda, Y. Furukawa, I. Ohdomari, and H. Kawarada, *Jpn. J. Appl. Phys.* **44**, 1558 (2005).

- ²⁹ M. Katagiri, N. Sakuma, M. Suzuki, T. Sakai, S. Sato, T. Hyakushima, M. Nihei, and Y. Awano, *Jpn. J. Appl. Phys.* **47**, 2024 (2008).
- ³⁰ T. Ohashi, R. Kato, T. Ochiai, T. Tokune, and H. Kawarada, *Diam. Relat. Mater.* **24**, 184 (2012).
- ³¹ N. Taniyama, M. Kudo, O. Matsumoto, and H. Kawarada, *Jpn. J. Appl. Phys.* **40**, L698 (2001).
- ³² Y. A. Lebedev, M. Mokeev, A. Tatarinov, V. Shakhatov, and I. Epstein, *Journal of Physics D: Applied Physics* **41**, 194001 (2008).
- ³³ T. Teraji, H. Wada, M. Yamamoto, K. Arima, and T. Ito, *Diam. Relat. Mater.* **15**, 602 (2006).
- ³⁴ T. Chu and J. Gavaler, *Journal of The Electrochemical Society* **110**, 388 (1963).
- ³⁵ S. Mendelson, *J. Appl. Phys.* **35**, 1570 (1964).
- ³⁶ S. Mendelson, *Materials Science and Engineering* **1**, 42 (1966).
- ³⁷ T.-C. Xiao, A. P. York, H. Al-Megren, C. V. Williams, H.-T. Wang, and M. L. H. Green, *Journal of Catalysis* **202**, 100 (2001).
- ³⁸ M.-L. Frauwallner, F. López-Linares, J. Lara-Romero, C. E. Scott, V. Ali, E. Hernández, and P. Pereira-Almao, *Applied Catalysis A: General* **394**, 62 (2011).

Chapter III Novel diamond MOSFET fabrication process by selectively grown source/drain and Si-terminated channel

During selective epitaxial growth of diamond through SiO₂ masks, silicon terminations were formed on diamond surface by replacing oxygen terminations under the masks. The high temperature of selective growth and its reductive atmosphere possibly allowed Si atoms in SiO₂ to interact with diamond surface, resulting in silicon terminated diamond (C-Si diamond) composed of monolayer or thin multi-layers of carbon and silicon bonds on diamond. Diamond metal oxide semiconductor field effect transistors (MOSFETs), with C-Si diamond channel and selectively grown undoped or heavily boron-doped (p⁺) source/drain (S/D) layers, have been fabricated. Both the MOSFETs with undoped and p⁺ S/D exhibited enhancement mode (normally-off) FET characteristics. The drain current (I_{DS}) of the undoped device reached -17 mA/mm with threshold voltage (V_T) -19 V; the p⁺ device attained a high I_{DS} -165 mA/mm with V_T of -6 V exhibiting one of the best normally off diamond FETs. Transmission electron microscopy and energy dispersive X-ray spectroscopy confirmed the presence of C-Si diamond under the SiO₂ masking area. The effective channel mobility and interface state density at the C-Si/ SiO₂ (220 nm)/Al₂O₃

(100 nm) MOS capacitor are $102 \text{ cm}^2 \text{ V}^{-1} \text{ s}^{-1}$ and $4.6 \times 10^{12} \text{ cm}^{-2} \text{ eV}^{-1}$, respectively. This is the first demonstration of the MOSFET operation of C-Si diamond and provides an alternative approach for diamond devices.

3.1 Background

The electrical properties of diamonds can be significantly altered by surface modification.^{1,2} Owing to high hole density (up to 10^{13} cm^{-3}), low activation energy (less than 50 meV), and high carrier mobility (around $100 \text{ cm}^2 \text{ V s}^{-1}$),^{1,3-5} H-terminated diamond (C-H diamond) has led to significant breakthroughs; high current output, wide temperature operation, and high breakdown voltage have been achieved in the development of diamond metal oxide semiconductor field effect transistors (MOSFETs).⁶⁻⁸ The spontaneous polarization of C-H dipole was reported to be associated with hole accumulations. Spontaneous polarization of C-H owing to the different electronegativity (C: 2.5, H: 2.1) cause hole accumulation of the hydrogen-terminated diamond (C-H diamond) surface.⁹ The build-in electric field of C-H dipole, which points from the hydrogen pole to carbon pole. Under action of electric field, hole carriers attracted by the interfacial negative charges transfer from diamond surface adsorbates to the bottom of C-H dipoles, while positive charging acceptors are located at the top of them. The energy band bending attributes to hole accumulations, then resulting surface conductivity of hydrogen-terminated diamond. As shown in **Figure 3.1**, the electronegativity of Si is 0.7 Pauling unit lower than that of C, the polarity of C-Si dipole should be stronger than that of C-H dipole. Basing on this speculation, more holes accumulate at the C-Si diamond (C-H diamond) surface.

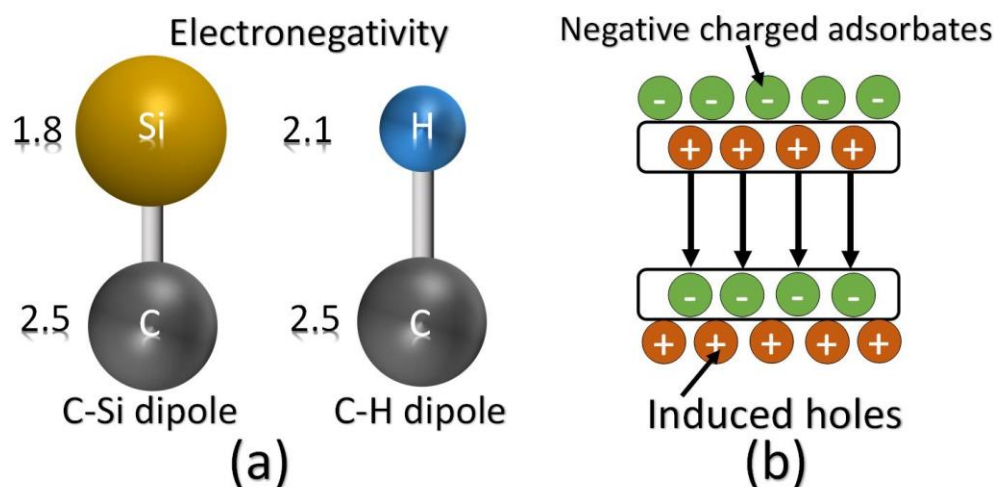


Figure 3.1 (a) Schematic diagram of C-Si dipole and C-H dipole due to the difference in electronegativity of C, Si and H. (b) Schematic diagram of hole accumulation induced by the C-H dipole and negative charge adsorbates.

However, the electronics basing C-Si diamond surface has not been reported intensively. The successful formation and surface characterization of silicon-terminated diamond (C-Si diamond) in vacuum were reported by Schenk et al, they form the C-Si surface by on hydrogen termination was produced previously on type IIb (100) diamond which contains boron in range of $5 \times 10^{18} \sim 1 \times 10^{19} \text{ cm}^{-3}$, then a 2.7 Å thick layer of Si was deposited on the C-H diamond surface, C-Si diamond was established by post annealing at 920°C for 15 min in vacuum.¹⁰ The electron affinity of pristine C-Si diamond surface is proved to be -0.86 eV.¹¹ Although upward band bending at oxidized C-Si diamond has been reported,¹² it has not be recognized as suitable termination for electronic device applications. The electrical measurement of the two-dimensional hole gas (2DHG) and the control of 2DHG by field effect have not been examined. C-Si diamond as a channel should be considered to have different device physics from C-H diamond for MOSFET, because

this termination directly connect diamond with SiO₂¹³ which is the most reliable insulator in MOS power devices. It has been extensively reported that using MoO₃ and other transition metal oxide with large positive electron affinity, as the acceptor to increase the hole concentration.¹⁴ However, taking their narrow bandgap into account, SiO₂ having the widest bandgap is more advantageous for power device applications.

As shown in **Figure 2.13** of the Chapter II, basing on silicon mapping profile the taken at the bottom of the selectively grown diamond by EDS, single or very thin multi-layer C-Si diamond at the interface were confirmed. Inspired by this result, we believe that selective growth of diamond using SiO₂ mask is applicable to fabricate C-Si diamond electronic device. In this work, oxidized C-Si diamond and its MOSFET operation with a SiO₂ gate insulator were demonstrated for the first time. Here, C-Si diamond is defined as diamond covered by monolayer or thin multi-layers of C-Si bonds. MOSFETs with undoped and heavily boron-doped (p⁺) source/drain (S/D) layers both exhibited normally-off mode operation. This is highly desirable as it offers the advantage of avoiding switching malfunctions and has been realized in diamond FETs^{8,15-20}, but the drain current densities were not high enough. In C-Si diamond MOSFETs, the drain current (I_{DS}) was effectively modulated by controlling the gate voltage (V_{GS}). For the undoped S/D ("Device A") the maximum I_{DS} was -17 mA/mm with a threshold voltage (V_T) of -19 V; for the p⁺ S/D MOSFET maximum I_{DS} was -165 mA/mm with V_T of -6 V, showing normally-off mode.

3.2 Device fabrication

As illustrated in **Figure 3.2**, two types of C-Si diamond MOFETs with undoped and p⁺ S/D layers were fabricated, respectively. The experimental process until selective

growth²¹ of the former one are the same as the experimental process in **Table 2.4** Chapter II. While the latter was selectively grown by NIRIM-type MPCVD. Since the two MOSFETs share the same fabrication process except the selective growth, so the experimental process are summarized in in **Table 3.2** with schematic diagram based on the C-Si MOSFET with p⁺ S/D layer. From the strong acid boiling to the selective growth, please refer to **Table 2.4**, experimental process in this chapter will focus on the device fabrication, starting from the process just after selective growth.

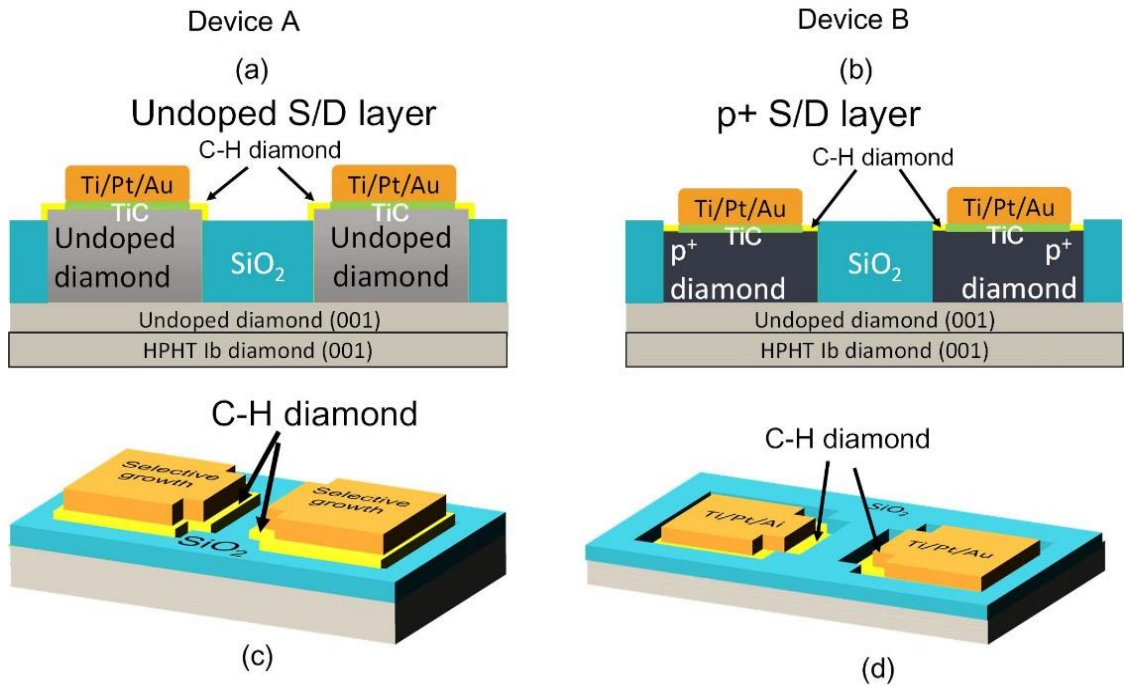


Figure 3.2 (a) and (c) cross-sectional schematic diagram and stereogram C-Si diamond MOSFET with undoped S/D layer (330 nm), respectively. (b) and (d) cross-sectional schematic diagram and stereogram C-Si diamond MOSFET with p⁺ S/D layer(130 nm), respectively.

As shown in **Figure 3.2**, the schematic diagram shows the process of p⁺ Homoepitaxial undoped (330 nm) and heavily boron-doped (p⁺) (130 nm) diamond film were selectively grown for Devices A and B respectively. The experimental parameter of undoped diamond layer of Device A can be seen in **Table 2.1** in Chapter II. In the case of Device B which is composed of p⁺ S/D layer, the boron concentration of the p⁺ diamond film was approximately 10²¹ cm⁻³. The experimental parameters are shown in **Table 3.1**.

Table 3.1 the experimental parameter for the p⁺ diamond selective growth (Device B)

Parameters	Values
Stage material	Mo
Substrate temperature	720°C
Chamber pressure	110 Torr
Microwave power	400 W
H ₂ flow rate	85 sccm
CH ₄ flow rate	5 sccm
TMB flow rate	3.0 sccm (20000 ppm)
Growth rate	900 nm/h
B-doped diamond thickness	130 nm

After the selective growth, Ti/Pt/Au (20 nm/30 nm/100 nm, respectively) was locally formed by e-beam evaporation inside the selective growth pattern at a distance of

5 μm (corresponding to the area inside the dotted line shown in **Figure 3.3 (a)**) through patterned photoresist and successive lift-off. TiC has been proposed beneficial to form low Schottky barrier height on both undoped and boron-doped diamond.^{22,23} The sample was annealed at 500°C in a hydrogen atmosphere for 30 min to form TiC contact which located at 3 nm²³ beneath the metals. Hydrogen radical treatment was performed through remote plasma for 30 min to form the C-H diamond surface between S/D and the SiO₂ covered channel (blue region in Fig.3.3 (b)). C-H surfaces were also formed at the sidewalls of the overhang structured diamond after hydrogen plasma treatment.²⁴ Here the hydrogen termination is essential for Device A's operation since the space between S/D metal contact and the surface require to be conductive. However, it is not necessary for Device B since p⁺ diamond layer surface is not a channel in this case.

Subsequently, prior to device isolation, all the SiO₂ except for the channel area was removed via ICP-RIE. Here the C-Si bonding formed on the surface and sidewall of diamond were slightly over etched. Next, as illustrated in **Figure 3.3(c)**, the surface and sidewall of diamond without SiO₂ covered was terminated by oxygen by O₂ plasma ashing, thus the MOSFETs were electrically isolated. 100 nm Al₂O₃ was deposited using atomic layer deposition (ALD) at 450°C, with trimethylaluminum (TMA) and H₂O as the aluminum source and oxidant, respectively. Al₂O₃ allows for high-reliability passivation of the 2DHG induced by C-H diamond.^{25,26} The Al₂O₃ deposited on the S/D was etched by alkaline solutions to expose the electrodes for subsequent electrical characterization. Finally, a 100 nm Al gate with 2 μm overlap ($L_{OP} = 2 \mu\text{m}$) to the S/D was evaporated. The gate width (W_G), gate length (L_G) and length of SiO₂ (L_{SiO_2}) = were 25 μm , 20 μm and 6 μm respectively.

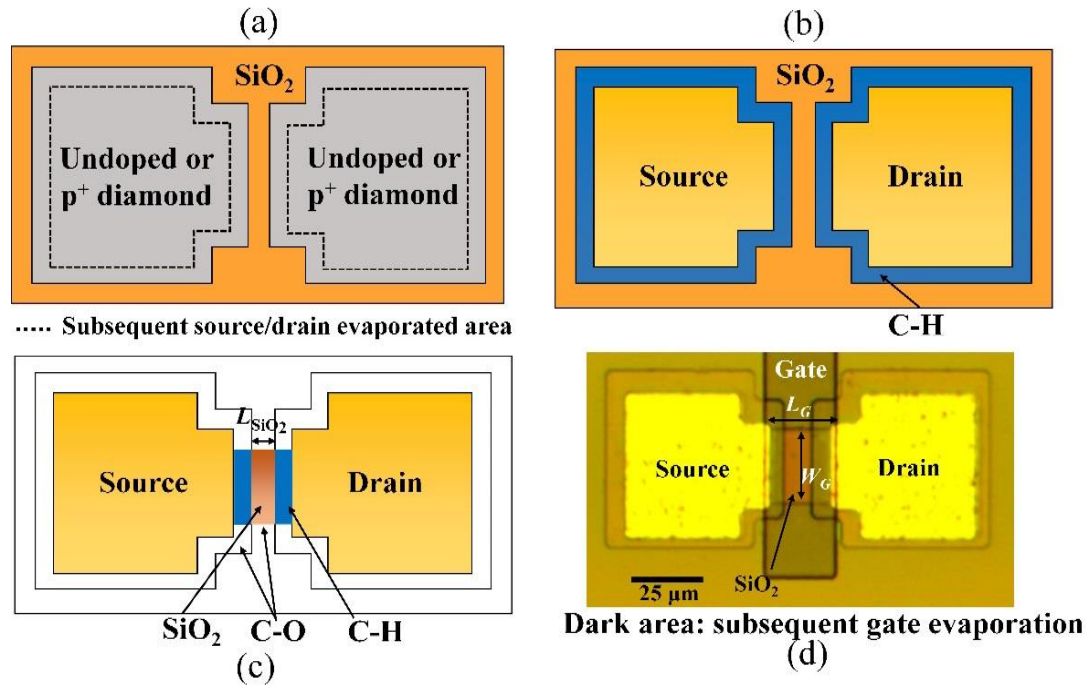
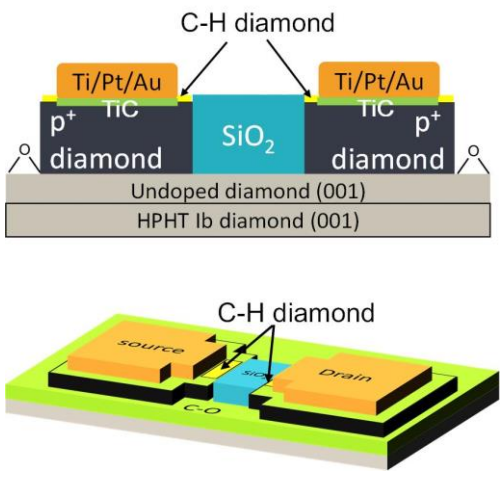
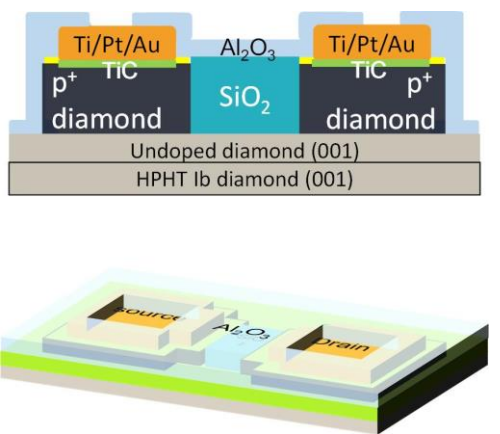
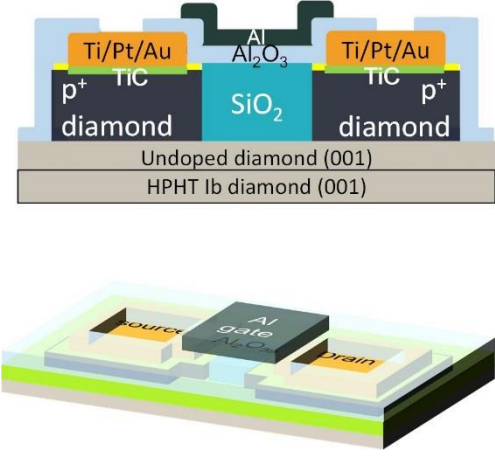


Figure 3.3 Device processing sequence of oxidized C-Si MOSFET with the SiO_2 gate insulator. (a) Top view of the sample after selective growth masked by SiO_2 before source/drain (S/D) formation. (b) Top view after metallization for S/D, hydrogen radical treatment (C-H termination, blue region) outside of SiO_2 mask. (c) Top view after electrical isolation by C-O termination (white region). Lines in the C-O region is the step of selectively grown diamond epitaxial layer. (d) Top view by optical image after ALD of Al_2O_3 and just before Al gate deposition. ALD- Al_2O_3 covers the full area. The photo resist also covers the area except for the dark area which is the free space for Al gate deposition.

Table 3.2 MOSFET fabrication process

	<p>1. Metallisation for S/D and ohmic contact formation</p>	<p>Substrate: selectively grown undoped/p⁺ diamond with SiO₂ mask</p> <ol style="list-style-type: none"> 1. double-layer resist spin 2. UV lithography 3. development 4. metallisation (Ti/Pt/Au) 5. lift-off 6. Annealing in H₂ (form TiC) 7. H-termination treatment
	<p>2. SiO₂ (except channel) remove</p>	<ol style="list-style-type: none"> 1. single-layer resist spin 2. UV lithography 3. development 4. ICP-RIE

	<p>3.Electric isolation</p>	<p>O₂ Plasma ashing for 2 min</p>
	<p>4.gate insulator deposition</p>	<ol style="list-style-type: none"> 1.ALD-Al₂O₃ 100 nm 450 2.Single-layer resist spin 3.UV lithography 4. Development 5.Al₂O₃ etched via alkaline solution

 <p>The diagram illustrates the structure of a diamond-based device. The cross-sectional view shows a substrate of HPHT Ib diamond (001) with an undoped diamond (001) layer on top. This is followed by a p+ diamond layer, a TiC layer, and a Ti/Pt/Au layer. A central SiO₂ gate is covered with Al₂O₃ and Al. The 3D view shows the Source, Drain, and Gate regions.</p>	<p>5. Metallization for gate</p>	<ol style="list-style-type: none"> 1. Double-layer resist spin 2. UV lithography 3. Development 4. Metallisation (Al 100 nm) 5. Lift-off
--	--------------------------------------	---

3.3 Electrical Characterization of C-Si MOSFET with undoped S/D layer

The current-voltage (I - V) and transfer characteristics of the MOSFETs were evaluated in vacuum at room temperature 298K (RT). By performing transmission electron microscopy (TEM) and (EDS) measurements, the SiO₂/diamond interface after selective homoepitaxial growth has been analyzed. To clarify the interfacial layer, SiO₂ was chemically removed using 46% hydrofluoric acid (HF) at RT for 20 min. Using TEM and EDS, the presence of C-Si diamond was examined.

For device A **Figure 3.4 (a) and (c)** show the I_{DS} versus the drain voltage (V_{DS}) (I_{DS} - V_{DS} characteristic) in linear scale for MOSFET I and II, respectively, measured as the V_{GS} , varied from -60 V to 4 V in increments of 4 V in vacuum at RT. Notably, I and II have different effective lengths of the source and drain (L_{SD}), the same L_G and W_G of 20 μm and 25 μm , respectively. Consequently, there are variations in device operation. Characteristics of I show the highest current density, while that of II shows the highest on-off ratio. The $I_{DS,max}$ of I and II were -17 mA/mm and -4.5 mA/mm, respectively. These values of I_{DS} are comparable to those of the normally-off diamond FETs reported in the literature, when the channel lengths are normalized to the same size.^{8,17} In both I and II, I_{DS} were effectively modulated by controlling V_{GS} . The transconductance (g_m) of I and II were 1 mS/mm and 0.2 mS/mm, respectively.

The transfer characteristics of I and II are shown in **Figure 3. 4(b) and (d)**, where $-I_{DS}$ in logarithmic scale is plotted against V_{GS} at $V_{DS} = -30$ V. V_T was estimated as the V_{GS} where the $-I_{DS}$ decreased by four orders of magnitudes from the on-state current. Therefore, the V_T values of I and II were -19 V and -25 V, respectively. As shown in the figures, the

drain off-state currents are suppressed to $10^{-10}\sim 10^{-11}$ A/mm, and the on/off ratio of approximately 10^7 and 10^6 were achieved at RT for I and II, respectively.

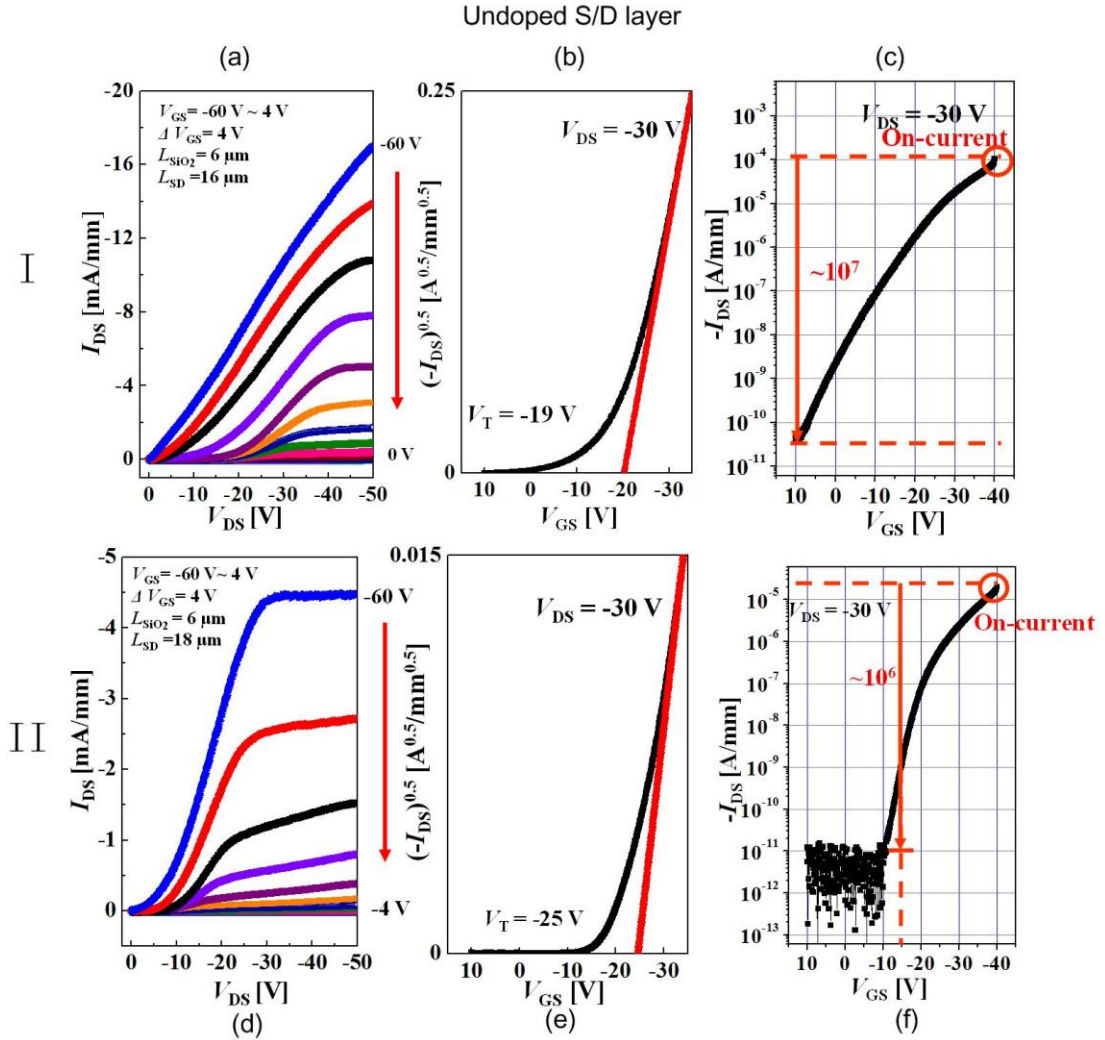


Figure 3.4 (a), (c) I_{DS} – V_{DS} characteristics at V_{GS} varied from -60 V to 4 V in increments of 4 V, (b), (d) $(-I_{DS})$ – V_{GS} characteristics in logarithmic scale at V_{DS} of -30 V for MOSFET I and II. The $I_{DS,max}$ and g_m were -17 mA/mm and 1 mS/mm, respectively, for I and -4.5 mA/mm and 0.2 mS/mm, respectively, for II. All characteristics were measured in vacuum at RT.

The values of I_{DS} and g_m are not as large as those of advanced C-H diamond MOSFETs.²³⁻²⁵ Considering the drain current path from the source to drain; however, the hole current path is extraordinary hazardous. As shown in **Figure 3.5**, the hole current enters from the source contact and travels through the C-H diamond surface covered by Al_2O_3 , which is normal current path. Before reaching the (001) diamond channel covered by SiO_2 , the hole current passes through the over-hang structured diamond and the sidewall in masking area, where the homoepitaxial SG diamond was exposed to SiO_2 .

The original diamond surface in the masking area was composed of C-O bond before SiO_2 deposition took place, followed by SG using high temperature plasma deposition. Therefore, the strong surface states existing at the C-O surface prevent the MOS structure from undergoing effective current modulation by the electric field.^{26, 27} However, the hole current was effectively modulated by the gate electric field at the SiO_2 / (001) After passing through the channel, the hole current passes through the over-hang structured diamond and the sidewall in the masking area and finally reaches the drain contact through the Al_2O_3 /C-H area of the diamond. The hole current at the over-hang structured area and the side wall area is difficult to be modulated by gate electric field, causing highly resistive character of low drain current region of **Figure 3.6** (a) and (d).

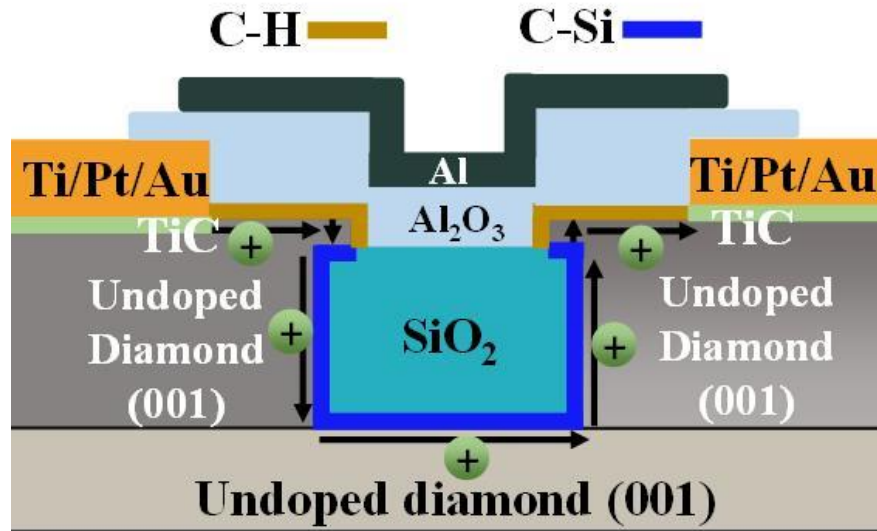


Figure 3.5 Schematic diagram of carrier path in C-Si MOSFET with undoped S/D layer (Device A).

3.4 Improved characteristic of C-Si diamond MOSFET with p⁺ S/D layer

In device A, except that part of the channel are parallel to the gate electric field, the high S/D contact resistance also contributes to the poor I_{DS} . In order to overcome this deficiency, C-Si diamond MOSFET with selectively grown p⁺ S/D layer was fabricated, shortening the channel length and realize high I_{DS} with normally-off characteristics. To illustrate more intuitively the improvement of device performance realized by reducing contact resistivity, we compared the characteristics of I in deviceA (undoped) and B (p⁺) in **Figure 3.6**.

Figure 3.6 (a) and (c) show I_{DS} versus drain voltage V_{DS} (the I_{DS} - V_{DS} characteristic) on a linear scale for Devices A and B respectively, measured as V_{GS} varied from -60 V to 4 V in increments of 4 V, in vacuum at RT. The two devices have the same dimensions: L_G , W_G and L_{SiO_2} as given above, the effective length of S/D (L_{SD}) are 16 μm and 6 μm for Device A and B, respectively. For Device A the maximum I_{DS} was -17 mA/mm. Due to the high on-resistivity in the linear region of Device A, the V_T is determined by plotting $(-I_{DS})^{0.5}$ versus V_{GS} at $V_{DS} = -30$ V and extrapolating the curve to $I_{DS} = 0$ A.²⁷ As shown in **Figure 3.6(b)**, A shows normally-off mode operation and the V_T is -19 V. For Device B (**Figure 3.6(d)**), maximum $I_{DS} = -165$ mA/mm, which is ten times higher than that of Device A. Since the S/D resistivity is negligible in Device B and equivalent to the advanced C-H diamond MOSFETs²⁷⁻²⁹ at the similar device size such as L_{SD} . Since the S/D resistivity is negligible in Device B, the high I_{DS} is controlled by (001) channel at the newly formed SiO₂/diamond interface. **Figure 3.6(e)** shows Device B's $(-I_{DS})^{0.5}$ - V_{GS} characteristic plotted at $V_{DS} = -10$ V, with = -6 V indicating normally-off operation. The on/off ratios of Devices A (**Figure 3.7(c)**) and B (**Figure 3.6(f)**) were 10^7 and 10^8 , respectively.

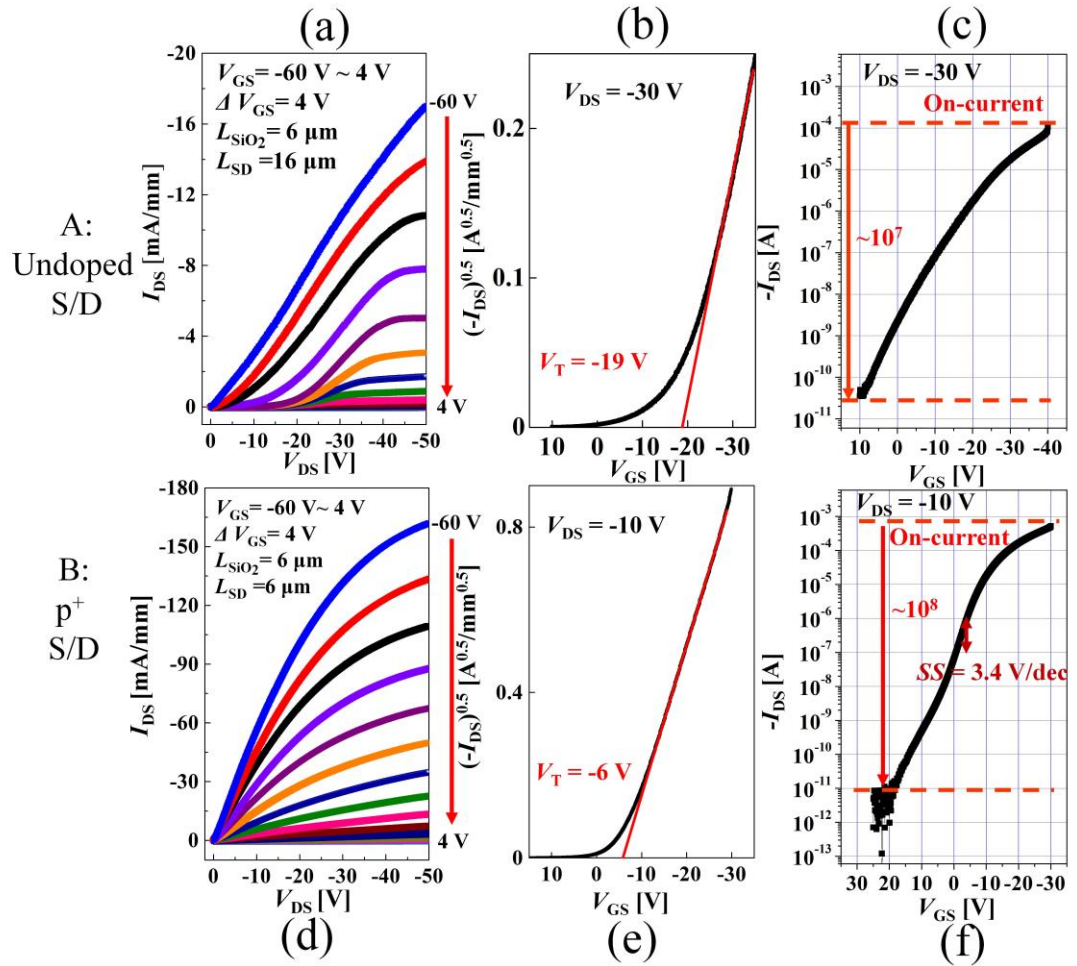


Figure 3.6 Characteristics comparison of the C-Si diamond MOSFET with undoped and p^+ S/D layers. (a,d) $(-I_{DS})-V_{DS}$ characteristics as V_{GS} varies from -60 V to 4 V in 4 V steps for (a) Device A, (d) Device B; (b,e) $(-I_{DS})-V_{GS}$ characteristics on linear scale at (b) $V_{DS} = -30\text{ V}$ for Device A and (e) $V_{DS} = -10\text{ V}$ for Device B; (c,f) $(-I_{DS})-V_{GS}$ characteristics on logarithmic scale at (c) $V_{DS} = -30\text{ V}$ for Device A and (f) $V_{DS} = -10\text{ V}$ for Device B.

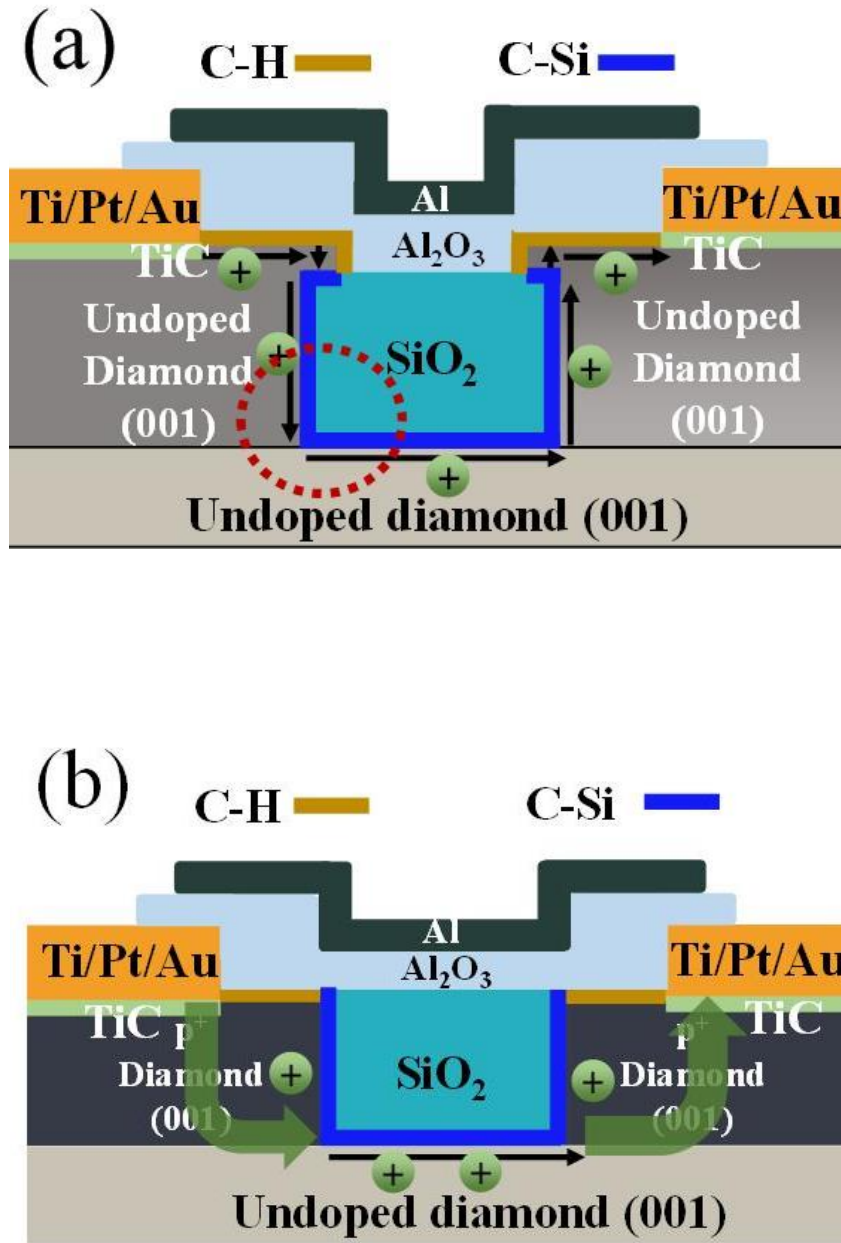


Figure 3.7 Schematic diagram of carrier path in C-Si MOSFET (a) with undoped S/D layer (Device A) and (b) with p⁺ S/D layer (Device B).

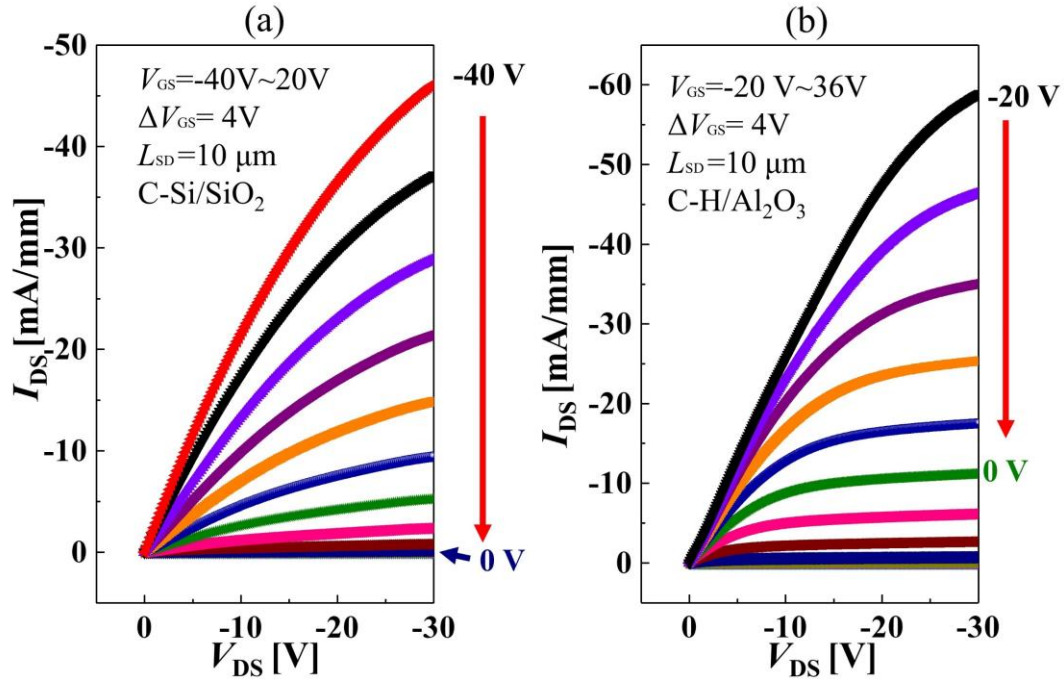


Figure 3.8 I-V characteristics of (a) C-Si diamond /SiO₂ MOSFET proposed in manuscript with effective channel length $L_{SD} = 10 \mu\text{m}$, and (b) C-H diamond /Al₂O₃ (200nm) MOSFET with same sizes as (a).

The values of I_{DS} and transconductance (g_m) for Device B are as large as those of advanced C-H diamond MOSFETs at the similar device size such as L_{SD} .²⁸⁻³⁰ In the same L_{SD} , the I_{DS} - V_{DS} characteristics of a Device B has been compared with that of a C-H diamond MOSFET with Al₂O₃ gate insulator as shown in **Figure 3.8**. The I_{DS} and g_m of the Device B are comparable to those of C-H diamond MOSFET, but the Device B exhibits normally-off operation.

In both Device A and B, the original diamond surface under the masking area was composed of C-O bonds before SiO₂ deposition occurred, followed by selective growth using high temperature plasma deposition. The strong surface states existing at the C-O surface^{31,32} prevent the MOS structure from undergoing effective current modulation by

the electric field. However, the hole current is effectively modulated by the gate electric field at (001) channel indicating other chemical bonds exist at the SiO₂/diamond interface under the masking area. The interfacial chemical bonding might be changed by the diamond selective growth process and hydrogen radical treatment.

3.5 The presence of C-Si diamond

3.5.1 TEM and EDS measurement of the diamond/SiO₂ interface

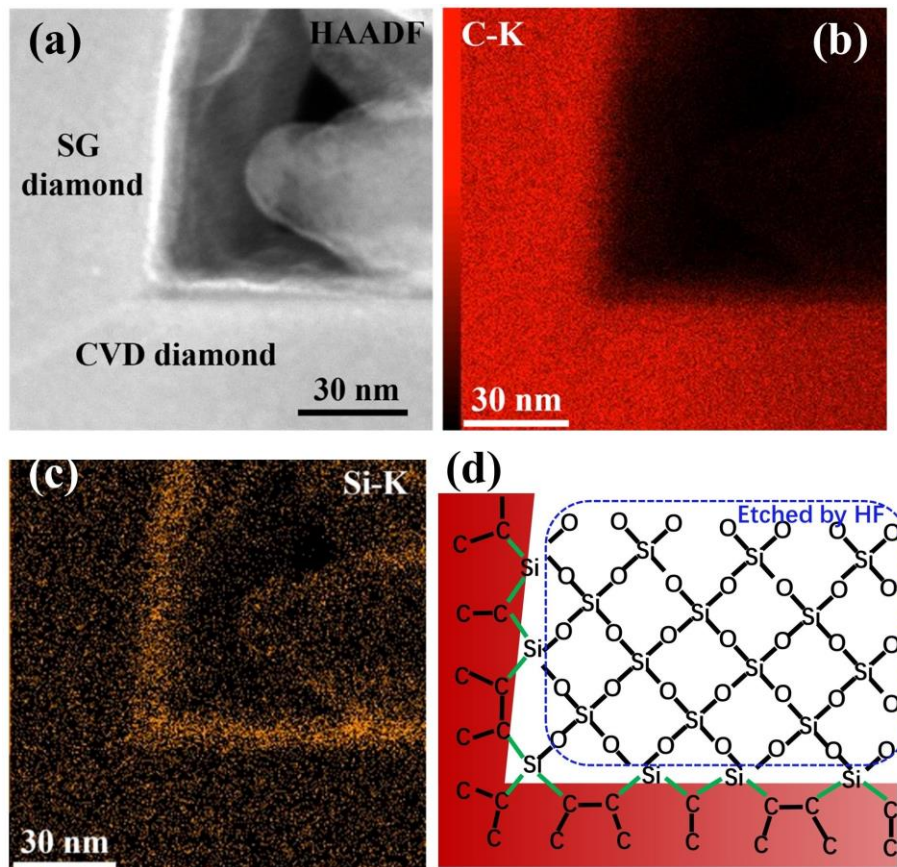


Figure 3.9 The corner of selectively grown (SG) diamond and SiO₂ mask. The SiO₂ has been selectively etched off by HF solution. (a) HAADF image; (b) EDS mapping of C; (c) EDS mapping of remaining Si; (d) schematic diagram of the SiO₂/diamond interface in the masking area after only SiO₂ was chemically removed. C-Si bonds illustrated in green were formed during selective growth.

By performing TEM and EDS measurements, the SiO₂/diamond interface after selective homoepitaxial growth has been analyzed. In order to clarify the interfacial layer, the SiO₂ mask in this area was chemically removed using HF. The results are shown in

Figure 3.9. In the high angle annular dark-field (HAADF) image (**Figure 3.9(a)**), elements with larger atomic number appear brighter. Based on **Figure 3.9(b)**, the bright area in the left part of **Figure 3.9(a)** is confirmed as the area of CVD and selectively grown diamond. A considerably brighter boundary was observed at the interface of the SiO₂/diamond in the masking area. The bright boundary indicates the atoms are heavier than C. In the EDS mapping of Si shown in **Figure 3.9(c)**, the brighter boundary is confirmed as Si. After the sample was treated with HF, SiO₂ on the diamond was completely etched off and C-Si diamond was not dominantly formed, resulting in no Si signal. However, a clear Si signal is observed in **Figure 3.9(c)** even after HF etching, indicating the presence of C-Si bonds. The SiO₂ is etched off by HF, but C-Si bonds are not.

The C-Si diamond formed at high temperature during selective homoepitaxial growth of diamond and H radical treatment. In the secondary ion mass spectrometry (SIMS) profile shown in **Figure 3.10**, the hydrogen concentration at the interface of diamond/SiO₂ was $5 \times 10^{20} \text{ cm}^{-3}$, which is approximately two orders of magnitudes lower than that of the C-H diamond/Al₂O₃ interface.²⁶ The components related to C-Si are clearly recognized in the C1s x-ray photoelectron spectroscopy (XPS) spectrum in **Figure 3.11** and an embedded component of CH_x is due to the hydrocarbon contaminant on the C-Si diamond surface. Based on the above analysis, the C-Si diamond is mainly responsible for the electric field effect performance. A possible formation mechanism of the C-Si diamond is as follows. The thermal energy provided by the selective growth temperature and its reductive atmosphere by hydrogen breaks C-O and Si-O bonds and allows Si atoms to interact with C atoms directly at the SiO₂/diamond interface. Owing to the high reactivity of the unbonded Si, the C-Si diamond is oxidized after the sample is exposed to air from HF

solution, thus remaining on the surface (**Figure 3.9(c) and (d)**). Due to the insufficient resolution of EDX, the presence of a thin multi-layered C-Si bonds might be not excluded. However, the interfacial multi-layer if it exists does not deteriorate the device performance. The influence of the oxidized C-Si diamond on channel conductance and mobility is expected to be comparable to that of C-H diamond exhibiting high field effect performance because of the low surface states density.

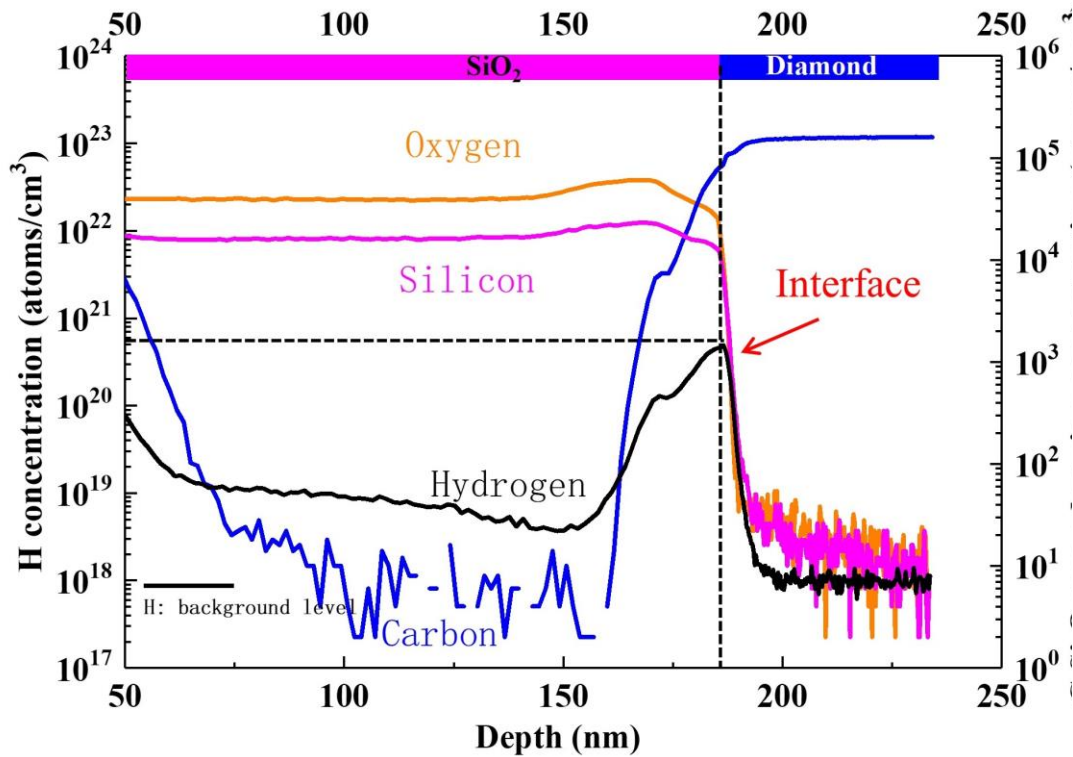


Figure 3.10 Hydrogen depth profile of p^+ CVD process treated diamond with SiO_2 mask investigated by secondary ion mass spectroscopy (SIMS).

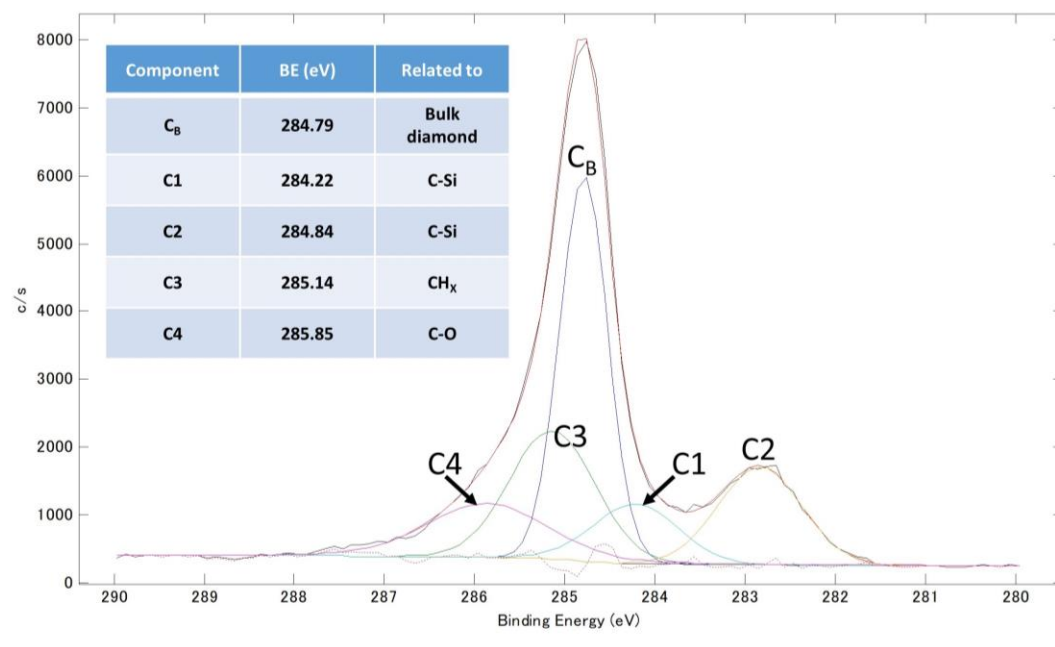


Figure 3.11 C1s XPS spectrum acquired from the p^+ selectively grown diamond surface masked by SiO_2 film. The XPS was performed after SiO_2 removed by HF. C1 and C2 component suggested the C-Si formed at the interface. C3 is related to the CH_x species due to hydrocarbon contaminant absorbed to the diamond surface.

3.5.2 XPS analyses of the diamond/SiO₂ interface

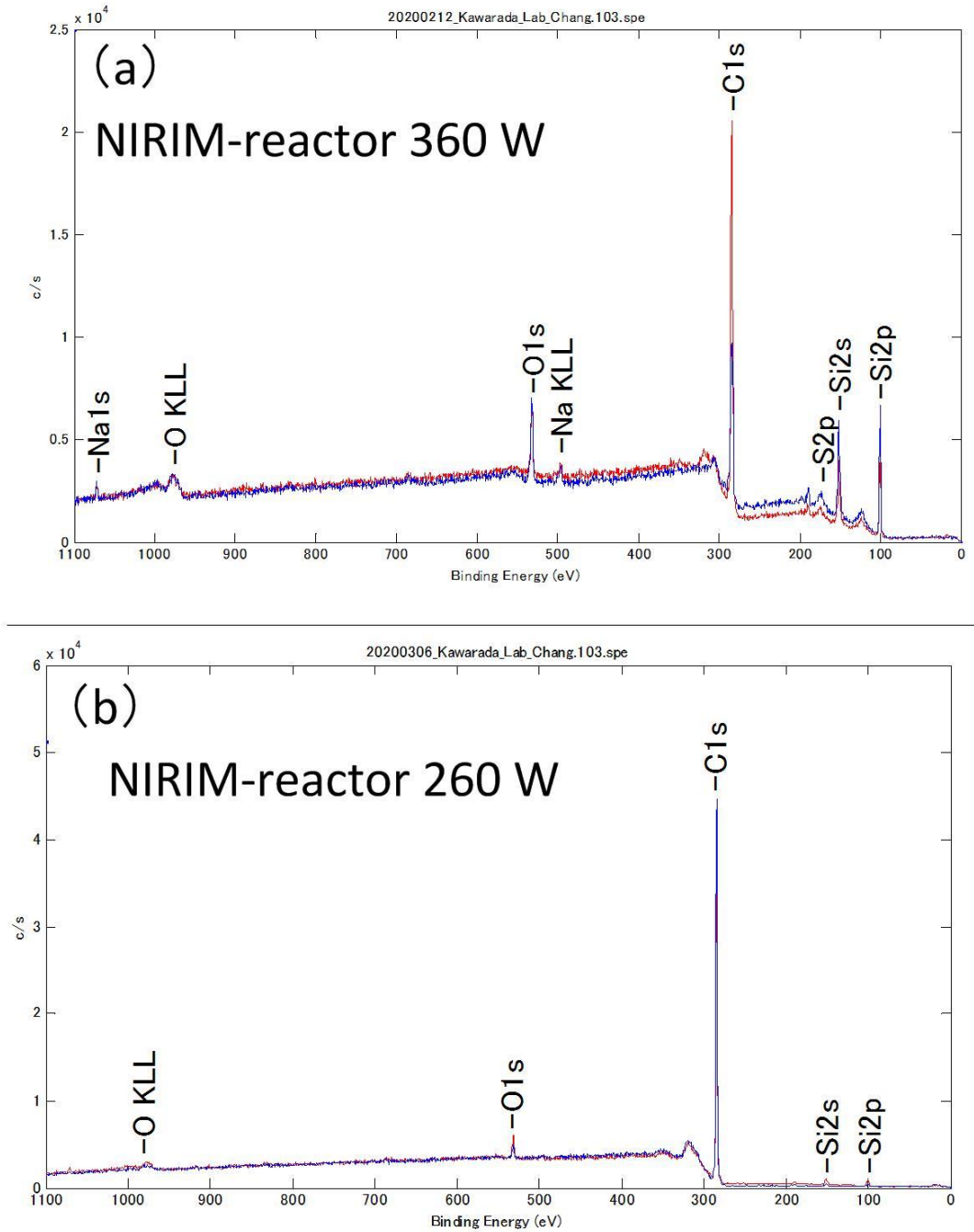


Figure 3.12 wide scan results of the sample treated by NIRIM-type reactor CVD at microwave power of (a) 360 W and (b) 260 W.

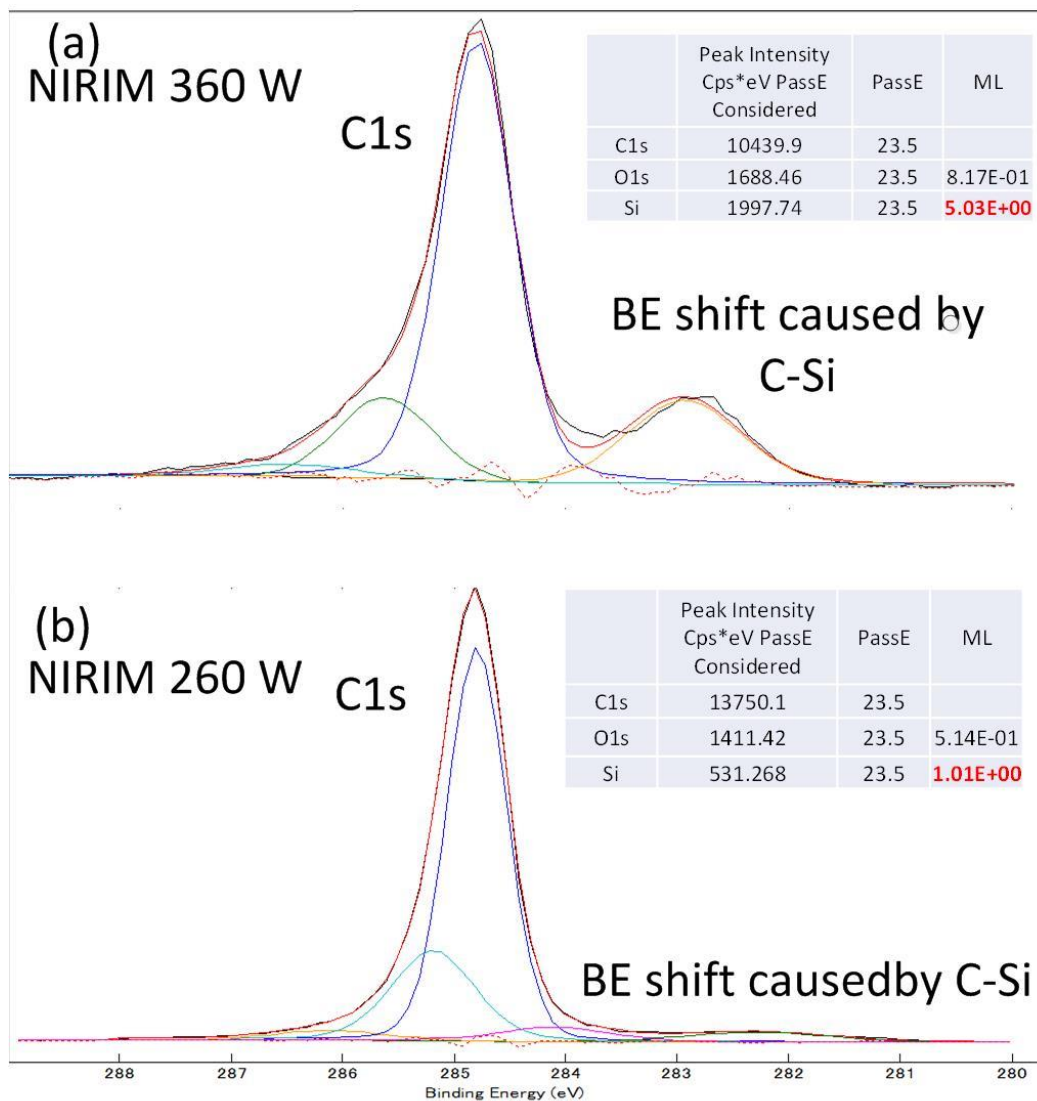


Figure 3.13 narrow scan results of the sample treated by NIRIM-type reactor CVD at microwave power of (a) 360 W and (b) 260 W. The Insets are calculation results of the coverage of Si.

XPS provides useful information for the interface conditions. The undoped diamond covered by 260 nm SiO₂ was treated by the same condition as the device with p⁺ S/D layer in NIRIM reactor CVD. After the CVD process, SiO₂ was removed by HF. To investigate the influence on interface by microwave power, two samples for XPS measurement were fabricated under substrate heated to 740°C and 700°C by microwave power of 360 W and 260 W, respectively. For the excitation source in XPS, a monochromatic Al K α line was used at a power of 24.7 W, the angle of photoelectron detection (θ) was 45°. The wide scan and narrow scan results are demonstrated as **Figure 3.12** and **Figure 3.13**.

The wide scan results are shown in **Figure 3.12**, as the microwave power of CVD process increase, the stronger Si peak is indicative of more silicon reacted with carbon. In the narrow scan results shown in Fig. 3.13, the component of C1s peak in both (a) and (b) shifting to lower energy are indicative of the formation of C-Si.¹⁰ According to the result of silicon coverage calculation, the silicon coverage of the sample obtained at 360 W and 260 W are 5.0 ML and 1.0 ML, respectively. The silicon coverage of the sample obtained at 360 W is in accordance with the EDX results which suggests there are multi-layer of C-Si formed at the SiO₂/diamond interface.

3.6 Field effect mobility and interface states density

The Field effect mobility μ was estimated in Device B using the following equation:

$$\mu_{FE} = \frac{g_m L_{SD}}{(C_{oxide})|V_{DS}|} \quad (\text{Eq. 3.1})$$

where $L_{SD} = 6 \mu\text{m}$. The g_m is derived from the $I_{DS}-V_{DS}$ characteristic (**Figure 3.6(d)**) in the linear region. The maximum g_m is 2.25 mS/mm at $V_{DS} = -10$ V. Capacitance $C_{oxide}^{-1} = C_{SiO_2}^{-1} + C_{Al_2O_3}^{-1}$, where C_{SiO_2} and $C_{Al_2O_3}$ are the capacitances of SiO_2 and Al_2O_3 respectively, $C_{SiO_2} = \frac{\epsilon_0 \cdot \epsilon_{SiO_2}}{d_{SiO_2}}$ where ϵ_0 , ϵ_{SiO_2} , d_{SiO_2} are vacuum permittivity, relative permittivity of SiO_2 (3.9)³³ and thickness of SiO_2 (220 nm) respectively. Similarly, $C_{Al_2O_3}$ is given by $C_{Al_2O_3} = \frac{\epsilon_0 \cdot \epsilon_{Al_2O_3}}{d_{Al_2O_3}}$, where $\epsilon_{Al_2O_3}$ is the relative permittivity of Al_2O_3 (8.9)³⁴, resulting in $C_{oxide} = 1.3 \times 10^{-8}$ F cm^{-2} . Hence, field effect mobility μ_{FE} is $102 \text{ cm}^2 \cdot \text{V}^{-1} \cdot \text{s}^{-1}$.

Interface state density D_{it} is an important factor in evaluating the stability of MOSFET operation. The transfer characteristic of Device B (**Figure 3.6(f)**) was used to calculate D_{it} of the C-Si/ SiO_2 / Al_2O_3 MOS capacitor. The subthreshold swing (SS) was calculated from the change in V_{GS} when I_{DS} decreases by a factor of 10 from 10^{-6} mA/mm, giving $SS = 3400$ mV/decade. D_{it} of the C-Si/ SiO_2 / Al_2O_3 MOS capacitor is determined from:

$$SS = \frac{kT}{q} \ln 10 \left(1 + \frac{C_d + q^2 D_{it}}{C_{oxide}} \right) \quad (\text{Eq. 3.2})$$

where k , T , q , C_d , and C_{oxide} are Boltzmann's constant, RT, elementary charge, the capacitance of the depletion layer, and the series capacitance of the planar Al_2O_3/SiO_2 capacitor respectively. Solving for D_{it} of the C-Si/ SiO_2 / Al_2O_3 MOS structure gives $4.6 \times$

$10^{12} \text{ eV}^{-1}\text{cm}^{-2}$, which is comparable to D_{it} of C-H planar MOSFETs.^{35,36} This indicates that the C-Si/SiO₂/Al₂O₃ capacitor performs stable MOSFET operation.

3.7 Conclusion

C-Si diamond MOSFETs with undoped and heavily boron doped (p^+) S/D layers were fabricated. MOSFET operation has been obtained with undoped S/D selectively grown by an SiO₂ mask, but performance is poorer than that of lateral C-H diamond FETs. This is because the vertical C-Si diamond surface cannot be effectively modulated by the gate voltage. The p^+ S/D decreases contact resistivity, so I_{DS} is increased by a factor of 10 compared to the undoped S/D and equivalent to those of advanced C-H diamond FETS. D_{it} and μ of the C-Si/SiO₂/Al₂O₃ capacitor were shown to be comparable to C-H/Al₂O₃ capacitors, suggesting the C-Si channel is successfully controlled by the field effect. The C-Si diamond MOSFET fabricated by the proposed method is unique and irreplaceable. There are two reasons why the proposed method is irreplaceable. Firstly, it is difficult to form C-Si interface without destroying the sp^3 structure of diamond. C-Si interface cannot be form unless under the high temperature and reductive atmosphere. The CH₄+H₂ plasma under high temperature is capable to protect the diamond surface as it is the diamond epitaxial growth condition. It is possible to form C-Si under pure H₂ high temperature plasma. However, CH₄ is critical for maintaining the diamond structure and repairing the diamond/SiO₂ interface. Therefore, the epitaxial condition is regarded as a suitable for C-Si formation. Secondly, diamond FET with low on-resistance fabricated by ion implantation remains challenging. Nevertheless, the on-resistance can be reduced by 1~2 order of magnitudes by selective growth of p^+ diamond. In a word, as a process that can

realize C-Si interface and low on-resistance, selective growth of p^+ diamond is concise and effective.

References

- ¹ H. Kawarada, Surf. Sci. Rep. **26**, 205 (1996).
- ² M. Tachiki, H. Seo, T. Banno, Y. Sumikawa, H. Umezawa, and H. Kawarada, Appl. Phys. Lett. **81**, 2854 (2002).
- ³ K. Hirabayashi and Y. Hirose, Diam. Relat. Mater. **5**, 48 (1996).
- ⁴ H. Looi, L. Pang, A. Molloy, F. Jones, J. Foord, and R. Jackman, Diam. Relat. Mater. **7**, 550 (1998).
- ⁵ K. Tsugawa, K. Kitatani, H. Noda, A. Hokazono, K. Hirose, M. Tajima, and H. Kawarada, Diam. Relat. Mater. **8**, 927 (1999).
- ⁶ K. Hirama, H. Sato, Y. Harada, H. Yamamoto, and M. Kasu, Jpn. J. Appl. Phys. **51**, 090112 (2012).
- ⁷ H. Kawarada, T. Yamada, D. Xu, H. Tsuboi, T. Saito, and A. Hiraiwa, presented at the 2014 IEEE International Electron Devices Meeting, (2014).
- ⁸ Y. Kitabayashi, T. Kudo, H. Tsuboi, T. Yamada, D. Xu, M. Shibata, D. Matsumura, Y. Hayashi, M. Syamsul, M. Inaba, A. Hiraiwa, and H. Kawarada, IEEE Electron Device Lett. **38**, 363 (2017).
- ⁹ K. Hirama, H. Takayanagi, S. Yamauchi, J. Yang, H. Kawarada, and H. Umezawa, Appl. Phys. Lett. **92**, 112107 (2008).
- ¹⁰ A. Schenk, A. Tadich, M. Sear, K. M. O'Donnell, L. Ley, A. Stacey, and C. Pakes, Appl. Phys. Lett. **106**, 191603 (2015).
- ¹¹ A. Schenk, A. Tadich, M. Sear, D. Qi, A. Wee, A. Stacey, and C. Pakes, Nanotechnology **27**, 275201 (2016).

- ¹² M. J. Sear, A. K. Schenk, A. Tadich, A. Stacey, and C. I. Pakes, *Appl. Phys. Lett.* **110**, 011605 (2017).
- ¹³ M. Geis, J. Gregory, and B. Pate, *IEEE Transactions on Electron Devices* **38**, 619 (1991).
- ¹⁴ S. A. Russell, L. Cao, D. Qi, A. Tallaire, K. G. Crawford, A. T. Wee, and D. A. Moran, *Appl. Phys. Lett.* **103**, 202112 (2013).
- ¹⁵ H. Umezawa, K. Hirama, T. Arai, H. Hata, H. Takayanagi, T. Koshiha, K. Yohara, S. Mejima, M. Satoh, K.-S. Song, and H. Kawarada, *Jpn. J. Appl. Phys.* **44**, 7789 (2005).
- ¹⁶ J. W. Liu, M. Y. Liao, M. Imura, H. Oosato, E. Watanabe, and Y. Koide, *Appl. Phys. Lett.* **102**, 112910 (2013).
- ¹⁷ T. Suwa, T. Iwasaki, K. Sato, H. Kato, T. Makino, M. Ogura, D. Takeuchi, S. Yamasaki, and M. Hatano, *IEEE Electron Device Lett.* **37**, 209 (2015).
- ¹⁸ T. Matsumoto, H. Kato, K. Oyama, T. Makino, M. Ogura, D. Takeuchi, T. Inokuma, N. Tokuda, and S. Yamasaki, *Sci. Rep.* **6**, 31585 (2016).
- ¹⁹ J. Liu, H. Oosato, M. Liao, and Y. Koide, *Appl. Phys. Lett.* **110**, 203502 (2017).
- ²⁰ N. Oi, T. Kudo, M. Inaba, S. Okubo, S. Onoda, A. Hiraiwa, and H. Kawarada, *IEEE Electron Device Lett.* **40**, 933 (2019).
- ²¹ W. Fei, M. Inaba, H. Hoshino, I. Tsuyusaki, S. Kawai, M. Iwataki, and H. Kawarada, *Phys. Status Solidi A* **216**, 1900227 (2019).
- ²² Y. Jingu, K. Hirama, and H. Kawarada, *IEEE transactions on electron devices* **57**, 966 (2010).
- ²³ J. Nakanishi, A. Otsuki, T. Oku, O. Ishiwata, and M. Murakami, *J. Appl. Phys.* **76**, 2293 (1994).

- ²⁴ M. Inaba, T. Muta, M. Kobayashi, T. Saito, M. Shibata, D. Matsumura, T. Kudo, A. Hiraiwa, and H. Kawarada, *Appl. Phys. Lett.* **109**, 033503 (2016).
- ²⁵ A. Hiraiwa, A. Daicho, S. Kurihara, Y. Yokoyama, and H. Kawarada, *J. Appl. Phys.* **112**, 124504 (2012).
- ²⁶ A. Daicho, T. Saito, S. Kurihara, A. Hiraiwa, and H. Kawarada, *J. Appl. Phys.* **115**, 223711 (2014).
- ²⁷ J. Liou, A. Ortiz-Condez, and F. G. Sanchez, presented at the 1997 IEEE Hong Kong Proceedings Electron Devices Meeting, (1997).
- ²⁸ H. Kawarada, *Jpn. J. Appl. Phys.* **51**, 090111 (2012).
- ²⁹ Y. Fu, R. Xu, Y. Xu, J. Zhou, Q. Wu, Y. Kong, Y. Zhang, T. Chen, and B. Yan, *IEEE Electron Device Lett.* **39**, 1704 (2018).
- ³⁰ X. Yu, J. Zhou, S. Zhang, Z. Cao, Y. Kong, and T. Chen, *Appl. Phys. Lett.* **115**, 192102 (2019).
- ³¹ S. Sque, R. Jones, and P. Briddon, *Physical review B* **73**, 085313 (2006).
- ³² K. M. O'Donnell, T. L. Martin, and N. L. Allan, *Chemistry of Materials* **27**, 1306 (2015).
- ³³ G. C. Schwartz, Y. S. Huang, and W. J. Patrick, *Journal of the Electrochemical Society* **139**, L118 (1992).
- ³⁴ A. Hiraiwa, D. Matsumura, and H. Kawarada, *J. Appl. Phys.* **120**, 084504 (2016).
- ³⁵ J. Liu, H. Ohsato, X. Wang, M. Liao, and Y. Koide, *Sci. Rep.* **6**, 34757 (2016).
- ³⁶ N. C. Saha and M. Kasu, *Diam. Relat. Mater.* **91**, 219 (2019).

Chapter IV Initial local epitaxial growth of diamond (111) on Ru (0001)//c- sapphire by antenna-edge-type microwave plasma chemical vapor deposition

Heteroepitaxial growth is critical for the large-scale synthesis of diamond (111) substrates. In this study, the initial local epitaxial growth of diamond (111) on Ru/c-sapphire was investigated. As Ru is a more economically viable option to Ir, a 150-nm Ru (0001) thin film was sputter-deposited on an Al₂O₃ (0001) substrate by a RF/DC magnetron sputtering system. X-ray diffraction analyses of the Ru film revealed the (0001) phase orientation with high crystalline quality. Bias enhanced nucleation and (111) preferential growth were both performed by antenna-edge-type microwave plasma-assisted chemical vapor deposition. After 30 min of preferential growth, the crystallite (diameter ~500 nm) with a smooth surface was observed through scanning electron microscopy. The electron backscattering diffraction (EBSD) orientation mapping indicated the presence of the highly

orientated diamond (111) crystallite. The EBSD pole-figure pattern represented the formation of a double positioning defect. Heteroepitaxial growth of diamond (111) on ruthenium provides a more economically viable approach to fabricate large vertical channel diamond MOSFET or GaN-on-diamond power electronics.

4.1 Heteroepitaxial growth of diamond

The (111)-oriented diamond shows advantages over other crystal surfaces in diamond-based electronic devices. The diamond (111) is desirable for high-current and high-frequency operation due to its higher hydrogen termination density.¹⁻³ Vertical-type diamond metal-oxide-semiconductor field-effect transistors (MOSFETs) exhibit coexistence of high current as well as high breakdown voltage operation.⁴⁻⁶ The fabrication of the aforementioned vertical-type transistor on heteroepitaxial (111) diamond grown on a metal substrate can be simplified, as there is no need for additional metal contacts at the back of the substrate for contact. For the doped diamond, (111)-orientation is beneficial to improve the carrier activation rate at room temperature owing to the highest incorporation efficiency of the dopant.⁷⁻⁹ In addition to the exceptional electronic properties, diamond possess the highest thermal conductivity, making the use of the GaN-on-diamond structure a promising approach to increase the output power density of high electron mobility transistors (HEMTs).¹⁰⁻¹² GaN HEMTs with remarkable operation have been realized using diamond as a heat spreader.¹³⁻¹⁶ However, homoepitaxial diamond (111) is limited in size and is costly as well as facilitates the easy formation of crystallite defects through twinning¹⁷ and promotes poor crystalline quality compared to (100).¹⁸ Thus, the heteroepitaxial

growth of diamond (111), which is not limited by the substrate size, is critical for its intended device applications.

Up till now, considerable efforts have been devoted to the preparation of diamond (111) on platinum-group substrates such as iridium,¹⁹⁻²² platinum,^{23,24} and rhenium.²⁵ However, the heteroepitaxial growth of diamond on a ruthenium substrate has never been reported yet. Ruthenium has properties similar to those of iridium, which has been extensively subjected to diamond heteroepitaxial growth investigation, such as in-plane lattice mismatch for diamond (111) (ruthenium 7.0 %, iridium 7.1 %) and melting point (ruthenium: 2334°C, iridium 2466°C).²¹ The interaction between diamond and iridium is considered crucial for the successful heteroepitaxial growth rather than the lattice mismatch and thermal expansion coefficient. The interaction between ruthenium and diamond has not been reported yet. However, previous studies have confirmed that graphene nucleation on Ru (0001) is caused because of the interaction of the carbon species with the atomic ruthenium terrace²⁶⁻²⁸, and the hexagonal structure of ruthenium is indicative of the possibility that it can be used as a deposition substrate for (111)-orientated diamonds. Moreover, the lowest price (only a quarter of iridium's current market price) in the platinum group makes the use of ruthenium economical in industrial applications, thus serving as a promising cost-effective candidate for application in the preparation of large-size single diamond substrates.

We demonstrate, here, the single crystal ruthenium thin film grown on an Al₂O₃ (0001) (c-sapphire) substrate provides the most economically viable solution as the platinum group substrate for nucleation and initial growth of diamond (111). The ruthenium film was sputtered on c-sapphire by magnetron sputtering, showed as single

crystal (0001)-orientated by X-ray diffraction (XRD) measurements. A two-step process composed of bias enhanced nucleation (BEN) and (111) preferential growth was performed in the antenna-edge-type microwave plasma-assisted chemical vapor deposition apparatus. The nuclei grown on the ruthenium film were characterized by scanning electron microscopy (SEM) and electron backscattering diffraction (EBSD). These nuclei were confirmed to be (111)-orientated diamond

4.2 Experimental process

As ruthenium single crystals are not available, thin films need to be deposited on other bulk substrates. Commercially available (MTI Corp., CA, US) c-sapphire with dimensions of $5 \times 5 \times 0.5$ mm was soaked in acetone in an ultrasonic bath to remove the organic impurities. Then, a 150 nm-thick ruthenium film was deposited on c-sapphire by a magnetron sputtering deposition system (Denton Vacuum Inc., NJ, USA) equipped with both DC and RF sputter power. The deposition was carried out using the DC bias for nucleation and the RF sputtering in Ar atmosphere. The summary of the experimental parameters which have been adopted for optimization of ruthenium sputtering deposition are concluded in Table 4.2, among them, only #7 and # 8 were effective for Ru (0001) deposition, so this condition was used to prepare the highly-orientated ruthenium film for diamond growth. The cross-sectional SEM image of ruthenium film after deposition is shown in **Figure 4.1**. The deposition rate of #8 is about 0.95 nm/min.

It is necessary to make the substrate electrically connected to the holder before the BEN process. The sputtering target was positioned at 45° to the substrate, so that the four

substrate sides were coated with the ruthenium film after the deposition. The Au contacts were deposited at the back of the substrate by e-beam evaporation. The heteroepitaxial diamond is grown by the two-step process: BEN and $\langle 111 \rangle$ preferential growth. The BEN process was carried out by antenna-edge-type microwave-plasma chemical-vapor deposition (MPCVD, Arios, spherical resonant cavity type) for 30s with methane concentration of 10 % at 650 °C, the subsequent $\langle 111 \rangle$ growth was carried out locally for 30 min with 0.3 % methane at 600°C. The DC voltage of -150 V for BEN was applied to the apparatus by connecting the cathode of the DC power supplier to the antenna, while the anode was connected to the substrate holder, which was made of Mo and was grounded. Details of the experimental parameters of the entire process are summarized in Table I. As there was no nucleus observed even the parameters were altered slightly. It is likely that BEN can be achieved only within a very narrow range of parameters. Notably, when the growth time exceeds 30 minutes, severely damage the ruthenium film is likely to be severely damage or even peel off from the diamond substrate. The damage is associated with the abnormal heat load caused by the ion bombardment.²⁹ In consideration of the growth condition is within a quite narrow range, buffer layer introduced between diamond substrate and ruthenium film could be a promising solution. The morphology and crystallographic characterization were investigated by SEM and EBSD.

Table 4.1 Experimental parameters of Ru sputter-deposition on c-sapphire and (111) diamond heteroepitaxial growth using two-step process.

Parameters	Ru sputter-deposition		Diamond growth	
	DC bias nucleation	RF magnetron sputtering	BEN	<111> growth
Substrate temperature (°C)	600	600	650	600
Bias voltage (V)	-50	-	-150	-
Microwave Power (W)	-	50	120	120
H ₂ (sccm)	-	-	90	199.4
CH ₄ (sccm)	-	-	10 (10 %)	0.6 (0.3 %)
Ar (sccm)	20	20	-	-
Process time (s)	1200	9600	30	1800

Table 4.2 summary of experimental parameters had been adopted to optimization of the Ru sputtering deposition on c-sapphire

#	Substrate temperature (°C)	DC bias voltage (V)	Process Time (s)	RF output power (W)	Substrate temperature(°C)	Process time (s)	Ru peaks in XRD?
1	600	-	600	50	600	3200	N
2	600	-150	300	50	600	3200	faint
3	RT	-	600	50	RT	3200	N
4	600	150	300	50	600	3200	faint
5	600	50	600	50	600	3200	faint
6	350	50	600	50	600	3200	No
7	600	50	1200	50	600	3200	Y
8	600	50	1200	50	600	9600	Y

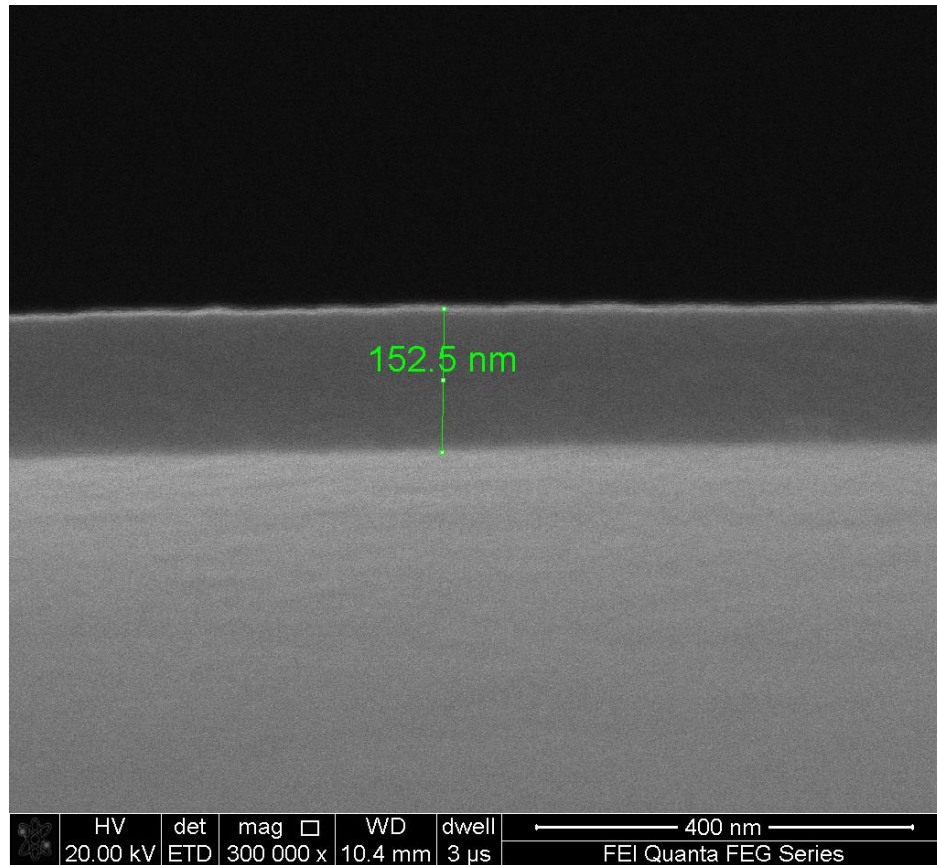


Figure 4.1 Cross-sectional SEM image of ruthenium film deposited on c-sapphire by condition #8 in Table 4.2. the thickness of ruthenium film deposited for 9600s is 152.5 nm, the deposition rate of the #8 is about 0.95 nm/min.

4.3 Crystallographic characterization of ruthenium on c-sapphire

Table 4.3 Diffraction data of ruthenium ($2\theta < 100^\circ$), Cu radiation

#	2θ	d	I(f)	(hkl)	θ	$1/(2d)$	$2\pi/d$
1	38.387	2.3430	40.0	(100)	19.193	0.2134	2.6817
2	42.152	2.1420	35.0	(002)	21.076	0.2334	2.9333
3	44.005	2.0560	100.0	(101)	22.003	0.2432	3.0560
4	58.323	1.5808	25.0	(102)	29.161	0.3163	3.9747
5	69.405	1.3530	25.0	(110)	34.702	0.3695	4.6439
6	78.388	1.2189	25.0	(103)	39.194	0.4102	5.1548
7	82.221	1.1715	6.0	(200)	41.111	0.4268	5.3634
8	84.703	1.1434	25.0	(112)	42.351	0.4373	5.4952
9	85.957	1.1299	20.0	(201)	42.979	0.4425	5.5608
10	92.035	1.0705	4.0	(004)	46.017	0.4671	5.8694
11	97.085	1.0278	8.0	(202)	48.542	0.4865	6.1132

Data highlighted in yellow are the diffraction data of Ru (0001) ($2\theta < 100^\circ$)

Highly oriented Ru (0001) was successfully deposited on c-sapphire, as is evident from XRD. The diffraction data of ruthenium ($2\theta < 100^\circ$) can be seen in Table 4.3, data highlighted in yellow are the diffraction data of Ru (0001). From the XRD, the diffraction pattern in **Figure 1(a)** has four peaks at 41.7° , 42.2° , 90.7° and 92.0° , corresponding to Al_2O_3 (0006), Ru (0002), Al_2O_3 (00012) and Ru (0004), respectively. No diffraction peaks of other planes except the (0001) suggests the Ru film is single crystal with (0001) orientation. The periodicity of the diffraction peaks localized every 60° in ϕ -scan [**Figure 4.2(b)**] indicates the highly orientated $(10\bar{1}1)$ Ru with six-fold symmetry. **Figure 1(c)** displays the full width at half maximum (FWHM) of ω -scan (rocking curve) of (0002)

diffraction with a value 1.1° . Considering the relatively thin thickness of ruthenium film, the value of FWHM is reasonable.

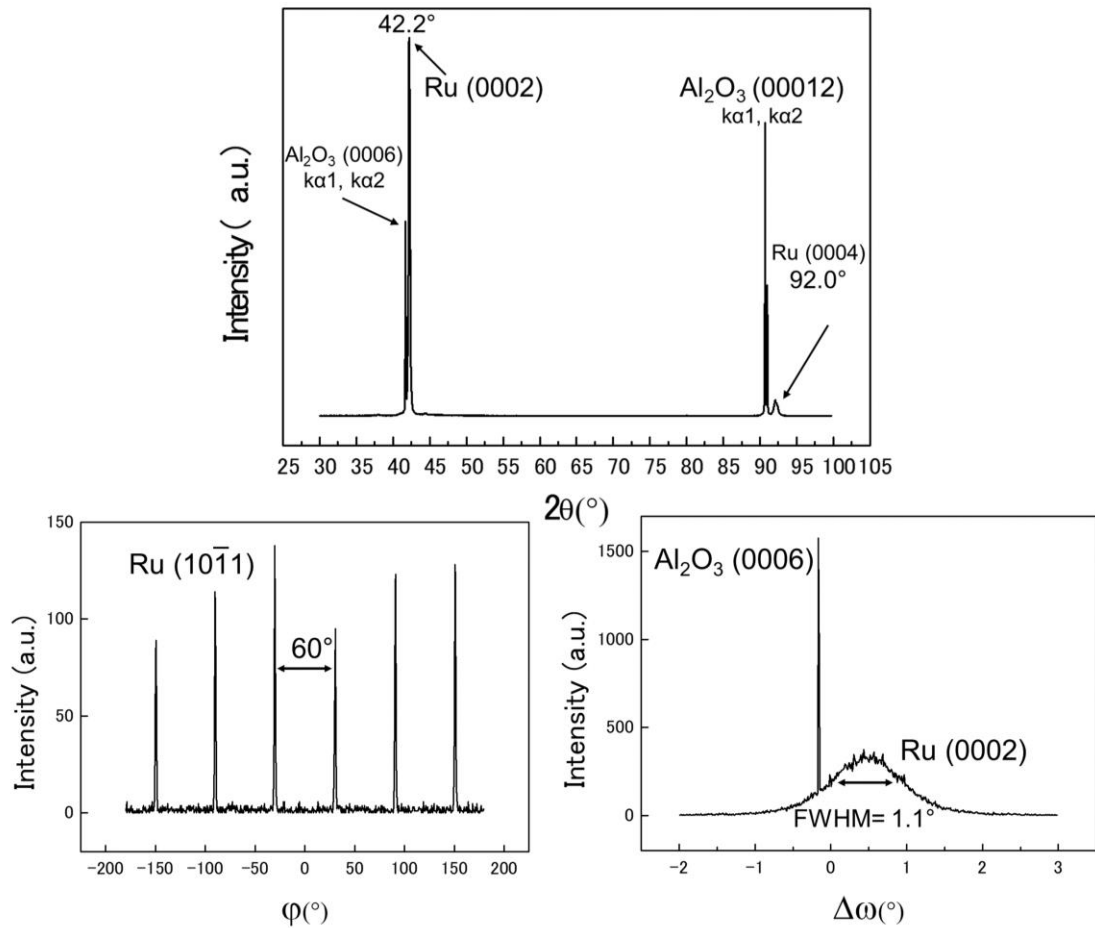


Figure 4.2 X-ray diffraction of Ru (0001) film deposited on c-sapphire. (a) θ - 2θ scan, $\kappa\alpha$ double in peak of Al_2O_3 were observed due to the Cu polychromatic x-ray source. (b) ϕ -scan for (10 $\bar{1}$ 1) diffraction measured at a polar angle $\chi = 61.9^\circ$ and (c) ω -scan (rocking curve)

4.4 Morphologies of diamond (111) on Ru (0001)//c-sapphire

Figure 4.3 shows the morphologies of the crystallites formed after 30 min of local heteroepitaxial growth of diamond on Ru (0001)/c-sapphire. Several (111)-orientated crystallites with faintly visible incomplete hexagonal outline show clear lateral growth in the same angle. This phenomenon may be explained by the formation of the (111) plane twinning crystal, and the orientation of one of the twinning is preferable to that of another one. The inset shows the crystallite with a clear (111) surface. The average diameter of the crystallites is approximately 500 nm.

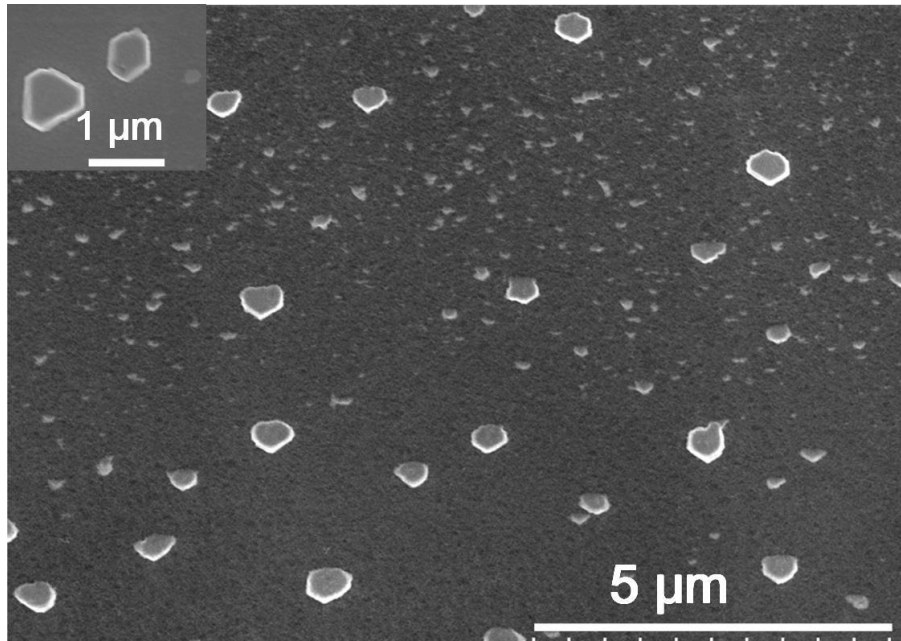


Figure 4.3 SEM image of crystallites formed on Ru film by the 30s BEN and 30 minutes $\langle 111 \rangle$ growth by antenna-type microwave plasma-assisted CVD. Inset shows the 111-faceted crystallite without twinning defect.

4.5 Crystallographic characterization of diamond on Ru

(0001)/c-sapphire

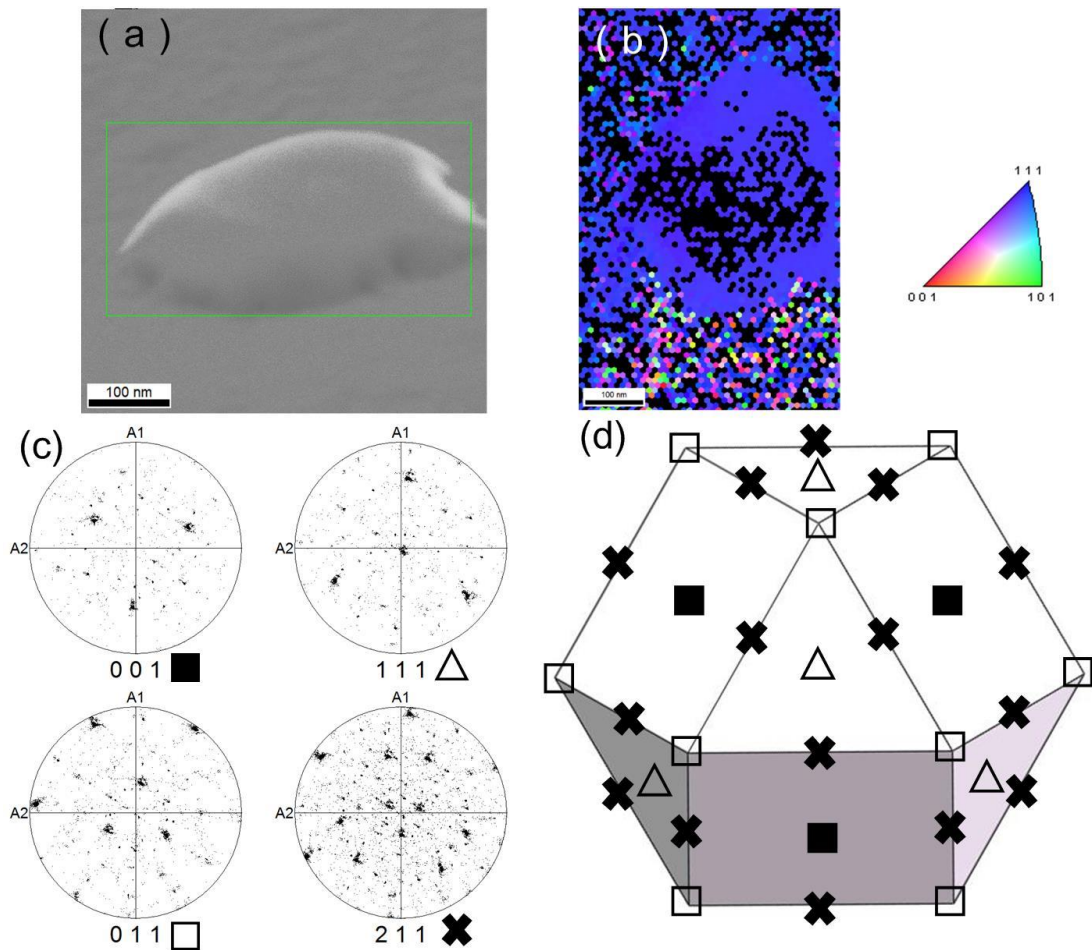


Figure 4.4 (a) 45°-tilting top view SEM image of the crystallite. (b) Inverse pole figure (IPF) of diamond and the color key. (c) The pole figure of (001), (111), (011), and (211), respectively. (d) 3D schematics of the diamond crystallite showing the well-faceted cuboctahedron composed of (111) and (001) planes.

The SEM image of the nucleus with a smooth surface of crystallite A was taken with the substrate tilted 45° [Figure 4.4(a)]. The inverse pole figure (IPF) of the diamond (mapped at the green square in (a) from top-view) and the corresponding color key indicate that the (111)-orientated diamond dominates the crystallites. Based on the EBSD pattern of (001), (111), (011), and (211), the 3D schematic of the crystallite can be illustrated as a well-faceted cuboctahedron of diamond developed of (111) and (100) facets [Figure 4.4(d)]. In the cuboctahedron, the triangular faces and the square faces are equivalent (111) and (100) facets, respectively. In Figure 4.4(d), the diffraction of the (011) is denoted as the vertices of the triangle and the square faces. While the (211) planes are denoted as the midpoint of the edges, the assignment of the planes is as per the pole distribution in Figure 4.4(c).

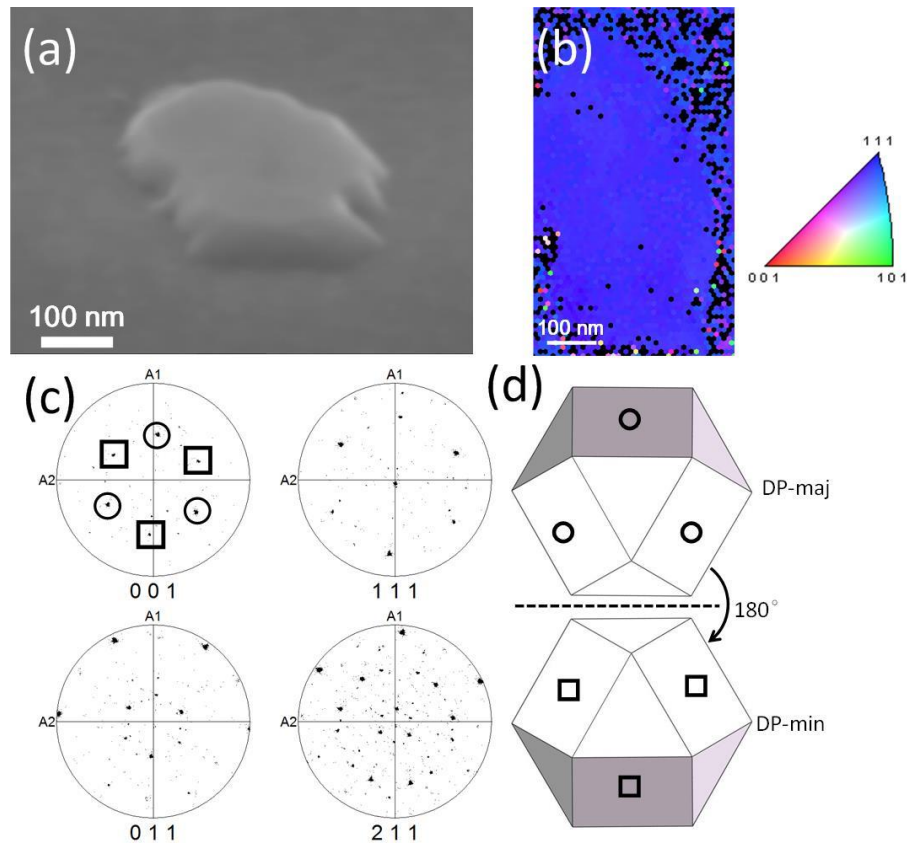


Figure 4.5 Crystallographic characterization of grain B. (a) SEM image, (b) IPF of diamond and the color key, (c) the pole figure of (001), (111), (011), and (211), respectively. (d) Schematics of the arrangement of DP-maj and DP-min.

Figure 4.5 (b) is the IPF of diamond mapped at the green square in crystallite labeled (crystallite B) observed by SEM (**Figure 4.5(a)**). Crystallite B was identified as the highly orientated (111) diamond by the IPF, which shares the same color key with **Figure 4.4(b)**. Crystallite B consists of two cuboctahedrons [as in **Figure 4.4(d)**] twining crystal called double positionings (DPs), which are rotated by 180° in-plane relative to each other. Because two alternative three-fold symmetrical crystallographic configurations are allowed during the nucleation, DPs are frequently observed when a (111)-oriented face-centered-cubic crystal with three-fold symmetry is grown on the basal plane of hexagonal crystal with six-fold symmetry.³⁰⁻³² In crystallite B, one phase of the DPs gives a stronger projection signal in the pole figure [**Figure 4.5(c)**] and is labeled ‘DP-maj,’ another gives a weak signal, which is labeled as ‘DP-min.’ The DP-maj is preferable to the DP-min with the other three orientations, which agrees with the incomplete hexagonal crystallite having the same orientation observed in **Figure 4.3**. The DPs did not stop at the (111) plane but propagate to the other adjacent (100) and (111) planes in the crystallite. Therefore, in the pole figures of (001), except for three orientations from the DP-maj, which are the same as the pole distribution in **Figure 4.4(c)**, there is an additional set of poles of DP-min rotated 180° relative to those of DP-maj. Two sets of orientation generated by DPs can also be found in the other three-pole figures of (111), (011), and (211). Suppression of the DP defect formed in the 3C-SiC epitaxial film by using an off-axis substrate or a surface cleaning method has been reported,^{31,33} and can be applied to reduce the formation of DP in heteroepitaxial diamond on ruthenium. Additionally, except the characteristic pattern of well-crystallized planes in the pole figure, there are some random projection spots observed,

indicating there are non-epitaxial amorphous carbon existing in the crystallites. Accordingly, based on the SEM and crystallographic analyses, the Ru (0001) film is an ideal substrate for diamond (111). After BEN and 30 min of growth under proper condition, single-crystal diamond or DP crystallite with (111) orientation was obtained. The expansion on the lateral size indicated that as the processing time of growth was extended, a continuous diamond film is expected to be formed.

4.6 Conclusion

In conclusion, here, we demonstrated the initial local epitaxial growth of diamond (111) on Ru (0001)/c-sapphire by antenna-edge-type MPCVD. A single-crystal Ru (0001) film was sputter-deposited on c-sapphire and investigated by DC/RF magnetron sputtering and XRD, respectively. The heteroepitaxial growth of diamond involved of two-step processes: BEN and $\langle 111 \rangle$ preferential growth. The crystallites after 30 min of growth were investigated by SEM and EBSD. The diamond crystallites with a smooth surface have an average diameter of approximately 500 nm, with a clear or double positioning twin (111) surface and propagate to other adjunct planes. The heteroepitaxial growth of diamond on a ruthenium film facilitates the economically viable preparation of large size (111) diamond. Unfortunately, we are not a specializing team in heterogeneous epitaxial of diamond, so the techniques and equipment we have are quite limited. If this work is continued by a highly-experienced group to grow the highly-oriented, it is extremely promising to realize large-size continuous diamond thin films or even substrates.

References

- ¹ M. Kasu, M. Kubovic, A. Aleksov, N. Teofilov, R. Sauer, E. Kohn, and T. Makimoto, *Jpn. J. Appl. Phys.* **43**, L975 (2004).
- ² K. Hirama, H. Takayanagi, S. Yamauchi, J. Yang, H. Kawarada, and H. Umezawa, *Appl. Phys. Lett.* **92**, 112107 (2008).
- ³ K. Hirama, K. Tsuge, S. Sato, T. Tsuno, Y. Jingu, S. Yamauchi, and H. Kawarada, *Applied physics express* **3**, 044001 (2010).
- ⁴ M. Inaba, T. Muta, M. Kobayashi, T. Saito, M. Shibata, D. Matsumura, T. Kudo, A. Hiraiwa, and H. Kawarada, *Appl. Phys. Lett.* **109**, 033503 (2016).
- ⁵ N. Oi, M. Inaba, S. Okubo, I. Tsuyuzaki, T. Kageura, S. Onoda, A. Hiraiwa, and H. Kawarada, *Sci. Rep.* **8**, 1 (2018).
- ⁶ M. Iwataki, N. Oi, K. Horikawa, S. Amano, J. Nishimura, T. Kageura, M. Inaba, A. Hiraiwa, and H. Kawarada, *IEEE Electron Device Lett.* **41**, 111 (2019).
- ⁷ D. Araujo, A. Tajani, E. Gheeraert, and E. Bustarret, *Journal of Physics: Condensed Matter* **16**, S287 (2003).
- ⁸ T. Saito, K.-h. Park, K. Hirama, H. Umezawa, M. Satoh, H. Kawarada, Z.-Q. Liu, K. Mitsuishi, K. Furuya, and H. Okushi, *Journal of electronic materials* **40**, 247 (2011).
- ⁹ R. Edgington, S. Sato, Y. Ishiyama, R. Morris, R. B. Jackman, and H. Kawarada, *J. Appl. Phys.* **111**, 033710 (2012).
- ¹⁰ J. G. Felbinger, M. Chandra, Y. Sun, L. F. Eastman, J. Wasserbauer, F. Faili, D. Babic, D. Francis, and F. Ejeckam, *IEEE Electron Device Lett.* **28**, 948 (2007).
- ¹¹ A. Dussaigne, M. Malinverni, D. Martin, A. Castiglia, and N. Grandjean, *Journal of crystal growth* **311**, 4539 (2009).

- ¹² F. Mu, R. He, and T. Suga, *Scripta Materialia* **150**, 148 (2018).
- ¹³ K. Hiram, M. Kasu, and Y. Taniyasu, *IEEE Electron Device Lett.* **33**, 513 (2012).
- ¹⁴ P. Chao, K. Chu, J. Diaz, C. Creamer, S. Sweetland, R. Kallaher, C. McGray, G. D. Via, and J. Blevins, *MRS Advances* **1**, 147 (2016).
- ¹⁵ T. Ohki, A. Yamada, Y. Minoura, K. Makiyama, J. Kotani, S. Ozaki, M. Sato, N. Okamoto, K. Joshin, and N. Nakamura, *IEEE Electron Device Lett.* **40**, 287 (2018).
- ¹⁶ M. J. Tadjer, T. J. Anderson, M. G. Ancona, P. E. Raad, P. Komarov, T. Bai, J. C. Gallagher, A. D. Koehler, M. S. Goorsky, and D. A. Francis, *IEEE Electron Device Lett.* **40**, 881 (2019).
- ¹⁷ A. Badzian and T. Badzian, *Diam. Relat. Mater.* **2**, 147 (1993).
- ¹⁸ A. Tallaire, J. Achard, A. Boussadi, O. Brinza, A. Gicquel, I. Kupriyanov, Y. Palyanov, G. Sakr, and J. Barjon, *Diam. Relat. Mater.* **41**, 34 (2014).
- ¹⁹ T. Fujisaki, M. Tachiki, N. Taniyama, M. Kudo, and H. Kawarada, *Diam. Relat. Mater.* **11**, 478 (2002).
- ²⁰ T. Fujisaki, M. Tachiki, N. Taniyama, M. Kudo, and H. Kawarada, *Diam. Relat. Mater.* **12**, 246 (2003).
- ²¹ M. Schreck, S. Gsell, R. Brescia, and M. Fischer, *Sci. Rep.* **7**, 1 (2017).
- ²² B.-C. Gallheber, M. Fischer, M. Mayr, J. Straub, and M. Schreck, *J. Appl. Phys.* **123**, 225302 (2018).
- ²³ Y. Shintani, *Journal of materials research* **11**, 2955 (1996).
- ²⁴ T. Tachibana, Y. Yokota, K. Nishimura, K. Miyata, K. Kobashi, and Y. Shintani, *Diam. Relat. Mater.* **5**, 197 (1996).

- ²⁵ T. Bauer, M. Schreck, S. Gsell, F. Hörmann, and B. Stritzker, *Phys. Status Solidi A* **199**, 19 (2003).
- ²⁶ S. Marchini, S. Günther, and J. Wintterlin, *Physical Review B* **76**, 075429 (2007).
- ²⁷ P. W. Sutter, J.-I. Flege, and E. A. Sutter, *Nature materials* **7**, 406 (2008).
- ²⁸ H. Zhang, Q. Fu, Y. Cui, D. Tan, and X. Bao, *The Journal of Physical Chemistry C* **113**, 8296 (2009).
- ²⁹ S. Ohmagari, T. Matsumoto, H. Umezawa, and Y. Mokuno, *Thin Solid Films* **615**, 239 (2016).
- ³⁰ H.-S. Kong, B. Jiang, J. T. Glass, G. Rozgonyi, and K. More, *J. Appl. Phys.* **63**, 2645 (1988).
- ³¹ M. Nakamura, T. Isshiki, T. Nishiguchi, K. Nishio, S. Ohshima, and S. Nishino, presented at the Materials Science Forum, (2005).
- ³² S. Roy, M. Portail, T. Chassagne, J. M. Chauveau, P. Vennéguès, and M. Zielinski, *Appl. Phys. Lett.* **95**, 081903 (2009).
- ³³ T. Kusumori, H. Muto, M. Okada, and P. Jin, *Thin solid films* **513**, 307 (2006).

Chapter V Summary

The previous chapters can be concluded as followings:

1. Functional silicon compatible architecture for robust diamond device: Selective growth of diamond is affected by the deformation of the metal mask, and contamination from the metal will deteriorate the electronic properties of selectively grown diamond. In Chapter II, by point-arc remote MPCVD and reliable SiO₂ mask deposited by plasma CVD (TEOS), the selective growth with a 330-nm diamond layer was selectively grown via four-hour deposition. SiO₂, which is a conventional gate oxide material, exhibits considerable stability to high temperature (850°C), and the reductive atmosphere (99.5% H₂) of diamond CVD growth is expected to improve the robustness of 2DHG diamond electronics. No distortion of the SiO₂ mask and Mo concentration under the detection limit of SIMS measurement indicative of high-quality diamond was selectively grown. **(Physica Status Solidi A, 21 (2019) 1900227/1-6)**

2. C-Si channel for robust 2DHG MOSFET: SiO₂ gate oxide is widely used in Si-based MOSFETs and is known to be more reliable than other oxide materials, such as Al₂O₃, because of its stable chemical bonding structure. Based on the selective growth of undoped single crystal diamond, MOSFETs were fabricated. The SiO₂ mask continued to act as the gate oxide; subsequently, Al₂O₃ passivation and Al gate were deposited. A drain current of -17 mA/mm with a normally-off operation was confirmed. By replacing the

undoped/TiC contact with the p⁺/TiC contact, the drain current of the MOSFET was significantly increased to -165 mA/mm, while maintaining the normally-off operation. The combination of diamond and its conventional reliability makes diamond more desirable for power electronics that require high voltage and high output current. However, further investigation on the surface analysis and C-V measurement of silicon-terminated diamond/SiO₂ is imperative to thoroughly understand the silicon-terminated diamond. (**Applied Physics Letters, 116 (2020) 212103/1-4**)

3. Possibility of larger diamond substrate synthesis: As described in Chapter IV, highly orientated (111) diamond was successfully grown on Ru (0001)/ c-sapphire. The 150-nm ruthenium film sputtering deposition on the c-sapphire substrate showed the possibility of well-crystallized substrate with a (0001) orientation. Diamond crystallites with smooth surfaces on the ruthenium film were observed after a two-step process consisting of bias-enhanced nucleation and <111> CVD growth. Crystallographic characterization suggests a dominant (111) orientation of the diamond crystallites. This technique provides an economically viable approach for large-size diamond (111) synthesis, because ruthenium has the lowest price among the platinum group metals. 2DHG MOSFETs based on diamond (111) yield better RF performance than (001) because of the high hole density. Moreover, diamond (111) is a highly desirable heat sink for GaN HEMTs. Chapter IV describes the initial growth of diamond (111) on ruthenium. Further experiments will focus on increasing the nucleation density and lateral growth to form a continuous film with a (111) orientation. (Applied Physics Letters submitted)

By proposing an effective approach for functional Si compatible architecture for diamond device, a robust 2DHG diamond FETs and the potential for large-scale diamond

substrates. These works are meaningful for realizing the wide use of diamond as a wide-band-gap semiconductor.

Appendix A MOSFET fabrication

process detail

Substrate preparation

Strong acid boiling	H ₂ SO ₄ (18 mL) + HNO ₃ (6 mL) boiling at 240 °C for 30 min
Substrate cleaning:	* 10 min soak in deionized water ultrasonic bath 10 min soak in ethanol in ultrasonic bath 10 min soak in acetone in ultrasonic bath 10 min soak in ethanol in ultrasonic bath 10 min soak in deionized water ultrasonic bath Blow dry with pure N ₂
Undoped homoepitaxy layer deposition	2 μm via CVD3
Strong acid boiling	H ₂ SO ₄ (18 mL) + HNO ₃ (6 mL) boiling at 240 °C for 30 min
Substrate cleaning:	Same as *
UV ozone treatment	O ₂ introducing: 5 min UV exposure time: 3h N ₂ introducing: 5 min
SiO ₂ deposition	260 nm by TEOS CVD at 300°C for 8 min
Double-layer resist spin	90°C baking for 60 s OAP: 3000 RMP 30 s TSMR V90 27cp: 500 RMP 30 s 180°C baking for 5min PMGI(SIF5): 4500 RMP 30 s 90°C baking for 90s
UV Lithography	Exposure time: 2 s Post baking: 115°C for 90 s Exposure to air: 20 min
Development	NMD-3 developer (2.38%) 60 s First rins:5 s Second rinse: 5 s

	Pure water rinse: 10 min 100°C baking for 60 s
SiO ₂ mask patterning	C3F8 atmosphere for 2 min via ICP-RIE
Double-layer resist remove	3 h or overnight soak in THF at RT (ultrasonic bath if need, once less than 2 s) Acetone spray N ₂ blow dry
Selective growth	at 800 °C for 4 h via CVD5
SiO ₂ remove	HF soak for 3 min at RT

S/D and ohmic contact formation

Substrate cleaning:	Same as *
Double-layer Resist spin	90°C baking for 60 s OAP: 3000 RMP 30 s TSMR V90 27cp: 500 RMP 30 s 180°C baking for 5min PMGI(SIF5): 4500 RMP 30 s 90°C baking for 90s
UV Lithography	Exposure time: 2 s Post baking: 115°C for 90 s Exposure to air: 20 min
Development	NMD-3 developer (2.38%) 60 s First rins:5 s Second rinse: 5 s Pure water rinse: 10 min Baking: 100°C for 60 s
Metallization for S/D	Ti/Pt/Au (20nm/30nm/100nm) via e-beam evaporation
Annealing (TiC formation)	Hydrogen atmosphere at 500 °C for 30 min via CVD 3
Hydrogen-termination	Hydrogen plasma treatment at 600 °C for 30 min via CVD2
Lift-off	3h or overnight soak in THF at RT (ultrasonic bath if need, once less than 2 s) Acetone spray N ₂ blow dry

isolation

Substrate cleaning:	Same as *
Single-layer Resist spin	90°C baking for 60 s OAP: 3000 RMP 30 s TSMR V90 27cp: 500 RMP 30 s 90°C baking for 90s
UV Lithography	Exposure time: 2 s Post baking: 115°C for 90 s Exposure to air: 20 min

Development	NMD-3 developer (2.38%) 60 s First rins:5 s Second rinse: 5 s deionized water rinse: 10 min 100°C baking for 60 s
Single-layer resist remove	1h soak in acetone at RT N ₂ blow dry
SiO ₂ except channel remove	C ₃ F ₈ atmosphere for 2 min via ICP-RIE
Isolation	O ₂ ashing for 2 min
Single-layer resist remove	1h or overnight soak in acetone at RT N ₂ blow dry

Gate insulator formation

Substrate cleaning:	Same as *
Gate isolator deposition	Al ₂ O ₃ 100 nm at 450 °C for 3 h via ALD
Single-layer Resist spin	90°C baking for 60 s OAP: 3000 RMP 30 s TSMR V90 27cp: 500 RMP 30 s 90°C baking for 90s
UV Lithography	Exposure time: 2 s Post baking: 115°C for 90 s Exposure to air: 20 min
Development	NMD-3 developer (2.38%) 60 s First rins:5 s Second rinse: 5 s deionized water rinse: 10 min 100°C baking for 60 s
Al ₂ O ₃ etching for S/D exposure	NMD-3 developer (2.38%) soak for 80 s first rins:5 s Second rinse: 5 s Pure water rinse: 10 min 100°C baking for 60 s
Single-layer resist remove	1h soak in acetone at RT N ₂ blow dry

Gate formation

Substrate cleaning:	Same as *
Double-layer Resist spin	90°C baking for 60 s OAP: 3000 RMP 30 s TSMR V90 27cp: 500 RMP 30 s

	180°C baking for 5min PMGI(SIF5): 4500 RMP 30 s 90°C baking for 90s
UV Lithography	Exposure time: 2 s Post baking: 115°C for 90 s Exposure to air: 20 min
Development	NMD-3 developer (2.38%) 60 s First rins:5 s Second rinse: 5 s Pure water rinse: 10 min Baking: 100°C for 60 s
Metallization for S/D	Al 100 nm by resistance evaporation
Lift-off	3h or overnight soak in THF at RT (ultrasonic bath if need, once less than 2 s) Acetone spray
Substrate cleaning:	Same as *

**List of research achievements for application of doctorate (Dr.
of Engineering), Waseda University**

(Full Name) Wenxi FEI (seal or signature)

By Type	(theme, journal name, date & year of publication, name of authors inc. yourself)
○Paper	<u>W. Fei</u> , M. Inaba, H. Hoshino, I. Tsuyusaki, S. Kawai, M. Iwataki, H. Kawarada, "Point-arc remote plasma chemical vapor deposition for high-quality single crystal diamond selective growth", Physica Status Solidi A, 216, 1900227/1-6, 2019.
○Paper	<u>W. Fei</u> , T. Bi, M. Iwataki, S. Imanishi, and H. Kawarada, "Oxidized Si terminated diamond and its MOSFET operation with SiO ₂ gate insulator" Applied Physics Letters, 116, 212103/1-4, 2020.
Paper	E. Suaebah, M. Hasegawa, J. J. Buendia, <u>W. Fei</u> , M. Chandran, A. Hoffman, H. Kawarada, "Functionalization of a Diamond Surface through N ₂ and H ₂ Irradiation for Estrogen (17β-estradiol) Aptamer Sensing", Sensors and Materials, 31, 1119-1134, 2019.
Oral presentation	Y. Hirano, M. Inaba, K. Suzuki, <u>W. Fei</u> , W. Norimatsu, M. Kusunoki, H. Kawarada, "Metal-Catalyst Free Carbon Nanotube Growth from Template Carbon Nanotube Forest Formed by SiC Surface Decomposition", 2015 MRS Fall Meeting & Exhibit, Boston, USA, Nov. 29-Dec. 4, 2015. (oral)
Oral presentation	<u>W. Fei</u> , M. Inaba, Y. Hirano, H. Masuda, H. Kawarada, "Growth of diamond nanorods using antenna-edge-type microwave plasma-assisted chemical vapor deposition", 10th International Conference on New Diamond and Nano Carbons (NDNC2016), The Westin Xi'an, China, 22-26 May 2016. 2016. (oral)
Poster presentation	<u>W. Fei</u> , M. Inaba, Y. Hirano, H. Masuda, H. Kawarada, "Diamond Nanocylinder Forest Formed by Porous Alumina Template", 2016 MRS Fall Meeting & Exhibit, Boston, USA, Nov. 27-Dec. 4, 2016. (poster)
Poster presentation	<u>W. Fei</u> , M. Inaba, H. Hoshino, I. Tsuyuzaki, S. Kawai, M. Iwataki, H. Kawarada, "Point-arc remote plasma CVD for single crystal diamond site-selective growth", Hasselt Diamond Workshop 2019 - SBDD XXIV, Hasselt, Belgium, Mar. 13-15, 2019. (Poster, March 13)

(As of July 2020)